

**MODELING BIOMASS TRANSPORT IN  
A COMPRESSION SCREW FEEDER**

by

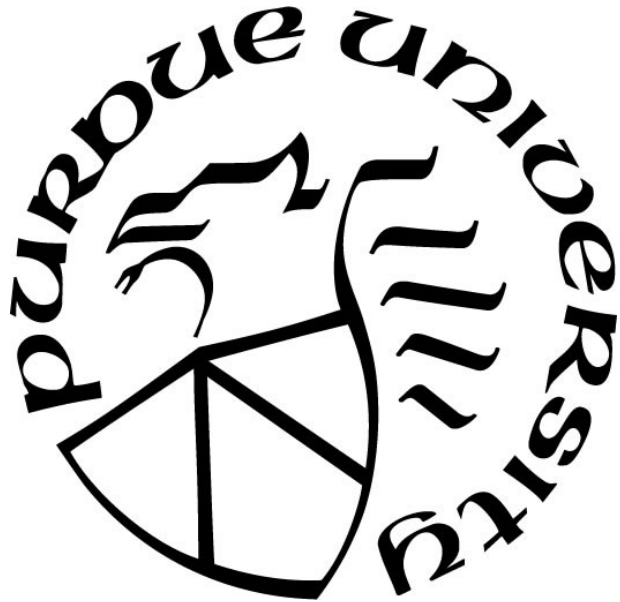
**Nathaniel Hall Gasteyer**

**A Thesis**

*Submitted to the Faculty of Purdue University*

*In Partial Fulfillment of the Requirements for the degree of*

**Master of Science in Mechanical Engineering**



School of Mechanical Engineering

West Lafayette, Indiana

August 2020

**THE PURDUE UNIVERSITY GRADUATE SCHOOL  
STATEMENT OF COMMITTEE APPROVAL**

**Dr. Carl Wassgren, Co-Chair**

School of Mechanical Engineering

**Dr. Marcial Gonzalez, Co-Chair**

School of Mechanical Engineering

**Dr. Kingsley Ambrose**

School of Agricultural and Biological Engineering

**Approved by:**

Dr. Nicole Key

*To my friends and family.*

## ACKNOWLEDGMENTS

I could not have accomplished everything that I have without the incredible support of those around me. Firstly, I would like to thank Prof. Marcial Gonzalez for introducing me to graduate school and helping me find a research group that was such a good fit for me. Thanks to him, this experience has helped me grow personally, professionally, and academically. I would also like to thank Prof. Carl Wassgren for providing guidance and making my graduate school experience worth every hour of hard work. Special thanks to Prof. Kingsly Ambrose for serving on my examination committee and helping me when and where he could. Additionally, I would like to thank everyone in CP3 for helping me to become a better researcher and student.

I am also lucky enough to have made an incredible group of friends during my time at Purdue. Among many others, Andrew, Jacob, and Thor were always there for me when I needed someone, and I'll always remember the six years of good times that we shared.

Finally, I'm thankful for my parents who always wanted what is best for me. They did everything they could to help me succeed, and because of that, my dreams have come true.

# TABLE OF CONTENTS

LIST OF TABLES .....	7
LIST OF FIGURES .....	8
NOMENCLATURE .....	15
ABSTRACT.....	17
1. INTRODUCTION .....	1
2. BACKGROUND .....	4
2.1 Screw Feeder Models.....	4
2.1.1 Pressure Evolution in a Screw Feeder .....	4
2.1.2 Torque Models for a Screw Feeder .....	9
2.2 Compressed Bed Models .....	12
2.3 DEM Modeling of Screw Feeders .....	18
2.4 Literature Summary .....	21
3. OBJECTIVES.....	23
4. DEM MODELS .....	24
4.1 Force Models .....	24
4.2 Screw Simulations .....	26
4.2.1 Geometry, Setup, and Inputs .....	26
4.2.2 Results.....	32
4.3 Plug Simulations.....	46
4.3.1 Geometry, Setup, and Inputs .....	47
4.3.2 Results.....	53
4.4 Summary of DEM Conclusions.....	58
5. ANALYTICAL MODELS .....	60
5.1 Methodology.....	61
5.2 Pressure Models .....	63
5.2.1 Plug Section Model.....	63
5.2.2 Screw Section Model.....	71
5.3 Torque Models .....	73
5.3.1 Plug Section Model.....	73

5.3.2	Screw Section Model.....	75
5.4	Analytical Models Summary .....	79
6.	ANALYTICAL MODEL INPUT PARAMETERS .....	81
6.1	Screw Geometry.....	81
6.2	Friction Coefficients and Friction Angles.....	83
7.	COMPARISON OF ANALYTICAL MODELS TO DEM SIMULATIONS .....	87
7.1	Plug Section And Screw Section Pressure Models.....	87
7.2	Plug Section Torque Model .....	94
7.3	Screw Section Torque Model.....	95
7.4	Full Screw Comparison.....	97
8.	SUMMARY AND CONCLUSIONS .....	100
9.	FUTURE WORK.....	103
	REFERENCES .....	106

## LIST OF TABLES

Table 4.1: Autodesk Inventor STL mesh properties. These properties were tuned to create a balance of mesh refinement and computational efficiency.....	29
Table 4.2: Compression feed screw simulation input properties.....	32
Table 4.3: Straight plug simulation input properties. The properties shown were arbitrarily selected and resemble those used in the screw feeder simulations.....	50
Table 4.4: Converging plug simulation input properties. Like the straight plug simulation input properties, these are arbitrary chosen to be similar to those used in the screw simulations.....	52
Table 6.1: Non-geometric model input properties. All other model parameters are known and well defined.....	81
Table 7.1: Straight plug model input parameters. These parameters were chosen using Figure 6.5 to provide a valid comparison between DEM and the analytical models.....	88
Table 7.2: Converging plug model input parameters. These parameters were chosen using Figure 6.5 to provide a valid comparison between DEM and the analytical models.....	89
Table 7.3: Analytical model parameters used in the plug model in order to compare results with the screw simulation. These parameters were chosen using Figure 6.5 to provide a valid comparison between DEM and the analytical models.....	92

## LIST OF FIGURES

Figure 1.1: Schematic of a representative compression screw feeder showing the important boundary conditions for the feeding process. ....	2
Figure 1.2: Process operations block diagram for the front-end of a representative biorefinery. Solid material enters on the left end, and a liquified slurry exits on the right. The compression screw feeder is needed to convey and compress material into the high-temperature high-pressure horizontal screw reactor (BETO 2019 Project Peer Review). ....	2
Figure 2.1: Unwrapping process of a screw feeder with a fixed element of the case. This technique was used by Darnell et al. as the foundation of their stress analysis and helps show the direction of the relative velocity between the material within the screw channel and the case. ....	5
Figure 2.2: Screw geometry terminology for all faces that interact with material within the screw feeder.....	6
Figure 2.3: Isometric view of the differential element of material considered by Darnell et al. (1956) showing the helical angle.....	6
Figure 2.4: Top-down view of the free body diagram used by Darnell et al. (1956). The polyhedron of material touches 6 faces, and the forces exerted by each face on the element of material is concentrated at the center of the face.....	7
Figure 2.5: Material in a screw pitch considered by Yu and Arnold (1997). ....	11
Figure 2.6: An Element of material within the screw pitch considered by Yu and Arnold (1997). ....	11
Figure 2.7 The differential element considered by Janssen. This shows the side-view of a disk of material subject to shear forces at the outer edge, material stress from above and below, and a gravitational force. ....	13
Figure 2.8 Differential element used by McNab and Bridgewater. Their differential element is valid immediately after a spouted bed forms and fluid is exerting a shear force on the inner face of the annulus of material.....	16
Figure 2.9 Axial stress solutions for a confined vertical column of material. This figure shows all solution forms resulting from considering a column of material subject to boundary conditions and body forces.....	17
Figure 2.10: Simple compaction cell showing confined particles subject to a punch-and-die type loading.....	19
Figure 2.11: Torpedo outlet boundary condition found in experiments performed by Moysey et al., (2004).....	20
Figure 2.12: Force field boundary condition that allows for a pressure boundary condition that is decoupled from material properties. The applied pressure depends on the magnitude of the force field, and the cross sectional area of the channel in the flow direction. ....	21

Figure 4.1: Contact model used in all DEM simulations. A linear hysteretic model is coupled with a simple Coulomb friction model. Particles subject to this contact model cannot store elastic energy in their tangential contacts. .... 24

Figure 4.2: Screw simulation overall geometry. The three major sections of a compression screw feeder are the hopper section, the compression throat section, and the plug section. .... 26

Figure 4.3: Detailed screw geometry. These dimensions are loosely based on a screw feeder assembly in a pilot scale facility at Idaho National Laboratory..... 27

Figure 4.4: Divided case geometry. These dimensions are also loosely based on a screw feeder assembly in a pilot scale facility at Idaho National Laboratory, but have been simplified to remove sharp edges, corners, and pockets. .... 27

Figure 4.5: Sliced screw geometry. When each slice is rotated together, this geometry behaves the same as a single screw body but allows for DEM results to be extracted from each slice individually. .... 28

Figure 4.6: Screw geometry with separate faces. When each screw face is rotated together, this geometry behaves the same as a single screw body but allows for DEM results to be extracted from each slice individually..... 29

Figure 4.7: The meshed surface of the screw. The mesh properties were chosen to avoid long, thin elements which adversely affect the way boundary forces are calculated within DEM. .... 29

Figure 4.8: Outlet axial stress boundary condition. Step one shows a body (a thick black line) parallel to the exit that is allowed to move but subject to a boundary force, P. Steps 2, 3, and 4 show the boundary movement as the particles advance toward the exit. .... 30

Figure 4.9: Oscillations of outlet axial stress are caused by the movement of the body at the exit of the screw feeder simulations that is used to apply a pressure. The average axial stress is much lower than the input axial stress..... 30

Figure 4.10: Corn stover shape and size with a ruler for scale. The particles are mostly plate-like, with millimeter scale dimensions in two directions and tenths of millimeter dimensions in the third direction. Other particle shapes include narrow, rod-like particles with only a single dimension on the scale of millimeters, and brick-like particles with all three dimensions on the millimeter scale. .... 31

Figure 4.11: Compression feed screw simulation showing the particle fill at the initial timestep. .... 32

Figure 4.12: Particle bin in the screw channel. The bin is positioned so the center is between the outer case, the inner case, and each screw flight face..... 33

Figure 4.13: Particle bin path in the screw section. Along the helical path of the bin, the axial position is also recorded such that the axial stress progression can be measured. .... 33

Figure 4.14: Particle bin stresses within the screw channel. To recover these stresses along the helical path, the bin must be rotated such that the face measuring the radial stress points directly outward from the screw axis. .... 34

Figure 4.15: Particle bins in the plug section. The particle bin wraps around the entire annulus and provides average values of the stresses over the cross section. ....	34
Figure 4.16: Particle bin stresses. Unlike the screw section, the particle bins in the plug section average the stresses over the entire annulus. ....	35
Figure 4.17: Comparison of solid stresses over screw length. The peak pressure is higher than the average applied outlet stress and is reached at the start of the plug section (end of the screw flights). The growth up to the start of the plug section is not exponential. ....	36
Figure 4.18: Bin positions for measuring pressure near the screw flights. The bin was moved as close as possible to the screw flight, but the closest edge remained one particle radius away.....	36
Figure 4.19: Pressure change from leading to trailing flight in the screw section, showing that the pressure near the screw flights is close to the average pressure measured in the center. In the highly compact region at the end of the screw flights, the pressures remain very close. ....	37
Figure 4.20: Screw pressure vs. position, backpressure, pitch, and particle-particle friction coefficient. These results represent a preliminary parametric study and only include the parameters that were hypothesized to be the most important.....	38
Figure 4.21: Screw pressure vs. Position, $\mu_{pp} = 0.5$ . The peak pressure is seen to scale with the backpressure within each screw pitch. Near the end of the screw flights there is some non-uniform growth, but within each screw pitch, the behavior is consistent.....	39
Figure 4.22: Peak pressure and torque, sensitivity to pitch, $\mu_{pp} = 0.25$ . Peak pressure and total screw torque show similar, linear sensitivities to screw pitch and backpressure suggesting a strong correlation. More backpressures and screw pitches are needed to investigate the relationship further.....	40
Figure 4.23: Peak pressure and torque, sensitivity to backpressure, $\mu_{pp} = 0.25$ . In contrast to Figure 4.22, this plot shows screw pitch on the x-axis instead of backpressure.....	40
Figure 4.24: $dT/dz$ versus axial position, $\mu_{pp} = 0.5$ . $dT/dz$ at each location scales with backpressure, but a form for the screw section is unclear. The development of $dT/dz$ in the screw section is not monotonic. ....	42
Figure 4.25: $dT/dz$ and pressure versus axial position where pitch = 1.5", backpressure = 500 kPa, $\mu_{pp} = 0.25$ . The figure shows that $dT/dz$ is not proportional to the measured pressure. ....	43
Figure 4.26: $dT/dz$ and screw radii versus axial position where pitch = 1.5", backpressure = 500 kPa, $\mu_{pp} = 0.25$ . $dT/dz$ is affected by the case and core radius of the screw in addition to the solid pressure, but the form is unclear. ....	43
Figure 4.27: Rotational power dissipation by screw face, pitch = 2", $\mu_{pp} = 0.5$ . In all cases, the leading flight dissipates the most energy, followed by the screw core almost an order of magnitude lower. The trailing flight generates energy in the system, but this behavior is not well understood. ....	45
Figure 4.28: Stress direction compared with boundary velocity. This diagram shows that at the leading flight, a component of the normal stress is directed in the opposite direction of the	

boundary velocity, dissipating energy. However, the trailing flight has a component of the normal stress in the direction of the boundary velocity. ....	46
Figure 4.29: Straight plug section simulation showing the annular particle bed being compressed. ....	46
Figure 4.30: Tapering plug section simulation showing the arrangement of particles as they are being compressed. ....	47
Figure 4.31: Plug simulation procedure for mobilizing friction. The applied stress is increased until the threshold stress is reached on the other end of the annulus and the bed starts sliding. After the bed begins to slide, and the direction of friction is known the pressure profile is measured .....	48
Figure 4.32: Straight plug section dimensions. The initial plug length is 5”, but after compaction the axial length changes. ....	48
Figure 4.33: Straight plug section case mesh. This mesh was chosen due to the regularity of the mesh size and shape. Because particle bins are used to measure stresses instead of boundary forces, it is not necessary to use a fine mesh. ....	49
Figure 4.34: Straight plug section shaft mesh. Like Figure 4.33, this figure shows the regular mesh size and shape of the straight plug simulations. ....	49
Figure 4.35: Tapering plug section dimensions. The tapering plug section simulations include one end with a tapering section where the stress is incrementally increased. On the other end, after a small straight section, a threshold pressure is applied. ....	51
Figure 4.36: Tapering plug section case mesh. This mesh was generated with the same mesh properties as the screw feeder and the straight plug section. ....	51
Figure 4.37: Tapering plug section shaft mesh. ....	52
Figure 4.38: Annular Eulerian particle bin. The bin shown is positioned between the tapering outer case and the constant inner case. ....	53
Figure 4.39: Direction of stresses and coordinate system. A high stress is applied at the inlet, and a low stress is applied at the outlet. ....	54
Figure 4.40: Average stresses over the length of the straight plug simulations. Except for some boundary effects at the high-pressure side, the growth from low to high pressure is consistent. The axial stress is much larger than the radial and theta stresses and the material is not in a hydrostatic stress state like that found in the screw feeder simulations. ....	54
Figure 4.41: The ratio of average principal stresses over the length of the straight plug. These values remain largely constant over a wide range of stresses. ....	54
Figure 4.42: Screw feeder plug section, high-pressure entrance. The transition region from the screw flights into the plug section is complicated and subject to significant normal and shear stresses from the leading screw flight. ....	55
Figure 4.43: Standalone plug section, high-pressure boundary condition. Unlike the entrance to the plug region in the screw feeder simulations, the plug simulations experience a uniform axial loading. ....	56

Figure 4.44: Direction of stresses and coordinate system for the converging plug simulations. The straight section begins at a dimensionless axial position of  $\sim 0.8$ . ..... 57

Figure 4.45: Average stresses over the length of the converging plug. Like the straight plug, the converging plug shows that the axial stress is much larger than the radial and theta stresses. However, due to the convergence causing a radial compression, the ratio of axial to radial stress is larger than in the straight plug simulations. Some oscillations and perturbations near the boundaries can be seen, but they are a result of the stress measurement and experimental setup. .... 57

Figure 4.46: The ratio of the average principal stresses over the length of the converging plug. Although there are oscillations in the curves, the ratios of the principal stresses remain relatively constant. .... 58

Figure 5.1: Hypothesized versus observed pressure profile. The DEM results show that the peak stress in the system is not the outlet stress, as was previously hypothesized. Rather, the screw section and plug section exhibit significantly different behavior and must be treated individually. .... 60

Figure 5.2: Screw section model versus plug section model. The two different regions of DEM behavior are highlighted and the validity of the models is defined. .... 61

Figure 5.3: Plug section of the compression screw feeder. This figure shows the general shape of the feeder after the screw flights end, and define the direction of the coordinate system. .... 61

Figure 5.4: Torque model procedure. The most important part of the procedure is starting at the material outlet. By developing a model that begins with the backpressure, that boundary condition can be accounted for in the screw section model. Using the plug pressure as a boundary condition, a screw section pressure model, and then a model to convert from pressure to torque are presented. .... 62

Figure 5.5: Constant geometry plug section differential element. The inner face of the annulus is touching a stationary inner shaft and sliding along it axially. .... 63

Figure 5.6: Mohr's circle for active failure at an orthogonal wall. This Mohr's circle defines the relationship between shear and normal stresses using trigonometric relationships..... 64

Figure 5.7: Simplified Mohr's circle diagram for the active state of stress, assuming failure along an orthogonal wall..... 65

Figure 5.8: Converging plug section differential element. The radius is a function of the axial position causing the resulting surface areas to also be a function of axial position. .... 67

Figure 5.9: Surface area of the inclined edge of a conic frustum. .... 68

Figure 5.10: Mohr's circle for active failure at an inclined wall. Point C deviates from point R by two times the angle of inclination of the wall to the axis. .... 69

Figure 5.11: Screw feeder pressure profile. The pressure of the material within the hopper (up to the hopper length,  $Lh$ ) is zero, and the pressure grows to the peak pressure over the length of the screw flights,  $Lf$  ..... 72

Figure 5.12: Plug section torque model. The shear and normal stresses are shown for a differential axial slice of the screw shaft. ....	73
Figure 5.13: Differential element of material interacting with the screw feeder surface. ....	76
Figure 5.14: Screw torque model differential element. Only the stresses that the material exerts on the screw faces are considered. ....	76
Figure 5.15: Radii at which the forces act about the screw axis. Looking down the length of the screw, assuming all stresses act at the center of their respective faces, the radii at which they act are known. ....	77
Figure 5.16: Screw differential element shape. The areas of each face are defined in terms of known geometric parameters, $h$ , $w$ , and $dL$ . It is important to note that $dL$ is in the helical direction. ...	78
Figure 5.17: Relationship between the helical and axial direction. By placing two differential elements next to one another it is possible to construct the relationship between the helical and axial direction. ....	79
Figure 6.1: Helical angle at the screw shaft and at the screw case. Because the helical angle changes as a function of the radius on the screw face, a single average value must be used. ....	82
Figure 6.2: Helical angle calculation. Using the average radius, the flight thickness, and the screw pitch, the average helical angle can be calculated. ....	83
Figure 6.3: Internal yield locus and wall yield locus for a granular material. The Mohr's circle is always constrained by the internal yield locus, but the wall yield locus will intersect the Mohr's circle at two points. One of these points represents active failure, and the other represents passive failure. ....	84
Figure 6.4: DEM friction coefficients are defined by the interacting bodies. The friction coefficients do not change under static or dynamic conditions and are represented by one value. ....	85
Figure 6.5: Relationship between DEM friction coefficient and bulk friction angle (Ketterhagen et al., 2009). The current work uses non-rotational particles, and therefore the upper curve is used to map particle-particle friction coefficient (DEM input) to internal friction angle (analytical model input). ....	86
Figure 7.1: Straight plug section simulation. ....	88
Figure 7.2: Comparison of Equation 42 to DEM simulations. The model for pressure lies between the axial stress and the pressure measured in DEM, and predicts a peak stress on the correct order of magnitude. ....	88
Figure 7.3: Converging plug section simulation. ....	89
Figure 7.4: Comparison of Equation 59 to plug DEM simulations. The straight section of the converging plug simulations (from a dimensionless axial position of $\sim 0.8-1.0$ ) are well captured by the analytical model, but the converging section (from a dimensionless axial position of $0-\sim 0.8$ ) is not captured by the analytical model. ....	90

Figure 7.5: Factors contributing to the pressure change in a converging plug. Each of these factors (area, inclined normal force, shear force at case, shear force at core) are accounted for with a distinct term in the converging plug model. .... 91

Figure 7.6: Relative magnitudes of terms in the plug section of the screw feeder. The contributions of each factor are summed to determine the sign and magnitude of the exponential growth predicted in the plug section, and the change in area contributes a large negative value..... 91

Figure 7.7: Screw simulation showing only the particles in the plug section..... 92

Figure 7.8: Comparison of Equation 59 to screw DEM simulation. The straight section of the plug (from a dimensionless axial position of  $\sim 0.15-1$ ) is captured well if the internal friction angle is varied, and similar results are obtained if the Walker distribution factor is varied) However, the converging section (from a dimensionless axial position of  $0\sim 0.15$ ) is not captured. .... 93

Figure 7.9: Model predictions of DEM pressure values,  $\mu_{pp} = 0.5$  if the peak pressure is known. The quadratic form fits the data well and matches the curvature at the high pressure region at the end of the screw flights, although in some cases, a linear fit provided a better match..... 94

Figure 7.10: Plug section torque model compared against DEM torque values. The plug torque is overestimated by the model even if the DEM pressure is used. .... 95

Figure 7.11: Screw section torque model compared against DEM torque values. The screw torque is overestimated by the model even if the DEM pressure is used. .... 96

Figure 7.12: Modified torque model with DEM pressure curve. By removing the contribution of the trailing flight from the final form of the torque model, the prediction is improved significantly. This modification is motivated by Figure 4.27. .... 97

Figure 7.13: Full screw torque model predictions versus DEM torque. Both the plug section model and screw section model overpredicted the torque, and when combined, they overpredict the total torque. The predictions were worse for small internal friction coefficients and high backpressures. .... 98

Figure 7.14: Full screw torque model predictions with modified torque model and DEM pressure (no trailing flight). By modifying the torque model using conclusions from the DEM simulations, it is possible to significantly improve the match. .... 99

Figure 7.15:  $dTdz$  shape for pressure-based torque model and typical DEM simulations. The curvature is not captured in the screw section or the plug section, and further investigation is needed. .... 99

## NOMENCLATURE

$\mathcal{D}$	Walker distribution factor
$F_{NU}$	Normal force on upstream face of material
$F_{ND}$	Normal force on downstream face of material
$F_{NL}$	Normal force on leading screw flight edge
$F_{TL}$	Tangent force on leading screw flight edge
$F_{NT}$	Normal force on trailing screw flight edge
$F_{TT}$	Tangent force on trailing screw flight edge
$F_{NC}$	Normal force on screw case
$F_{TC}$	Tangent force on screw case
$F_{NS}$	Normal force on screw shaft
$F_{TS}$	Tangent force on screw shaft
$h$	Screw channel height
$K_f$	Janssen Coefficient
$L_f$	Length of screw with screw flights
$L_h$	Length of hopper section
$L_{plug}$	Length of the plug section
$L_{screw}$	Length of the screw with screw flights minus length of hopper
$P$	Pressure
$R$	Radius
$\bar{R}$	Average radius of screw flights
$R_c$	Radius at the screw case
$R_s$	Radius at the screw shaft
$s_n$	Particle overlap
$T_z$	Screw Torque
$w$	Screw channel width
$z$	Axial position
$dL$	Differential length in helical direction
$dT_z$	Differential screw torque

$dz$	Differential length in axial direction
$\alpha_c$	Conveying angle
$\alpha$	Plug section taper angle
$\mu_w$	Wall friction coefficient
$\mu_{pp}$	Particle-particle friction coefficient (DEM)
$\mu_{pb}$	Particle-boundary friction coefficient (DEM)
$\phi_h$	Helical angle
$\bar{\phi}_h$	Average helical angle
$\phi_i$	Internal friction angle
$\phi_w$	Wall friction angle
$\sigma$	Normal stress
$\sigma_0$	Initial normal stress
$\tau$	Shear stress (usually associated with friction)
$\tau_0$	Initial shear stress
$\omega$	Screw speed

## ABSTRACT

Biorefineries which seek to convert biomass into ethanol face many different challenges, and among them, mechanical failure of equipment is common. Unfortunately, the resulting downtime can significantly reduce the profitability and the viability of bioethanol plants. One important piece of mechanical equipment in this setting is the compression screw feeder, which is used both to convey and compress biomass into pressurized chemical reactors. However, due to the variability of feedstock properties, this feeding operation is challenging. An analytical model for predicting the operational steady-state torque of a compression screw feeder can assist the identification of optimal processing conditions, as well as predict and prevent equipment failure.

Since these models have not yet been proposed, this thesis restricts attention to milled corn stover and investigates the application of the discrete element method (DEM) and analytical techniques to develop predictive models for the stresses and torques developed inside a compression screw feeder. Specifically, DEM simulations are used to identify and study the stresses within the different sections of a representative compression screw feeder for three backpressures, three screw pitches, and three internal friction angles. Using these numerical results, a suite of analytical models is then developed to predict the operational torque required to drive the screw feeder. In this thesis, the DEM results are also used in lieu of experimental data to provide a point of comparison for the models.

The analytical models predict stresses on the correct order of magnitude and are not prohibitively sensitive to input properties, but the operational steady-state torque is overpredicted by the model in all cases. The mispredictions of the model are likely due to the assumption of constant material properties along the densification process, and the assumption of hydrostatic conditions throughout the compression screw feeder (especially near the boundaries). Despite these limiting assumptions, the proposed procedure for calculating the torque provides a first-order estimate of the required screw torque, demonstrates the sensitivity of the screw feeder to different inputs, and outlines the necessary steps to improve the model. The DEM simulations proved an invaluable tool in analyzing the behavior of bulk material within a compression screw feeder, but more experiments and simulations (possibly using the finite element method) are needed to further understand the biomass feeding operation.

# 1. INTRODUCTION

Screw feeders are one of the most common and important devices found in industrial processes involving particles and powders, but they are also a source of significant difficulties. In fact, solid material handling is one of the major issues that plague bulk solids industries by causing unpredictable downtime and equipment malfunction (Dai & Grace, 2008a). A study performed in 1981 found that in 40 solids processing plants across the U.S. and Canada, 80% of these plants had solids handling issues (Morrow et al., 1981), and further study led to the conclusion that mechanical problems dominate plant failures (Morrow, 1985). This problem has persisted, and the United States Department of Energy (DOE) and their Bioenergy Technologies Office (BETO) has recently cited complexity and variability of feedstocks and operational difficulty encountered when handling of solids as two of the most important problems affecting the economical operation and scale-up of bioethanol production (DOE, 2016).

Although screw feeders are common, their mechanics are often not well understood. In his 1964 paper, Metcalf offers the following description of how screw feeders operate:

The screw feeder is mentioned briefly in various engineering handbooks and is the subject of patents. From such sources it appears that the following description of its action is commonly accepted. The material fills the available space between screw and tube wall forming one or more helical ribbons, depending on the number of wings. Rotation of the screw tends to rotate the ribbon. Friction on the tube wall opposes this. The ribbon can avoid rotation by moving axially, though this is also opposed by friction on the tube wall and on the screw. The ribbon therefore moves both in rotation and axially so that effort against friction is a minimum. Hence a smooth tube and a rough screw of long pitch favor rotation of the ribbon. A rough or ribbed tube with a smooth screw of short pitch favors axial movement and so gives the better rate of delivery. (p. 131)

Biorefineries operate using many different types of solid materials and must be able to reliably move them from one location to another, and in some cases, compress the material. Screw feeders can be used to accomplish both tasks, but the focus of this work is centered on compression. In compression screw feeders (Figure 1.1), loose material enters the system from a hopper that is exposed to atmospheric pressure. The screw flights then carry the material down the length of the screw and into a section called the compression throat where the case around the screw reduces in diameter and the material is compressed. Further downstream, the screw flights end and the material is forced into a thin, ring-shaped section at the exit, called the plug section. Finally, at the

exit of the plug section the material enters a high-temperature, high-pressure reactor where it is chemically processed (Figure 1.1). By compressing the material, a dense and impermeable plug is formed in the plug section that resists the backflow of pressurized gas from the reactor, called blowback. If the plug is too dense, the screw will seize and require a costly and time-consuming shutdown to remove, however, if the plug is too loose, it will be too weak to resist blowback. The mechanisms that create and maintain the integrity of the plug are still poorly understood. Although models of screw feeders have been previously developed (Broyer & Tadmor, 1972; Campbell & Dontula, 1995; Dai & Grace, 2008a; Darnell & Mol., 1956; Hyun & Spalding, 1997; Metcalf, 1965; Yu & Arnold, 1997), these models do not typically address the feeding of material into a backpressure, and some of the required material properties are either challenging or cost-prohibitive to directly measure in experiments.

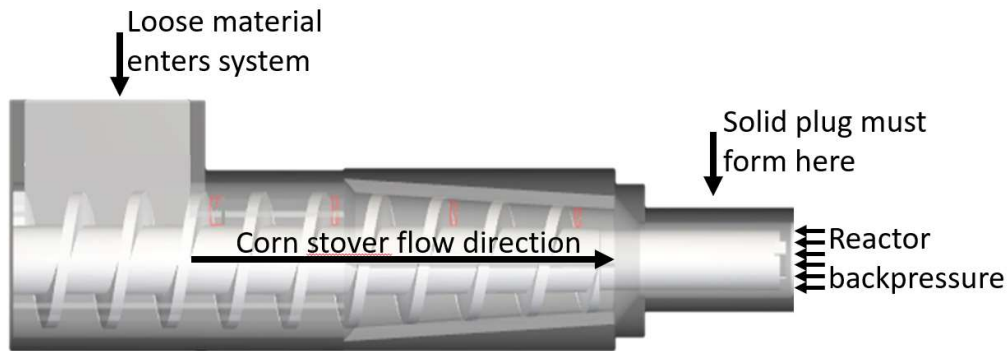


Figure 1.1: Schematic of a representative compression screw feeder showing the important boundary conditions for the feeding process.

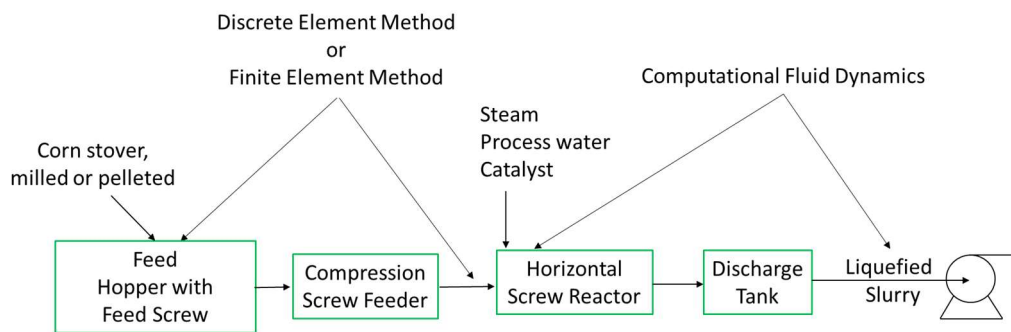


Figure 1.2: Process operations block diagram for the front-end of a representative biorefinery. Solid material enters on the left end, and a liquified slurry exits on the right. The compression screw feeder is needed to convey and compress material into the high-temperature high-pressure horizontal screw reactor (BETO 2019 Project Peer Review).

The focus of this work is twofold. Firstly, DEM simulations are used to understand compression, densification, and plug formation within a compression screw feeder. Secondly, a set of analytical models is presented, informed by the DEM model, that attempts to predict the steady-state torque required to run a screw feeder. Finally, the analytical models are compared to results from the DEM simulations and their accuracy is assessed.

## 2. BACKGROUND

### 2.1 Screw Feeder Models

The models described in this section focus on obtaining predictions for material stresses as the material is transported through a screw, and how these stresses generate a screw torque. These models are developed for steady-state operating conditions.

#### 2.1.1 Pressure Evolution in a Screw Feeder

There is limited prior work focused on developing models for feeding biomass materials (Dai & Grace, 2008a). However, there has been considerable study of pellet feeding during plastic extrusion. In the field of polymer processing, a screw is used to convey solid, pelleted material as it melts and is squeezed out of a tapering screw cavity. During this process, three different screw zones have been identified, namely the solids conveying zone, the melting zone, and the melt conveying zone (Tadmor & Klein, 1970). The analysis of the solid conveying zone is most pertinent to this thesis since the biomass remains as a solid material during feeding.

Although the literature refers to these as “solid plug” models, this thesis refers to such models as “screw flight” models. This terminology is used to avoid confusion with the “plug section” of the biomass compression feed screw. These plastic extrusion models are only valid in the compression screw feeder section where screw flights are interacting with the material.

One of the earliest works in this field was conducted by Darnell et al. (1956) which served as the foundation for the following studies. Darnell et al. developed a one-dimensional analytical model to describe material behavior in the solids conveying zone of a plastic extruder using the following assumptions (Tadmor & Klein, 1970):

1. The material in the screw is a continuum.
2. The material completely fills the screw feeder and interacts with all boundary surfaces.
3. The channel depth is constant.
4. The flight clearance between the screw and the casing is negligible
5. The velocity of the material is constant in time (steady-state), and uniform across a cross section of a screw flight.
6. The material stress is a function of the down channel direction only.

7. All friction coefficients are independent of pressure.
8. Gravitational forces are negligible
9. The material bulk density is constant along the length of the screw.

Additionally, it is important to note that the coordinate system in this analysis is attached to a representative volume of material in the screw channel. Thus, the screw and boundary move relative to the representative element.

Under the assumptions listed above, Darnell et al. considered the helical screw cavity as a straight channel that is wrapped along a helical path. This insight allows the screw channel and case to be unwrapped, transforming the helical screw into a straight channel (Figure 2.1). Additionally, instead of analyzing a system with a fixed screw casing and rotating inner screw, a fixed screw with a rotating case is considered. This process was used by Darnell et al. (1956) to determine the direction of all forces in the free body diagrams by shedding light on the relative motion between the material and the screw. In the figure,  $\omega$  is the screw speed, and  $\bar{\phi}$  is the average helical angle of the screw which is defined later.

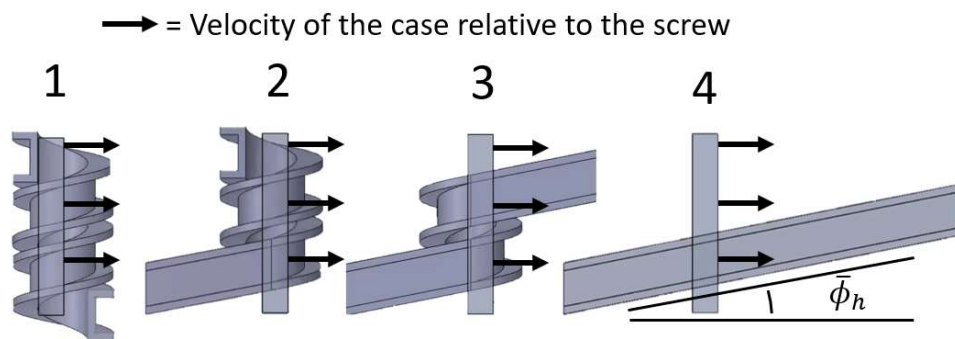


Figure 2.1: Unwrapping process of a screw feeder with a fixed element of the case. This technique was used by Darnell et al. as the foundation of their stress analysis and helps show the direction of the relative velocity between the material within the screw channel and the case.

The first step to predicting the stresses in the material within the screw flights requires a force balance on a differential element of material in the screw flights, noting that assumption 5 eliminates inertial effects from consideration and allows for all calculations to be quasi-static. Although it is unclear in the wrapped screw geometry, the unwrapped screw shows that the movement of material is constrained in every direction except the downstream flow direction

shown in Figure 2.2. Figure 2.3 shows the differential element of material considered by Darnell et al., and Figure 2.4 shows the top-down view of the free body diagram.

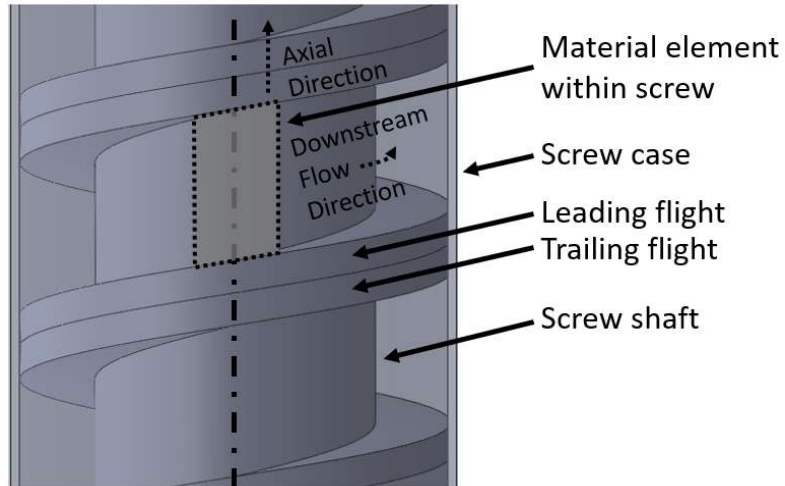


Figure 2.2: Screw geometry terminology for all faces that interact with material within the screw feeder.

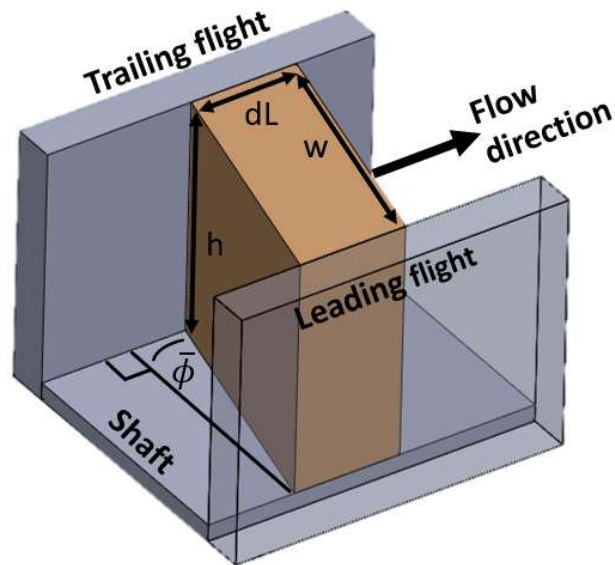


Figure 2.3: Isometric view of the differential element of material considered by Darnell et al. (1956) showing the helical angle.

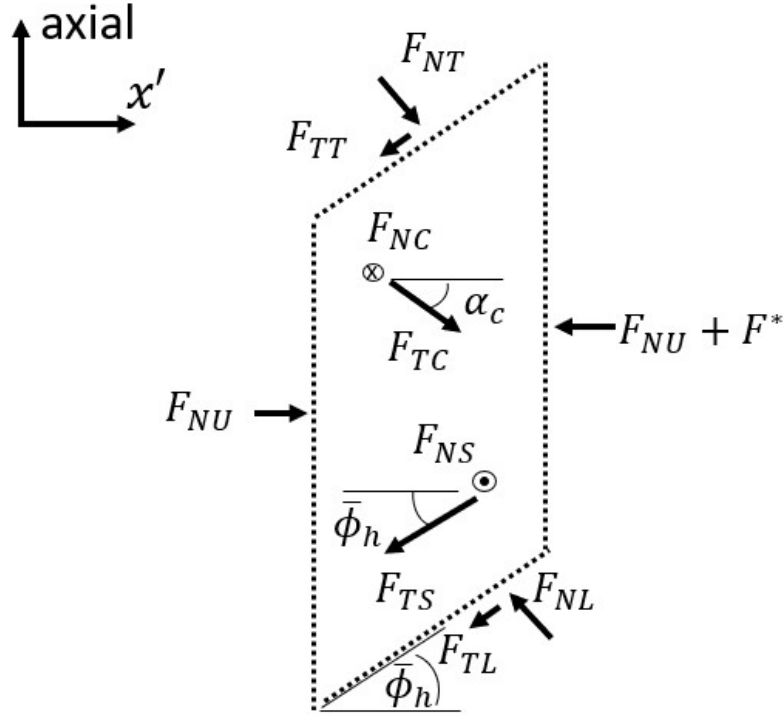


Figure 2.4: Top-down view of the free body diagram used by Darnell et al. (1956). The polyhedron of material touches 6 faces, and the forces exerted by each face on the element of material is concentrated at the center of the face.

The boundary forces of interest are the normal and friction force on the leading screw flight ( $F_{NL}$  and  $F_{TL}$ ), the trailing screw flight ( $F_{NT}$  and  $F_{TT}$ ), the outer screw case ( $F_{NC}$  and  $F_{TC}$ ), the inner screw shaft ( $F_{NS}$  and  $F_{TS}$ ), and the force exerted on the element by the upstream material ( $F_{NU}$ ) and the downstream material ( $F_{ND}$ ). Lastly, all models that follow this approach also include an extra force ( $F^*$ ) applied at the leading flight face in order to add a degree of freedom to the solution. It is assumed that the forces are distributed uniformly over the face that they act on, and with this, the general solution strategy is to reduce the problem to two equilibrium equations and two unknowns ( $F_{ND}$  and  $F^*$ ) by relating the forces to one another. However, within this approach, the common solution strategies differ in three ways: their selection of equilibrium equations, the direction of the extra force ( $F^*$ ), and the relationships used to relate the unknown forces. These differences are discussed in the following paragraphs.

Firstly, different models select different equilibrium equations to solve for the forces. All solution strategies use the  $x'$  force balance equation as shown in the free body diagram of Figure 2.4, but another equation is needed to solve for the unknowns. One class of models (Campbell &

Dontula, 1995) assumes the material behaves like a fluid, and the solution is therefore unable to apply a torque balance. Instead, the direction and magnitude of the unknown force are assumed, and the equilibrium equation is reduced to a single equation and one unknown. The most common class of models, though, uses the axial force balance and an axial torque balance on the material in their solution. In this way, less is assumed about the extra force ( $F^*$ ) at the leading flight face, and the problem is allowed more degrees of freedom.

Secondly, the models each treat the extra force ( $F^*$ ) differently. Darnell et al. and Tadmor et al. (1972) both assume the angle of this force is perpendicular to the leading flight face, but it is of unknown magnitude. Hyun assumes that the additional force is at the leading face and is of unknown magnitude, but changes the analysis by assuming this force is not perpendicular to the leading flight face (Hyun & Spalding, 1997). Lastly, Campbell's model includes the force at the leading flight face but assumes the angle and magnitude. Little rationale is given to these modeling choices, and although the treatment of this force does not significantly alter the form of the resulting equations, it does alter the resulting solution.

Third, the models each relate the forces to one another through different assumptions. In each model, the forces on each face are combined with the area of the face to convert them into stresses. Once the forces are expressed in terms of stresses, each model makes different assumptions to relate the stresses to each other. The stresses in a fluid do not depend on the surface normal direction, and therefore the model developed by Campbell assumes that the stresses on the shaft, flights, and case are all equivalent along the screw channel. Darnell and Tadmor both assume that the material in the screw flights is in an isotropic stress state and, therefore, the stresses on all surfaces are assumed equivalent as well. An improvement was made to this assumption in the Hyun model, in which the out-of-plane stresses are assumed to be anisotropic and are related to the stress in the helical/down-channel direction with a single stress ratio " $K_r$ ". The stress ratio is an important constant that is discussed further in section 2.2.

Following the previously described assumptions and solving the respective equilibrium equations, Darnell, Tadmor, and Hyun all arrive at a final equation of the form,

$$\sigma = \sigma_0 \exp \left[ \frac{KB_1 - A_1}{KB_2 - A_2} L \right] \quad (1)$$

and Campbell arrives at the following form,

$$\sigma = \sigma_0 \exp \left[ \frac{L}{A_2} [-A_1 + B_1 - B_2] \right] \quad (2)$$

where  $\sigma$  is the major principal stress,  $\sigma_0$  is the initial major principal stress at the screw inlet,  $L$  is the axial length of the screw, and  $B_1, A_1, B_2, A_2$  and  $K$  (not the Janssen coefficient) are each different combinations of material properties (internal friction angles, screw surface friction coefficients, Janssen coefficients, etc.) and screw geometry (screw pitch, radius, flight thickness, etc.) that are unique for each model.

It is important to note that although the forms of the Darnell, Tadmor, and Hyun models are the same and Campbell's result is similar, each of these models can produce significantly different predictions of stress depending on the material and screw geometry being analyzed. However, Hyun et al. (1997) show through experiments that for the same material properties, their prediction for the evolution of the principal stress fits between the Darnell model and Campbell model, which underpredict and overpredict the flow rate-discharge pressure relationship, respectively. Although the growth of stresses within a screw subject to backpressure has been observed in experiments (Patterson, 2014), directly measuring the stresses is challenging.

The models described heretofore have focused on the solids conveying region of melt extrusion feed screws, the next section focuses on work outside of plastic extrusion. Similar modeling techniques have been used by researchers that focus on conveying of materials that remain solid for the entire conveying process. This work is largely parallel to what has been done in plastic extrusion and is presented in the following chapter.

### 2.1.2 Torque Models for a Screw Feeder

In addition to predicting the stress evolution within screw feeders, models have been developed to calculate their operational torque (Dai & Grace, 2008a; Metcalf, 1965; Yu & Arnold, 1997). These models operate on many of the same assumptions as the stress evolution models, and many are experimentally verified. Unfortunately, though, the models do not address feeding material into a backpressure and their predictions cannot be directly used to predict the behavior of compression screw feeders.

The earliest applicable effort to predict the torque required to drive a screw feeder was performed by Metcalf in 1965. Metcalf developed a feed screw torque model for a coal screw

feeder, and with experiments, tested it against the model developed by Darnell and Mol (1956). Metcalf asserts that all the torque is generated by the leading flight face and that the torque and axial force on the leading flight face are both proportional throughout the length of the screw. His final expression for the feeder torque (Eq. 5 in his analysis) is,

$$Torque = P_{hopper}Lbt\bar{r}_{face} \exp(Y\Psi) \quad (3)$$

where  $P_{hopper}$  is the vertical hopper stress above the feed screw inlet,  $L$  is the length of the screw,  $b$  is the number of leading flight faces,  $t$  is the thickness of the screw flight,  $\bar{r}_{face}$  is the average radius of the flight face,  $Y$  is a geometric and material property term, and  $\Psi$  is the angle between the leading flight faces. Metcalf noted that his equation differed significantly from Darnell's and pointed out that Darnell's equation did not agree well with Metcalf's experiments. However, Metcalf found good agreement between his model and his experiments when conveying coal in his experimental setup.

Instead of considering the torque to be fully dependent on the driving face like Metcalf, Yu and Arnold (1997) developed expressions for the individual force contributions to the screw torque for each face, and then applied each of them uniformly on the driving flight face. These expressions involve geometry, material properties, and an assumption for the evolution of stress between the leading and trailing flight within a screw pitch shown in Figure 2.5. Figure 2.6 shows the material element considered by Yu and Arnold (1997). Their analysis results in the torque required to drive a single pitch and is then multiplied by the total number of pitches to calculate the total torque required. Their model does not allow for the material stress to increase over the length of the screw, and therefore not be used in systems where the pressure changes significantly from the hopper to the outlet. Their final form is,

$$Torque = n_c T_c \quad (4)$$

where  $n_c$  is the number of pitches, and  $T_c$  is the torque required to drive a single pitch involving geometry, material properties, and the hopper stress.

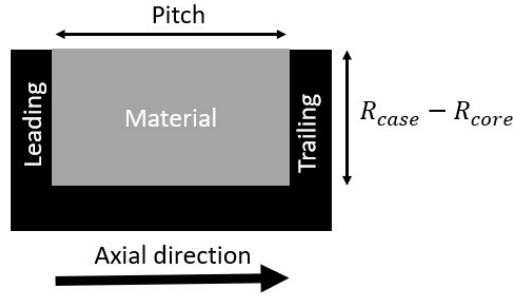


Figure 2.5: Material in a screw pitch considered by Yu and Arnold (1997).

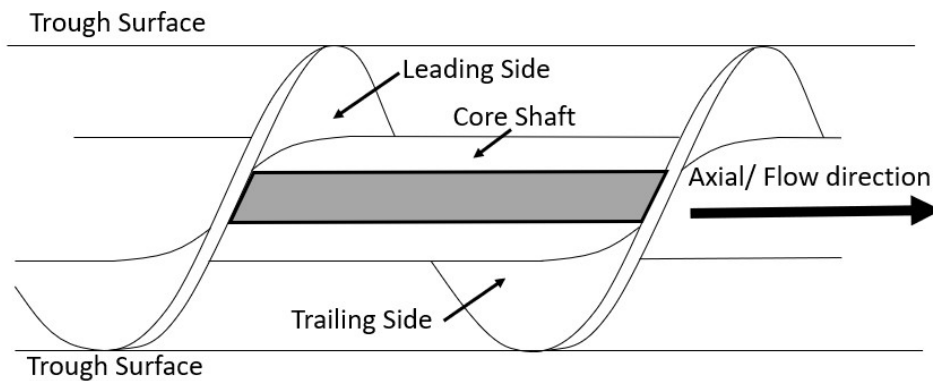


Figure 2.6: An Element of material within the screw pitch considered by Yu and Arnold (1997).

Dai and Grace build on the work of Metcalf and Yu, developing a torque model for biomass screw feeding that includes a converging outer case and material densification (Dai & Grace, 2008b, 2008a). However, their model does not include feeding into a backpressure, and their predicted torque is instead proportional to the hopper outlet stress. As with Yu and Arnold's solution, the stress does fall exponentially from the leading edge to the trailing edge within the screw flight, but the stress at the leading edge does not change with axial position. This approach leads to a form like Equation (3).

Experiments have been performed to understand relationships between flow rate, hopper stress, screw speed and other screw feeder properties (Carleton et al., 1969; George J. Burkhardt, 1967; Metcalf, 1965) and to test the existing models (Dai & Grace, 2008b; Yu & Arnold, 1997), but all experimental setups used when conveying biomass or other applicable materials used an open outlet condition, which is not representative of a compression screw feeder. However, the existing models show good agreement with experimental results, suggesting that the technique of

individually calculating torque contributions for each screw face is reasonable. All past works conclude that the development of analytical models can reveal relationships between different screw feeder properties and the behavior of the system. Dai and Grace conclude, in contrast to Yu and Arnold, that the fully encased region of the screw downstream from the hopper section (referred to in their work as the choke section) is the most important section and accounts for the largest percentage of the total torque. Their model also predicts that longer choke sections with smaller clearances will increase the screw torque, and this is confirmed by their experiments. This effect will become even more important when examining compression screw feeders subject to a backpressure.

## **2.2 Compressed Bed Models**

The term “compressed bed model” is a generic term used to describe a class of mechanistic or semi-mechanistic models that seek to describe the internal stresses of a bed of particulate material under a compressive loading with various boundary conditions. Research can be found on the development of analytical models to describe flow fields and stresses in hoppers, silos, and bunkers (Janssen, 1895; McNab & Bridgwater, 1979; Nedderman, 1992; Walker, 1966; Walters, 1973), and comparisons to experiments (Liu & Yeung, 2008; Ovarlez & Clément, 2005; Vanel et al., 1999; Wambaugh et al., 2010) and discrete element simulations (González-Montellano et al., 2012; Landry et al., 2004; Landry et al., 2003) have been made. These works are mainly focused on developing and testing models to predict material stresses, hopper mass flow rates, critical flow criteria, and stresses at the confining boundaries.

In 1895, H.A. Janssen studied the stresses on the side walls and the base of a vertical, cylindrical silo filled with corn. Through experimental measurements, Janssen observed that as a silo is filled, the pressure at the base initially increases and then saturates. He concluded that beyond a certain fill height, the friction against the vertical walls was able to fully support the weight of the added material, allowing the pressure at the base to remain constant as more material is added. Janssen then developed a model to describe this behavior in cylindrical containers, starting with the following assumptions:

- 1) friction is fully mobilized at the walls,
- 2) the stresses are uniform across any horizontal cross-section,

3) the vertical (axial) stress and the horizontal (radial) stress are principal stresses.

These assumptions have been shown to be incorrect in many cases (Nedderman, 1992; Sperl, 2006), but Janssen is still able to predict the vertical stress at a depth in a granular material with reasonable accuracy in his experiments.

Janssen’s analysis, called the “Method of Differential Slices” (Hancock, 1970), involves performing a force balance on a differential element of material and then solving the resulting differential equation to determine an equation for the vertical stress evolution along the axis in a silo. In Janssen’s case, the side-view of the differential element takes the shape shown in Figure 3.1.

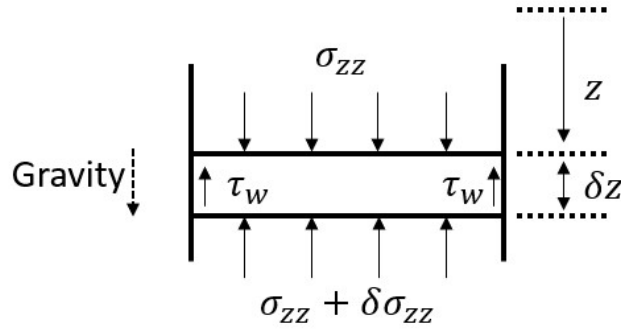


Figure 2.7 The differential element considered by Janssen. This shows the side-view of a disk of material subject to shear forces at the outer edge, material stress from above and below, and a gravitational force.

Janssen assumes static equilibrium of the system and balances the forces in the  $z$ -direction,

$$\Sigma F_z = \sigma_{zz}A_z - \tau_w A_w - (\sigma_{zz} + \delta\sigma_{zz})A_{z+\delta z} = 0 \quad (5)$$

where  $\sigma_{zz}$  is the axial stress,  $\tau_w$  is the shear stress acting in the  $z$ -direction along the circumference of the disk, and  $z$  is the depth of the material in the silo. Janssen then performs two important substitutions. The first substitution he makes relates  $\tau_w$  to  $\sigma_{zz}$ , applying the following relationship for a cohesionless material,

$$\tau_w = \mu_w \sigma_{rr} \quad (6)$$

where  $\sigma_{rr}$  is the stress normal to the wall (in the radial direction), and  $\mu_w$  is the wall friction coefficient. The second substitution comes from noticing that for cohesionless materials, assuming

that  $\sigma_{zz}$  and  $\sigma_{rr}$  are principal stresses, their ratio is a constant (Nedderman, 1992). This ratio takes the form,

$$\sigma_{rr} = \sigma_{zz}K_r \quad (7)$$

where  $K_r$  is known as a ‘‘Janssen Coefficient’’. The Janssen coefficient is an important simplification that allows Janssen’s mathematics as well as those found in Chapter 3.2 of this thesis to be easily solvable. Additionally, once an expression for the change of  $\sigma_{zz}$  is calculated, the relationship can easily be converted to express the change in  $\sigma_{rr}$ .

When performed for a cylindrical silo (Nedderman, 1992) Janssen’s equation takes the form,

$$\sigma_{zz} = \frac{2\gamma R}{4\mu_w K_r} \left( 1 - \exp \left[ -\frac{4\mu_w K_r}{R} z \right] \right) \quad (8)$$

where  $\gamma$  is the specific weight of the material,  $R$  is the radius of the silo,  $\mu_w$  is the coefficient of friction between the material and the silo walls,  $K_r$  is the Janssen Coefficient, and  $z$  which is the depth into the material from the free surface.

Janssen’s work is still the subject of comparisons between models, experiments, and simulations. One of the major reasons for these comparisons is that, although improvements and modifications to his model have been made and are discussed in the following paragraphs, none of them have gained wide appeal due to the added complexity of the resulting equations (Landry et al., 2004; Nedderman, 1992). For the current work, it is also important to note that many of the discrepancies found between Janssen’s approach and experimental results are because wall friction is not fully mobilized (Landry et al., 2004). In an operational screw feeder, however, wall friction is known to be fully mobilized and therefore the method that Janssen uses in his analysis is suitable.

Walker improved on Janssen’s analysis by relaxing assumptions 2 and 3 above listed at the start of Section 2.2 (Walker, 1966). His major contribution was introducing a ‘‘distribution factor’’ that describes the ratio between the average axial stress on the whole bed cross-section and the axial stress at the walls (maximum radius) of the hopper,

$$\mathcal{D}_{wall} = \frac{\sigma_{zz}|_{r=wall}}{\bar{\sigma}_{zz}} \quad (9)$$

where  $\sigma_{zz}|_{r=wall}$  is the axial stress at a radius “r” from the centerline of the hopper, and  $\bar{\sigma}_{zz}$  is the average axial stress on the cross-section. Using this substitution Walker arrives at an equation like Eq. (8) but with his added property  $\mathcal{D}$ ,

$$\bar{\sigma}_{zz} = \frac{\gamma R}{2\mu_w K_r \mathcal{D}} \left( 1 - \exp \left[ -\frac{2\mu_w K_r \mathcal{D}}{R} z \right] \right) \quad (10)$$

He also adds critical insight from the theory of soil mechanics and includes the Mohr-Coulomb failure criterion in his analysis to remove the Janssen coefficient entirely, modifying Equation (10),

$$\bar{\sigma}_{zz} = \frac{R\gamma}{2B\mathcal{D}} \left( 1 - \exp \left[ -\frac{2B\mathcal{D}}{R} z \right] \right) \quad (11)$$

where R is the cylindrical column radius, B is a parameter calculated for a Mohr’s circle analysis from material properties, and all other variables from Eq. (10) remain the same. Removing the Janssen coefficient by using Mohr-Coulomb failure theory provides a more mechanistic problem solving approach, and including the distribution parameter acknowledges that the stress on the cross-section is not uniform. In applications where predictions of boundary stresses are important  $\mathcal{D}$  becomes necessary to correctly define the material behavior at the walls. Additionally, other works realized the need for this parameter, and many sources concluded that more analytical and experimental work was necessary to evaluate  $\mathcal{D}$  (McNab & Bridgwater, 1979; Nedderman, 1992).

The distribution parameter was especially important for McNab and Bridgwater in 1979 while investigating the stresses in spouted cylindrical hopper beds (McNab & Bridgwater, 1979). They applied the same method as Janssen and Walker, but used an annular-shaped differential element that contacts the hopper at the outer edge, and an air stream at the inner edge. Figure 2.8 shows the shape,

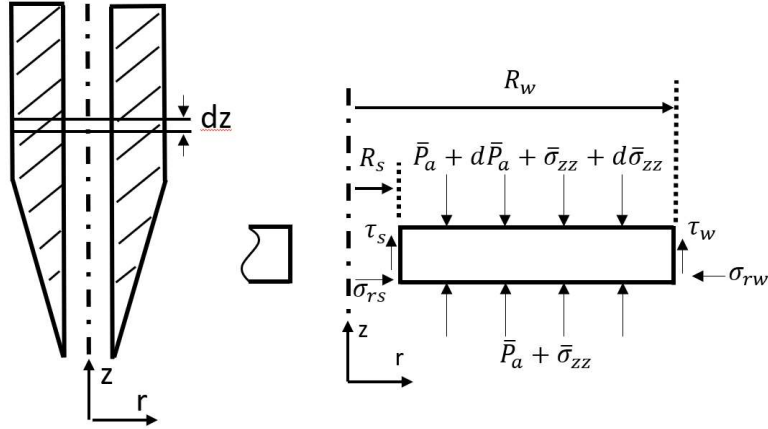


Figure 2.8 Differential element used by McNab and Bridgewater. Their differential element is valid immediately after a spouted bed forms and fluid is exerting a shear force on the inner face of the annulus of material.

where  $\bar{\sigma}_{zz}$  is the average axial stress on the annulus face,  $\sigma_{rw}$  is the normal stress on the vertical wall,  $\tau_w$  is the vertical shear stress at the wall,  $\tau_s$  is the vertical shear stress at the spout,  $\sigma_{rs}$  is the normal stress at the spout,  $\bar{P}_a$  is the hydrostatic fluid pressure,  $R_s$  is the inner radius of the annulus, and  $R_w$  is the outer radius of the annulus. If the fluid pressure is ignored, and all material properties are taken to be constant, the analysis leads to the following equation:

$$\bar{\sigma}_{zz} = \bar{\sigma}_{zz,0} \exp \left[ \frac{\psi_w D_w R_w + \psi_s D_s R_s}{R_w^2 - R_s^2} z \right] \quad (12)$$

where the new parameter  $\psi_a$  is a material property that is described in detail in later sections. Apparent here is also a difference in the form of the equation. Depending on the boundary conditions and loading situation, it is possible to apply their analysis to many different situations. This difference is summarized in Figure 2.9.

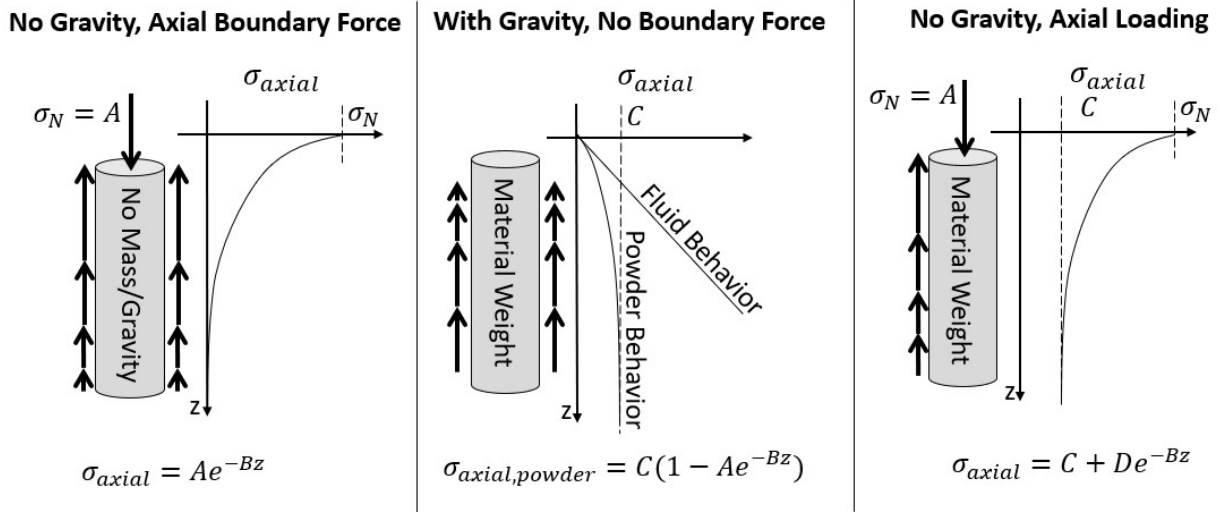


Figure 2.9 Axial stress solutions for a confined vertical column of material. This figure shows all solution forms resulting from considering a column of material subject to boundary conditions and body forces.

Janssen and Walker include gravity, but assume that the material does not have an additional boundary force applied to the top and, therefore, they both arrive at the form in the center of Figure 2.9. McNab & Bridgwater arrive at the form on the right side because their analysis includes an additional axial loading term caused by the fluid pressure.

Up to now, only hoppers and silos of constant cross-section have been discussed. However, in compression screw feeders it is not uncommon to find annular sections with changing cross-sections and the stress predictions in these regions are critical as well. Walker and McNab & Bridgwater were also interested in hoppers with variable geometry, and both extended their analyses to include the effects of a variable outer hopper radius. This analysis is similar to what is discussed in Chapter 5.2.1.

Unfortunately, although the new models provide estimations of axial stress, radial stress, and shear stress at different heights and radii in silos and hoppers, the available experimental measurements are limited. Much of the work performed by and described in (Liu & Yeung, 2008; Ovarlez & Clément, 2005; Vanel et al., 1999; Wambaugh et al., 2010) only compares the axial stress profile of the silo, whereas the current work is also interested in assessing the ability of the past models to predict other stress components.

### 2.3 DEM Modeling of Screw Feeders

The discrete element method (DEM) has proven to be a useful tool in modeling systems where particle scale effects are important, and screw feeders are one of these systems. Moysey et al. (2004) used DEM to study velocity fields and pressure evolution in screw feeders. Their contributions include motivating the need to use three-dimensional simulations, explaining the loss in computational efficiency compared to the finite element method (FEM), and explaining the importance of capturing particle shape effects (Moysey & Thompson, 2004). Another significant contribution is the simulation of screw extruders using a restricted outlet condition. They use a “torpedo style” boundary condition (described later in this section) to generate a backpressure and compare the pressure growth in the system to an equivalent system with an open outlet condition. For the open condition the pressure was not found to change significantly from hopper to exit, but for the restricted outlet condition the solid stress in the material was found to monotonically increase from hopper to outlet.

Moysey et al. continued their analysis, focusing on solids compaction in the solids conveying zone of a single screw extruder (Moysey & Thompson, 2008). This work investigates how the measured pressures and bulk densities in simulations of screw extruder compared to simulations of a simple compaction cell (Figure 2.10), and compares to the trends predicted by Darnell et al. (1956). Firstly, they conclude that the pressure growth in their screw extruder did not follow the exponential trend predicted by Darnell et al. (1956). Additionally, they found that although the material within the screw flights was in an anisotropic state of stress, the pressure at the screw shaft and the advancing flight are close in magnitude over a wide range of pressures. Further, their simulations showed that the pressure at the trailing flight is almost an order of magnitude smaller than the pressure at the advancing flight. These conclusions represent a significant step toward understanding the evolution of the state of stress of material within a screw feeder.

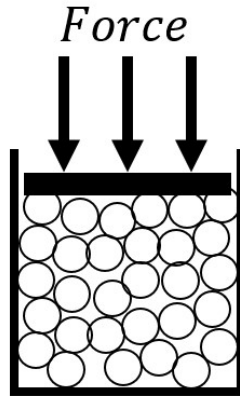


Figure 2.10: Simple compaction cell showing confined particles subject to a punch-and-die type loading.

Although Moysey and Thompson’s work is directly applicable to a compression screw feeder, there have been other works that contribute to the body of simulation work surrounding screw feeders. Owen et al. (2009) studied the relationship between screw conveyor mass flow rate, power, screw speed, and angle of screw inclination using DEM, but their application did not include analysis of a restricted outlet or a full screw flight cavity. Hou et al. (2014) studied how cohesion affected flow patterns, velocity fields, and drawdown characteristics screw feeder systems using DEM. However, their application was also surrounding high screw speeds and a loosely packed screw cavity without backpressure. Michelangelli et al. (2014) studied the influence of particle-case friction on the relationship between flow rate and screw speed relationship. However, with a coarse mesh, large particles, and little information provided about the backpressure characteristics of their simulation, their conclusions do not apply to the current work.

Applying stress-based boundary conditions in DEM is often challenging, requiring either a physical body to interact with the DEM particles to generate a desired stress, or additional body forces to be defined for particles in a certain region. Previous works regarding screw behavior have developed two methods to apply a backpressure to a screw system: the “torpedo” method and the “force field” method. In the torpedo method, a bullet-shaped solid body is placed at the outlet of the screw feeder, leaving a gap smaller than the particle size that particles must pass through to exit the system (Figure 2.11). The drawback of this strategy is that the backpressure is influenced by simulation inputs that makes the gap harder or easier to cross (gap size, particle size, size distribution, friction coefficients, particle stiffnesses, etc.). However, this method is still popular,

as it is one of the ways that backpressure is generated in experiments (Moysey & Thompson, 2004, 2008).

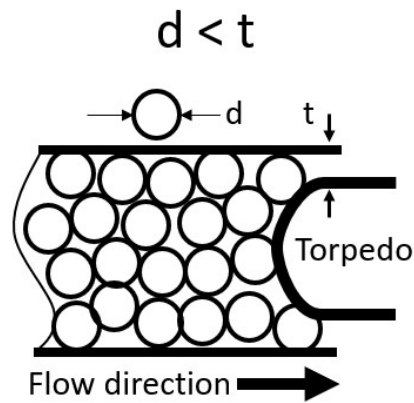


Figure 2.11: Torpedo outlet boundary condition found in experiments performed by Moysey et al., (2004).

The force field method has become more popular in recent works due to its ability to decouple the boundary pressure from the material properties (Lessmann & Schoeppner, 2015, 2016; Trippe & Schöppner, 2018). In this method, a region is defined at the exit of the screw that will apply a body force to all particles that lie within it (Figure 2.12). This approach has been a successful method for applying outlet stresses that are independent of material interaction properties, but depending on the particle, determining the correct force to achieve a desired pressure could be challenging. However, in addition to decoupling material properties from the outlet stress, the force field method also generates a uniform and steady stress within a region.

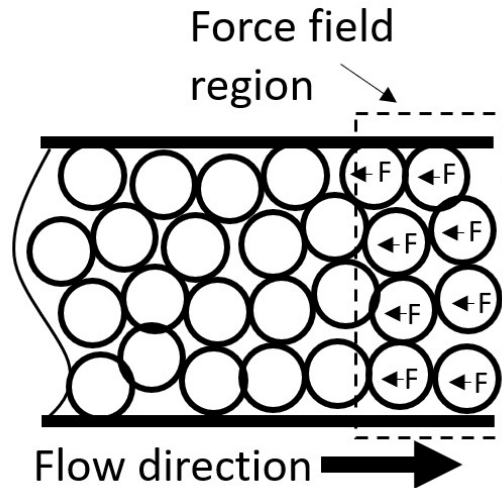


Figure 2.12: Force field boundary condition that allows for a pressure boundary condition that is decoupled from material properties. The applied pressure depends on the magnitude of the force field, and the cross sectional area of the channel in the flow direction.

## 2.4 Literature Summary

First, previous models for material stresses and screw torque for screw feeders and screw extruders were reviewed and the major conclusions were presented. For screw extruders, a differential analysis predicts an exponential growth in the principal stress within the screw flights. For screw feeders, the geometry, hopper stresses, and material properties were studied to develop predictions of the operating torque when subject to an open-outlet boundary condition for a variety of materials.

In addition to leaving out backpressures, the screw models did not consider the plug section that is found in compression screw feeders. Therefore, models that predict the evolution of the state of stress inside confined columns were also presented. The axial stress is predicted to grow exponentially from the backpressure, and the state of stress is predicted to be anisotropic. However, although the resulting models performed reasonably well when compared to existing data, more experimentation is required to confirm many of the conclusions from the compressed bed models.

Finally, existing works regarding DEM models of screw systems were discussed and their conclusions were analyzed. DEM models of screw feeder systems have given insight into the relationships between pressure and axial position, pressure, and position within the screw flight, screw speed and mass flow rate, and more. The major conclusion from the DEM work is that the pressure growth in a screw with a restricted outlet condition is not purely exponential. This finding

is contradictory to the screw section models presented in the literature and requires more analysis to understand why.

### **3. OBJECTIVES**

The goal of this thesis is to provide a better understanding of compression screw feeders, in order to improve the economic viability of biomass as an energy source in the U.S. by developing predictive models for biomass feeding. Predictive tools will aid in efficiently designed and reliable biorefinery equipment. To help achieve this goal, the objectives of this thesis work are:

- 1) Develop DEM models to predict material behavior in different regions of a compression feed screw
- 2) Utilize DEM to inform the development of analytical models that can make rapid predictions of screw torque and solid stress within the screw
- 3) Establish a method for determining model input parameters
- 4) Compare the analytical models against DEM results

## 4. DEM MODELS

The commercial Discrete Element Method solver, Rocky DEM © and the Python API available within the software have been used in all simulations. The proceeding paragraphs describe the force models, simulation setup, and material properties used to analyze a compression screw feeder.

### 4.1 Force Models

Standard force models are available in Rocky DEM and are used to model normal and tangent interactions between particles. The biomass is represented using irrotational, polydisperse spherical particles on a similar size scale as milled corn stover used in a pilot scale facility. Figure 4.1 shows the two force models used in the DEM simulations.

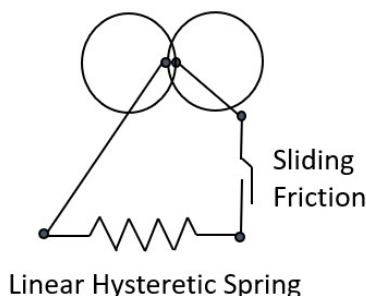


Figure 4.1: Contact model used in all DEM simulations. A linear hysteretic model is coupled with a simple Coulomb friction model. Particles subject to this contact model cannot store elastic energy in their tangential contacts.

Missing from Figure 4.1 are two forces commonly investigated in simulations: a model of rolling resistance and a model of cohesion. The current work does not consider rolling due to the non-spherical shape of milled corn stover and the highly compact nature of the material in the screw. Rather than rolling past each other, particles are confined and tend to slip instead. Additionally, because of the magnitude of the compressive forces and stresses being considered in this work, small cohesive forces are assumed to provide a negligible contribution to the total energy dissipated by the system. Therefore, normal and tangent interactions are assumed to dominate the behavior of the screw feeder.

The normal force model used in all simulations is the linear hysteretic spring model, proposed by Walton & Braun (1986). This model is a linear model that approximates elastoplastic normal interactions with the following formulation;

$$F_n = \begin{cases} K_{loading}s_n & \text{if loading} \\ K_{unloading}(s_n - s_0) & \text{if unloading} \end{cases} \quad (13)$$

where  $K_{loading}$  is the stiffness of the contact if the particles are moving towards one another,  $K_{unloading}$  is the stiffness if the particles are moving apart,  $s_n$  is the amount of overlap between the particles, and  $s_0$  is the peak overlap during the loading-unloading cycle. The parameters  $K_{loading}$  and  $K_{unloading}$  are further defined as,

$$\frac{1}{K_{loading}} = \frac{1}{E_1L_1} + \frac{1}{E_2L_2} \quad (14)$$

$$K_{unloading} = \frac{K_{loading}}{\epsilon^2} \quad (15)$$

where  $E_1$  and  $E_2$  are the Young's moduli of the interacting bodies (the bulk Young's modulus for particles, and the true Young's modulus for boundary elements),  $L_1$  and  $L_2$  are the diameters of the interacting bodies, and  $\epsilon$  is the coefficient of restitution of the body.

During a contact event, Rocky first determines the normal force and then calculates the magnitude and direction of the tangent force using the calculated normal force. For the current work, the Coulomb limit model is used. All stresses and torques measured in this work have shown strong sensitivity to the tangent force model and in the future, a more realistic model should be used. The Coulomb limit model is defined with the following equation;

$$F_t = -\mu F_n \hat{s} \quad (16)$$

where  $F_t$  is the vector of the tangent force,  $\mu$  is the friction coefficient (in the current work, the dynamic and static friction coefficients are taken to be the same), and  $\hat{s}$  is the unit vector pointing in the direction of the relative velocity of the contact. This model does not allow for the coefficient

of friction to change based on the normal force and provides only a simplified prediction of frictional behavior. Although the applied contact models are simple, they allow for faster simulations and provide a first step toward modeling biomass.

## 4.2 Screw Simulations

The subject of this section is the compression screw feeder geometry (shown in Figure 4.2). First, the geometry, setup, and simulation inputs are discussed and then the results are presented.

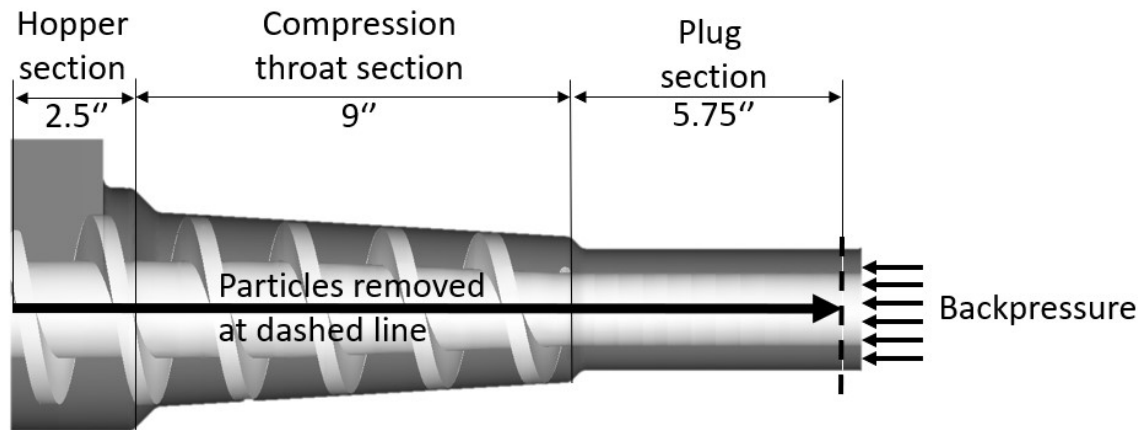


Figure 4.2: Screw simulation overall geometry. The three major sections of a compression screw feeder are the hopper section, the compression throat section, and the plug section.

### 4.2.1 Geometry, Setup, and Inputs

The geometry in Figure 4.2 shows the three distinct sections of a compression screw feeder. Firstly, the hopper section is characterized by an open inlet where material can enter the system. Here, the purpose of the screw flight is only to convey the material forward. Secondly, the compression throat section is characterized by a converging outer case, causing the material to be compressed. In this region, without the frictional force against the case, the material in the screw flight would rotate with the screw. However, the friction with the case resists this rotation and presses the material against the leading screw flight, causing the material to be conveyed forward. Finally, after the screw flights end, the material passes through the plug section of the screw system. The material in the plug section is slipping against the screw shaft and the screw case as the pressure from the screw flights conveys the material forward. Preliminary simulations showed that

sharp corners on the screw case caused numerical instabilities and needed to be removed. After performing the necessary simplifications, the detailed dimensions of the resulting screw geometry are shown in Figure 4.3 and Figure 4.4.

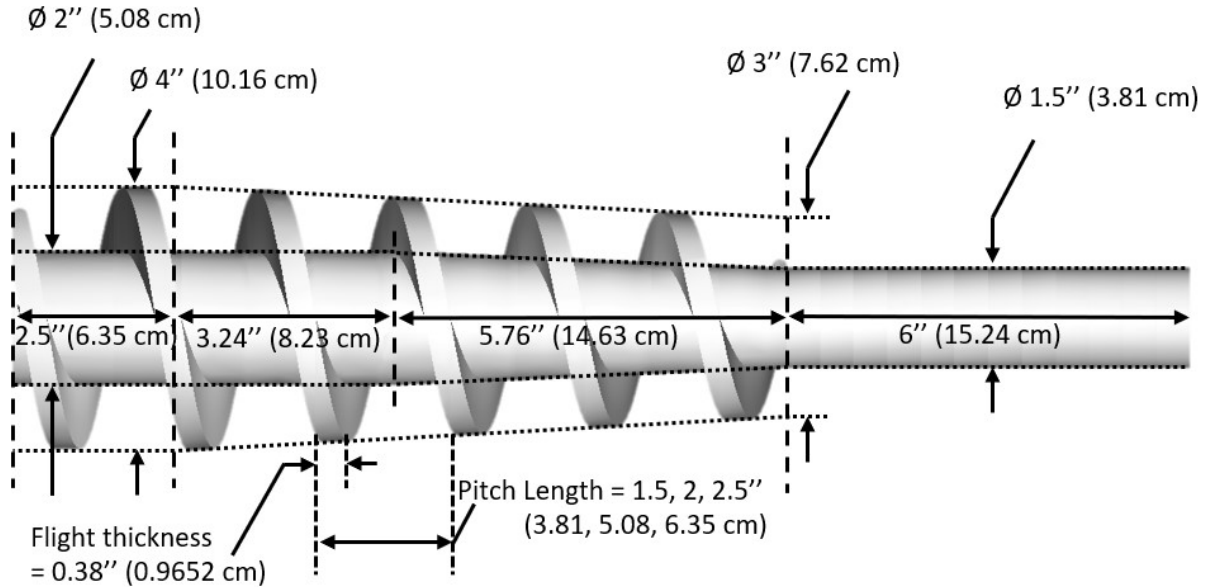


Figure 4.3: Detailed screw geometry. These dimensions are loosely based on a screw feeder assembly in a pilot scale facility at Idaho National Laboratory.

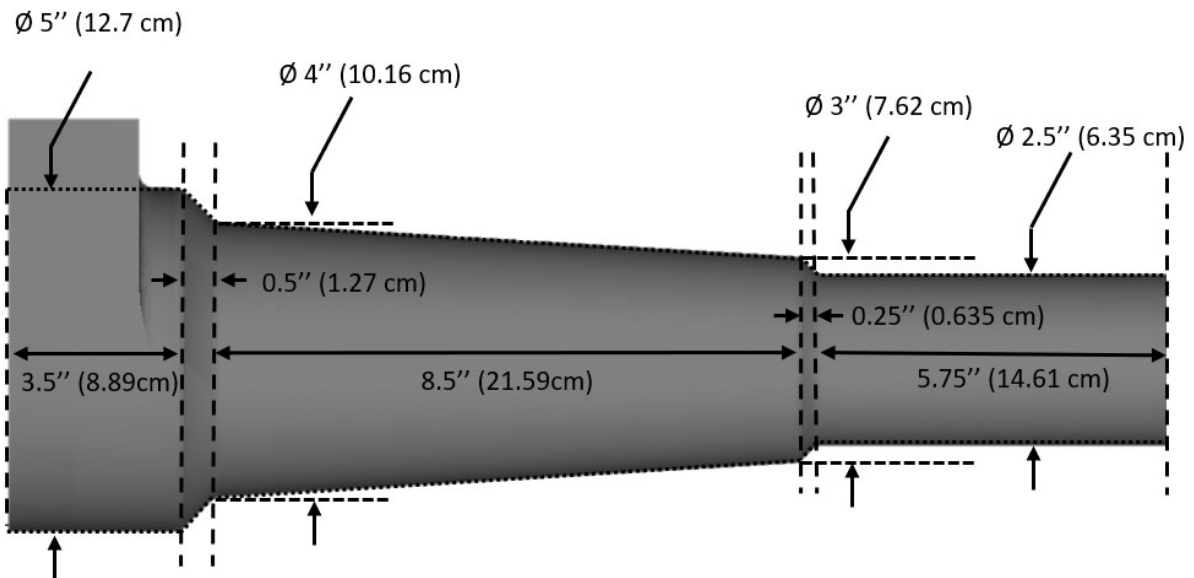


Figure 4.4: Divided case geometry. These dimensions are also loosely based on a screw feeder assembly in a pilot scale facility at Idaho National Laboratory, but have been simplified to remove sharp edges, corners, and pockets.

Once the geometry was chosen, two different simulation types were created. In one set of simulations the screw geometry was sliced into distinct axial segments (Figure 4.5), and in another set the different faces of the screw were separated into distinct bodies (Figure 4.6). The axially sliced simulations provide insight into which segments of the screw require the most torque to drive. The simulations with separate faces are useful in informing the model development, as they show which screw faces require the most torque to drive. The sliced screw components are then rotated together to provide a kinematically equivalent system to the unsliced screw (Figure 4.5), and the total torque can be calculated by summing each of the individual components. One of the major insights gained from this analysis was the realization that the screw segments in the hopper section contributed a low percentage (<5%) of the torque to the system when there was backpressure applied. The geometry was meshed in Autodesk Inventor © with the mesh properties shown in Table 4.1. Although the mesh shown in Figure 4.7 is not highly refined, the simulation results showed little sensitivity to further reductions in mesh size.

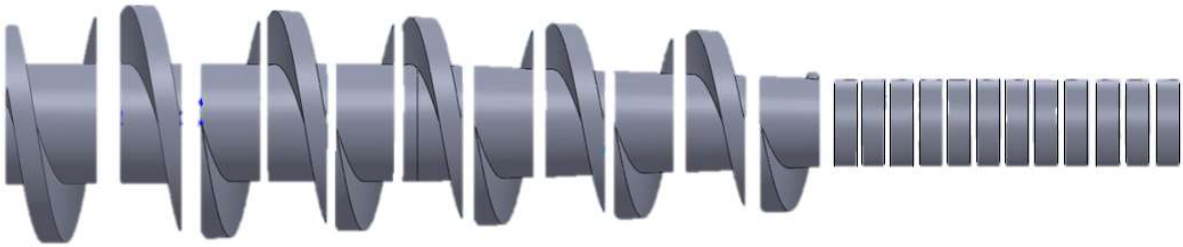


Figure 4.5: Sliced screw geometry. When each slice is rotated together, this geometry behaves the same as a single screw body but allows for DEM results to be extracted from each slice individually.

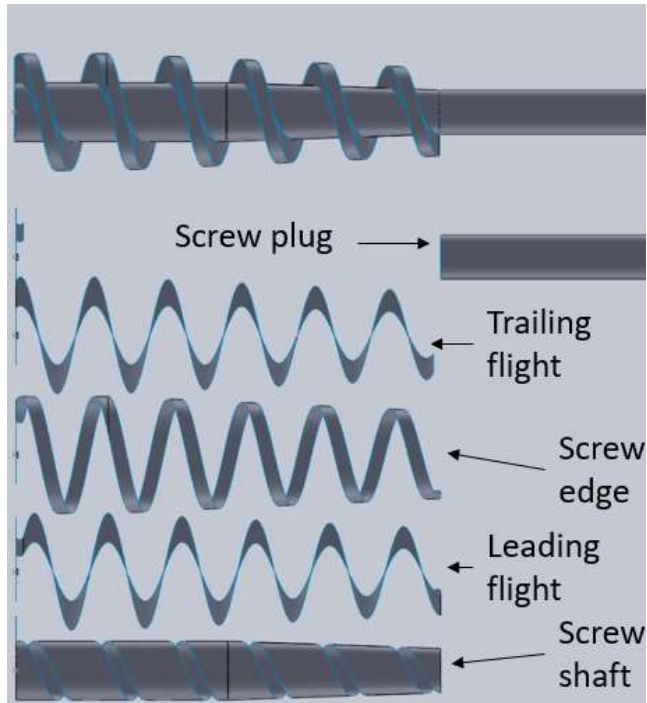


Figure 4.6: Screw geometry with separate faces. When each screw face is rotated together, this geometry behaves the same as a single screw body but allows for DEM results to be extracted from each slice individually.

Table 4.1: Autodesk Inventor STL mesh properties. These properties were tuned to create a balance of mesh refinement and computational efficiency.

Mesh Property	Value
Maximum allowable surface deviation	0.663%
Maximum allowable normal deviation	11.94
Maximum edge length	100%
Maximum aspect ratio	2.31



Figure 4.7: The meshed surface of the screw. The mesh properties were chosen to avoid long, thin elements which adversely affect the way boundary forces are calculated within DEM.

In the current work, the boundary stress is enforced by placing a frictionless barrier at the outlet and applying a force to the barrier Figure 4.8. The particles advance naturally as the screw runs, but once their centers of mass pass a plane at the “exit” of the simulation (represented by the thin, black, dashed line in the figure) the particles are deleted (represented by steps 2 and 3). After the particles are deleted, there is a gap between the body used to apply pressure at the exit and the particles, and the body quickly accelerates to meet the particles again (steps 3 and 4). Using this boundary condition, the applied stress is only dependent on the boundary force. However, one drawback of this technique is that after particles are deleted from the simulation, there is a gap between the barrier and the particles (step 3 to step 4), and the particles experience no outlet stress during this time. This effect, shown in Figure 4.9, causes oscillations in the applied outlet stress.

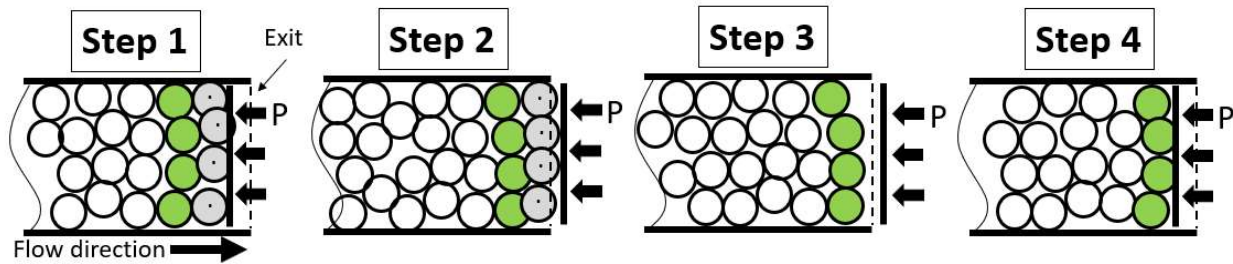


Figure 4.8: Outlet axial stress boundary condition. Step one shows a body (a thick black line) parallel to the exit that is allowed to move but subject to a boundary force,  $P$ . Steps 2, 3, and 4 show the boundary movement as the particles advance toward the exit.

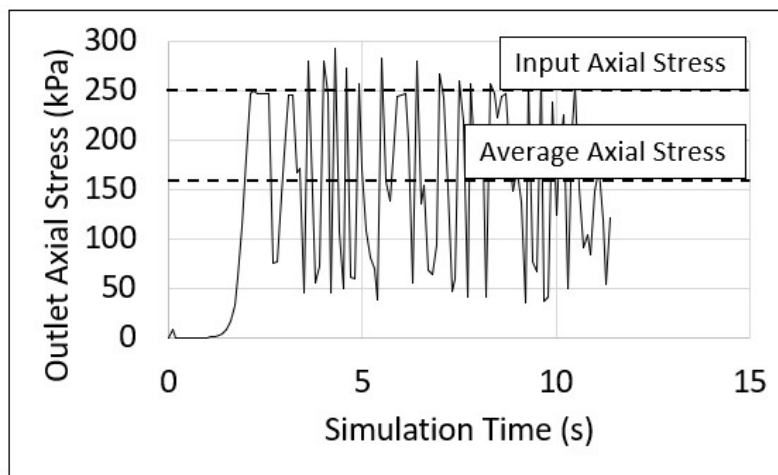


Figure 4.9: Oscillations of outlet axial stress are caused by the movement of the body at the exit of the screw feeder simulations that is used to apply a pressure. The average axial stress is much lower than the input axial stress.

Finally, it is important to discuss the DEM particle properties and the final simulation setup. Although corn stover is made up of mostly narrow rod-like particles and thin plate-like particles (Figure 4.10), the current work approximates tightly packed domains of material within the screw feeder as spheres. The spheres are given a size on the order of the real particle size (millimeters) with a narrow, uniform size distribution. This approach significantly reduces the time required to run the simulations but restricts the ability to investigate the effects of particle shape. In addition to using the Linear Hysteretic Spring model for normal interactions and the Coulomb Limit model for tangent interactions, a small gravitational force is used to direct the material downward in the hopper. Particles are input to the system before the first timestep by filling the entire void space between the screw and the case, and then injected into the hopper as needed to maintain a filled screw cavity for the duration of the simulation.

All pertinent material properties are summarized in Table 4.2. From a base set of input properties, three properties were chosen to be varied: screw pitch, outlet axial stress, and particle to particle coefficient of friction. These three properties were chosen to represent changes in screw geometry, boundary conditions, and material properties, respectively. In order to assess the sensitivity of the system to these properties, simulations were run using every combination of a high value, the base value, and a low value for each variable. Figure 4.11 shows the screw geometry full of particles at the first timestep.



Figure 4.10: Corn stover shape and size with a ruler for scale. The particles are mostly plate-like, with millimeter scale dimensions in two directions and tenths of millimeter dimensions in the third direction. Other particle shapes include narrow, rod-like particles with only a single dimension on the scale of millimeters, and brick-like particles with all three dimensions on the millimeter scale.



Figure 4.11: Compression feed screw simulation showing the particle fill at the initial timestep.

Table 4.2: Compression feed screw simulation input properties.

Input Parameter	Notation	Value
Outlet force (Backpressure)	$F_{outlet}$	250, 500, 1000 [N]
Screw rotational velocity	$\omega$	5 [radians/second]
Boundary Young's modulus	$E_{boundary}$	10 [GPa]
Boundary Poisson's ratio	$\nu_{boundary}$	.3
Particle bulk Young's modulus	$E_{particle}$	100 [MPa]
Particle Poisson's ratio	$\nu_{particle}$	.3
Particle density	$\rho_{particle}$	500 [ $\frac{kg}{m^3}$ ]
Particle-particle static friction	$\mu_{pp,static}$	0.25, 0.5, 0.75
Particle-particle dynamic friction	$\mu_{pp,dynamic}$	0.25, 0.5, 0.75
Particle-particle coefficient of restitution	$\epsilon_{pp}$	.3
Particle-boundary static friction	$\mu_{pb,static}$	0.4
Particle-boundary dynamic friction	$\mu_{pb,dynamic}$	0.4
Particle-boundary coefficient of restitution	$\epsilon_{pb}$	.3
Particle size range	d	2.5 – 3.0 [mm]
Particle distribution type	-	Uniform
Timestep	$\Delta t$	1e-6 s

## 4.2.2 Results

The pressure is measured in the simulations at various axial positions using a particle binning method. The measured value of stresses depended on the ratio of the bin size to the particle size and required time averaging to produce significant results. Approximately 50 particles resided

within the bin depending on the level of compaction, and 35 output timesteps were used to average the data ( $\sim 2.8$  screw rotations). In the screw section, a 10x10x10 mm bin was positioned in the center of the screw channel (Figure 4.12), and traced a helical path down the length of the screw (Figure 4.13). Along the helical path, the particle bin is rotated such that the radial stress ( $\sigma_{RR}$ ), shown in Figure 4.14, points directly away from the screw axis. In the plug section, an annular bin type was used with 25 tangential partitions (Figure 4.15), providing stresses over the entire annulus (Figure 4.16).

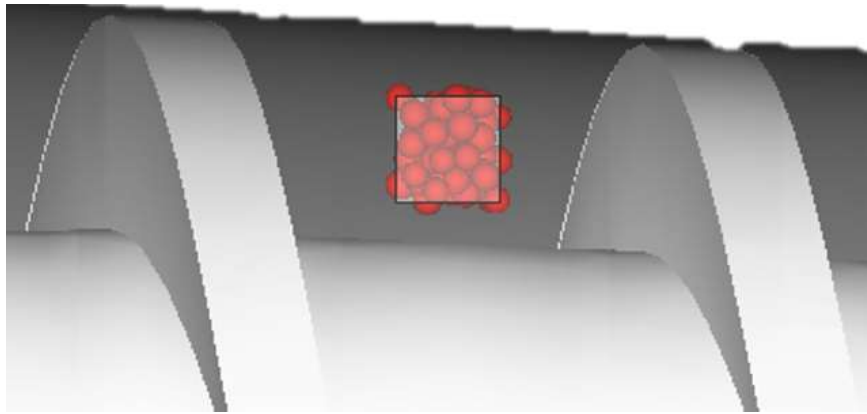


Figure 4.12: Particle bin in the screw channel. The bin is positioned so the center is between the outer case, the inner case, and each screw flight face.

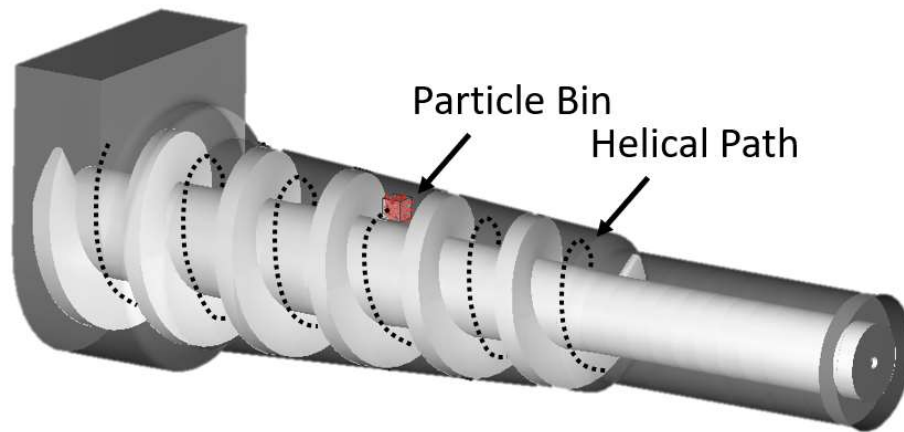


Figure 4.13: Particle bin path in the screw section. Along the helical path of the bin, the axial position is also recorded such that the axial stress progression can be measured.

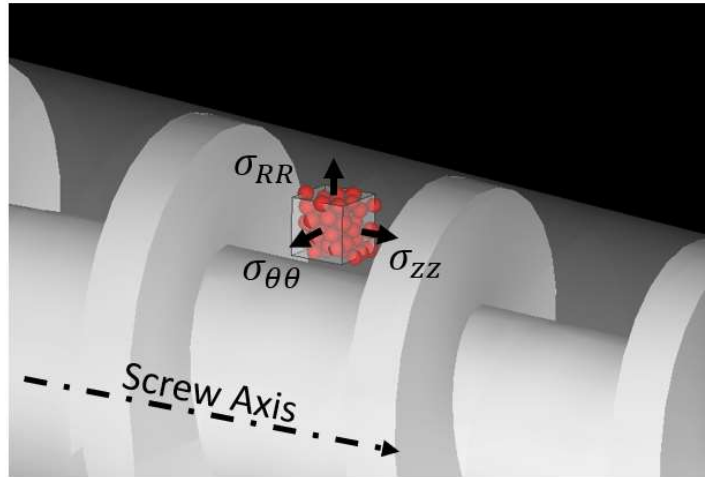


Figure 4.14: Particle bin stresses within the screw channel. To recover these stresses along the helical path, the bin must be rotated such that the face measuring the radial stress points directly outward from the screw axis.

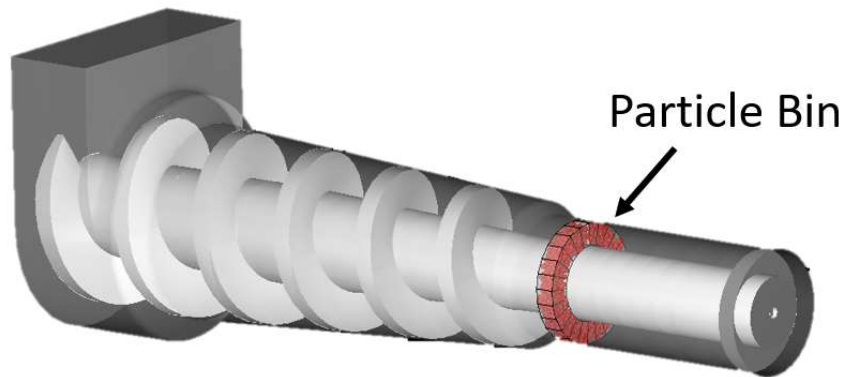


Figure 4.15: Particle bins in the plug section. The particle bin wraps around the entire annulus and provides average values of the stresses over the cross section.

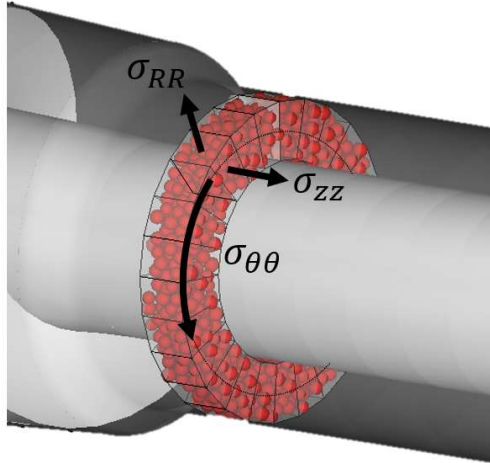


Figure 4.16: Particle bin stresses. Unlike the screw section, the particle bins in the plug section average the stresses over the entire annulus.

Unlike in experiments, the internal state of stress of material can be directly examined within DEM. Figure 4.17 shows that the DEM predicts, on average, a mostly hydrostatic stress state throughout the entire screw assembly which aligns with what Darnell et al. (1956) assumed. However, the stresses do not grow exponentially within the compression throat of the screw, contradicting Darnell et al. (1956). Within the plug section, the DEM predicts that all stresses are close in magnitude throughout the length, which is contradictory to the plug section literature (Nedderman, 1992; Walker, 1966; Walters, 1973a). The maximum difference between the pressure and any individual stress throughout the length is less than 10%, and therefore, the evolution of the pressure represents all other stresses well. Therefore, the pressure within the compression screw feeder is analyzed further.

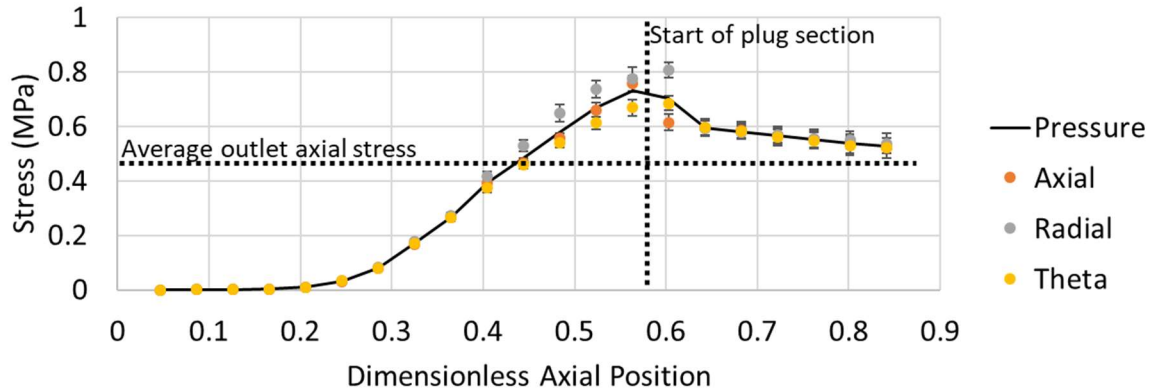


Figure 4.17: Comparison of solid stresses over screw length. The peak pressure is higher than the average applied outlet stress and is reached at the start of the plug section (end of the screw flights). The growth up to the start of the plug section is not exponential.

To further understand the pressure within the screw section, measurements were taken at the leading and trailing flight at different axial positions by placing a 10x10x10mm bin one particle diameter away from the surface (Figure 4.18). Figure 4.19 shows data taken from a simulation with a backpressure of 250 kPa, a 2" screw pitch, and a  $\mu_{pp}$  value of 0.5. The DEM suggests that the pressure near the trailing flight is of similar magnitude as the trailing edge, with larger percent errors at low pressures. The data also shows that the pressure at the trailing flight is larger than the leading edge, challenging the assumption made by Yu and Arnold (1997) which states that the axial stress within the screw channel decreases exponentially from the leading edge to the trailing edge.

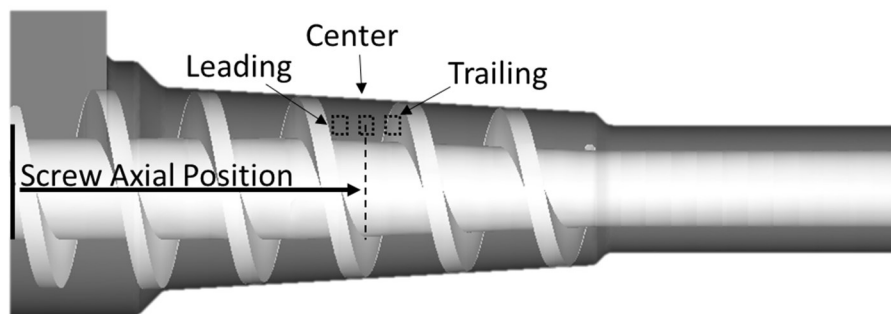


Figure 4.18: Bin positions for measuring pressure near the screw flights. The bin was moved as close as possible to the screw flight, but the closest edge remained one particle radius away.

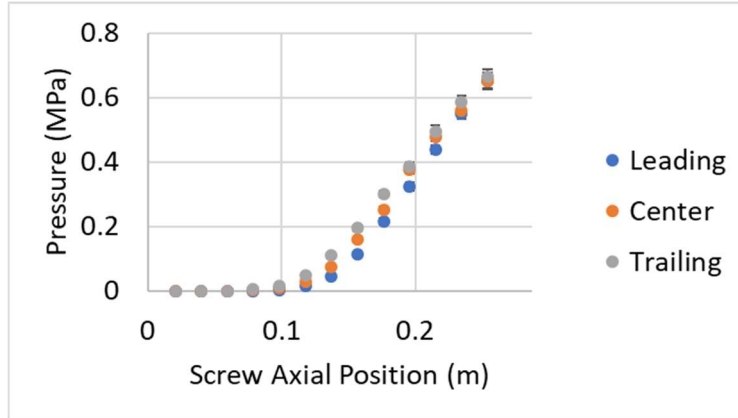


Figure 4.19: Pressure change from leading to trailing flight in the screw section, showing that the pressure near the screw flights is close to the average pressure measured in the center. In the highly compact region at the end of the screw flights, the pressures remain very close.

The next set of simulations studied the effects of screw pitch, applied backpressure, and particle-particle coefficient of friction on the pressure evolution (Figure 4.20). Figure 4.21 represents a subset of the data, also providing a 95% confidence interval. It is important to note that due to oscillations at the exit boundary condition, the achieved value of backpressure is always lower than the input value. Therefore, the pressure measured in the DEM simulations approaches the average applied outlet stress, not the desired outlet stress. Additionally, the oscillation causes the error bars to grow near the exit.

Figure 4.20 shows two distinct regions of monotonic behavior. The solid pressure starts at zero in the hopper section and grows to a peak value at the end of the screw flights in all cases. Further downstream, the material unloads as it passes into the plug section and the pressure slowly reduces due to friction with the outer case and screw shaft until the pressure approaches the outlet axial stress at the exit. Varying the backpressure has the most significant effect on the pressure evolution, shown in Figure 4.21 for one friction coefficient. This result represents a departure from what is predicted by the continuum models, as they suggest the pressure evolution in the screw section should be very sensitive to screw pitch and friction coefficient, with no sensitivity to backpressure (Campbell & Dontula, 1995; Darnell & Mol., 1956; Hyun & Spalding, 1997). Additionally, the pressure does not grow exponentially, and does not exhibit smooth growth at high pressures. Finally, the transition from the screw section into the plug section is accompanied by a transition in loading, as material within the screw flights is loaded as it travels towards the exit, but material in the plug section is being unloaded.

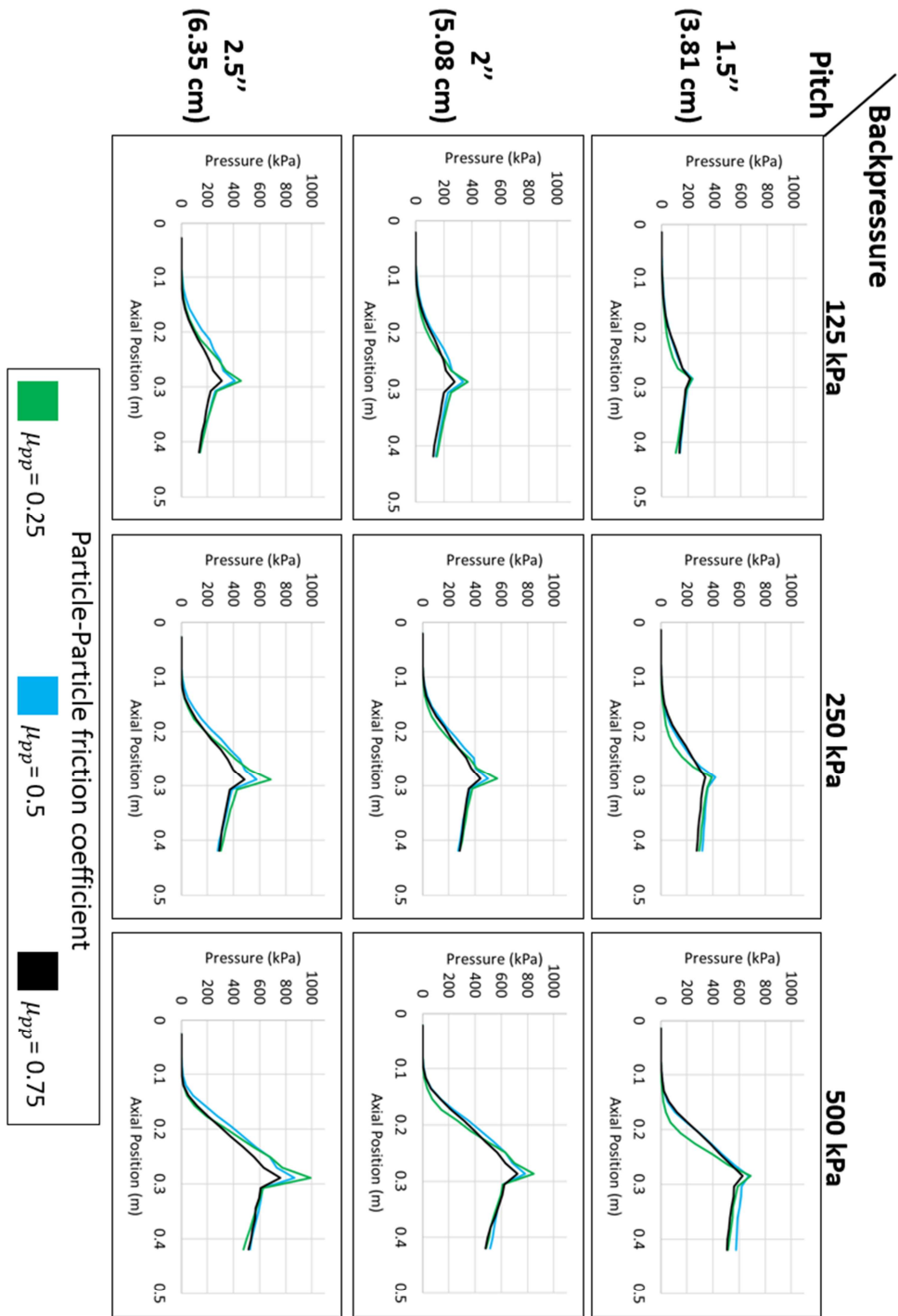


Figure 4.20: Screw pressure vs. position, backpressure, pitch, and particle-particle friction coefficient. These results represent a preliminary parametric study and only include the parameters that were hypothesized to be the most important.

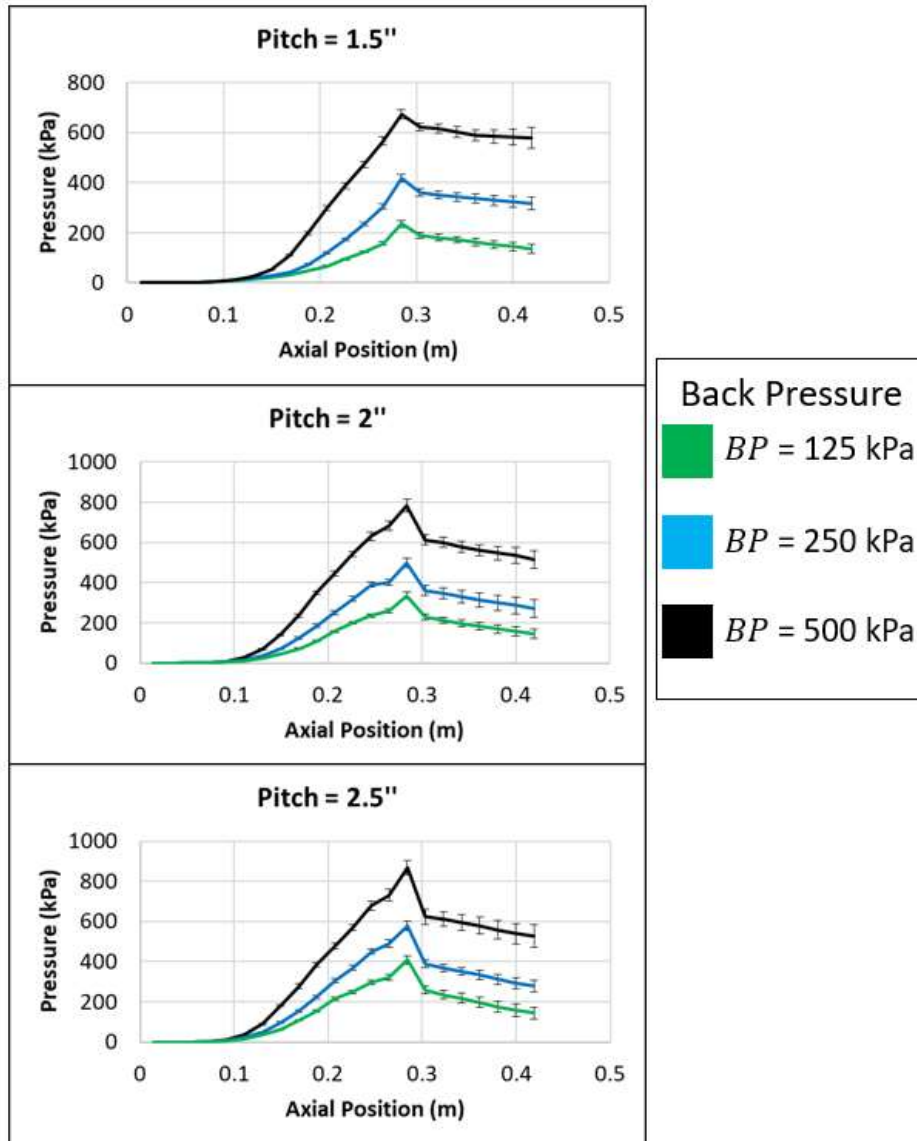


Figure 4.21: Screw pressure vs. Position,  $\mu_{pp} = 0.5$ . The peak pressure is seen to scale with the backpressure within each screw pitch. Near the end of the screw flights there is some non-uniform growth, but within each screw pitch, the behavior is consistent.

For a particle-particle friction coefficient of 0.25, Figure 4.22 and Figure 4.23 show how the peak pressure (found at the end of the screw flights) and total screw torque for the system change with respect to screw pitch and backpressure. The total screw torque increases linearly with an increase in backpressure and screw pitch, but the peak pressure is not perfectly linear. In order to understand their relationship better, a wider range of inputs and the inclusion of other geometric and material properties is necessary; however, it remains that there is a strong correlation between pressure and torque in compression screw feeders.

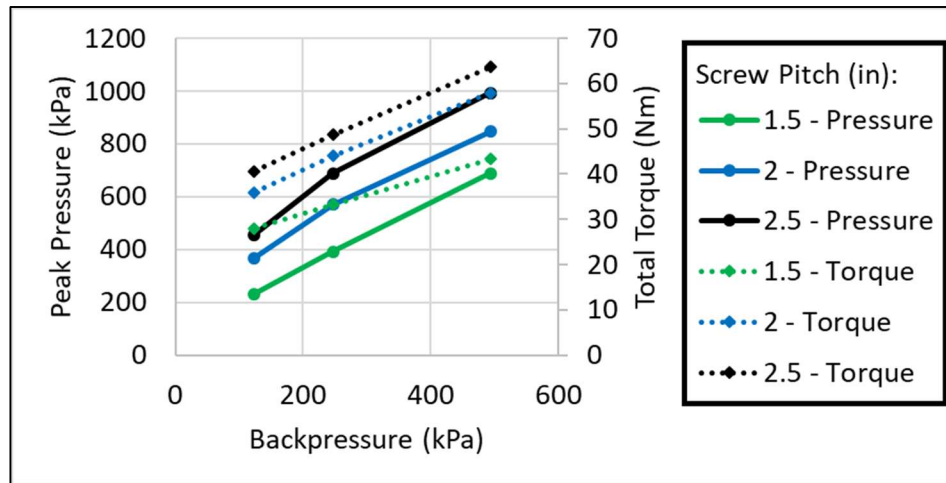


Figure 4.22: Peak pressure and torque, sensitivity to pitch,  $\mu_{pp} = 0.25$ . Peak pressure and total screw torque show similar, linear sensitivities to screw pitch and backpressure suggesting a strong correlation. More backpressures and screw pitches are needed to investigate the relationship further.

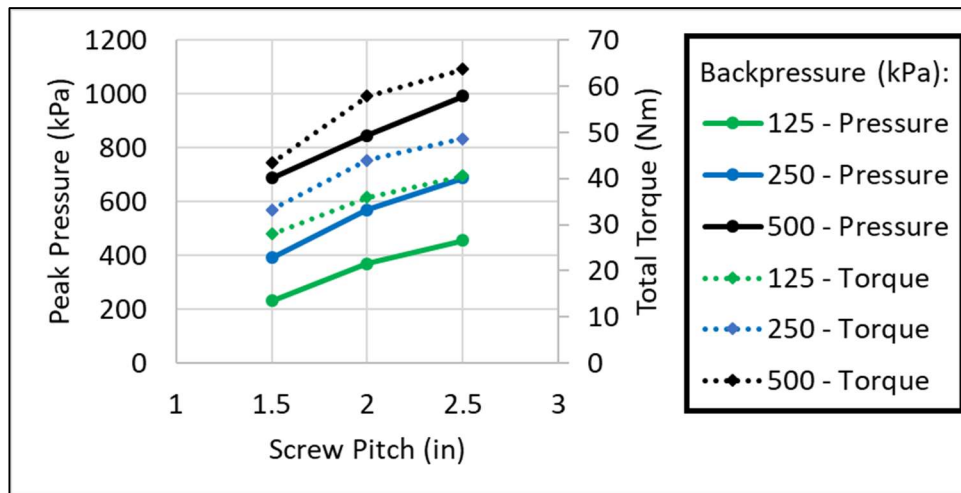


Figure 4.23: Peak pressure and torque, sensitivity to backpressure,  $\mu_{pp} = 0.25$ . In contrast to Figure 4.22, this plot shows screw pitch on the x-axis instead of backpressure.

Although the total screw shows a strong correlation between pressure and torque, it does not explain which locations in the screw require the most torque to drive. To address this issue, Figure 4.24 shows the differential torque required to drive a differential axial segment of the screw ( $\frac{dT}{dz}$ ), and is presented for each pitch and backpressure and a particle-particle friction coefficient of 0.5. The total torque for each simulation can be calculated by integrating the area under the plot, and the value at any axial location can be interpreted as the intensity of torque at that location.

Figure 4.25 and Figure 4.26 show how  $\frac{dT}{dz}$ , pressure, screw case radius, and shaft radius change with axial position for the screw section. Upon investigation, no simple, useful correlations exist between these values, and an explanation for the shape is not apparent. However, it can be observed that moving axially toward the exit,  $\frac{dT}{dz}$  does increase with pressure until the outer case radius and inner screw radius start to converge. This change in geometry causes the effective surface area of the leading flight to decrease, and results in a reduction of the moment arm at which the screw face pressure is acts. Lastly, Figure 4.24 shows that the torque contribution of the plug section shows a low sensitivity to backpressure and is nearly constant throughout the length even though the pressure is decreasing. This behavior is not understood but may be due to anisotropy or variations in the stresses near the boundaries that is not reflected in the pressure.

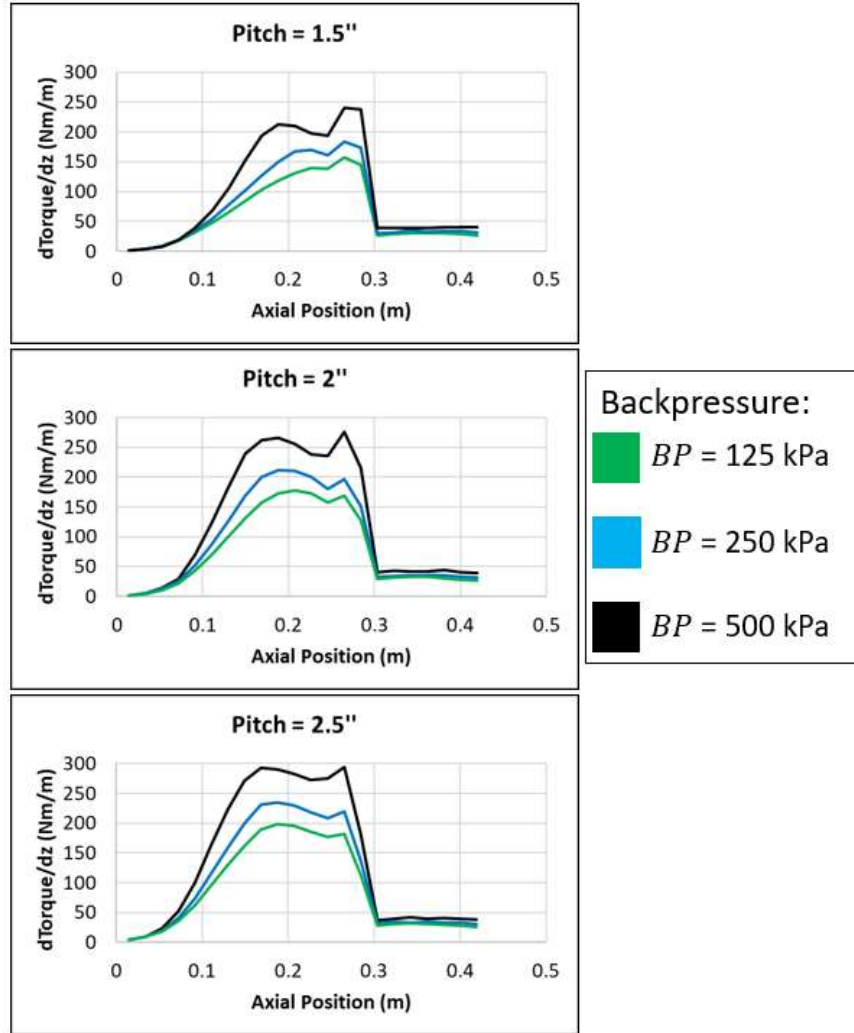


Figure 4.24:  $\frac{dT}{dz}$  versus axial position,  $\mu_{pp} = 0.5$ .  $\frac{dT}{dz}$  at each location scales with backpressure, but a form for the screw section is unclear. The development of  $\frac{dT}{dz}$  in the screw section is not monotonic.

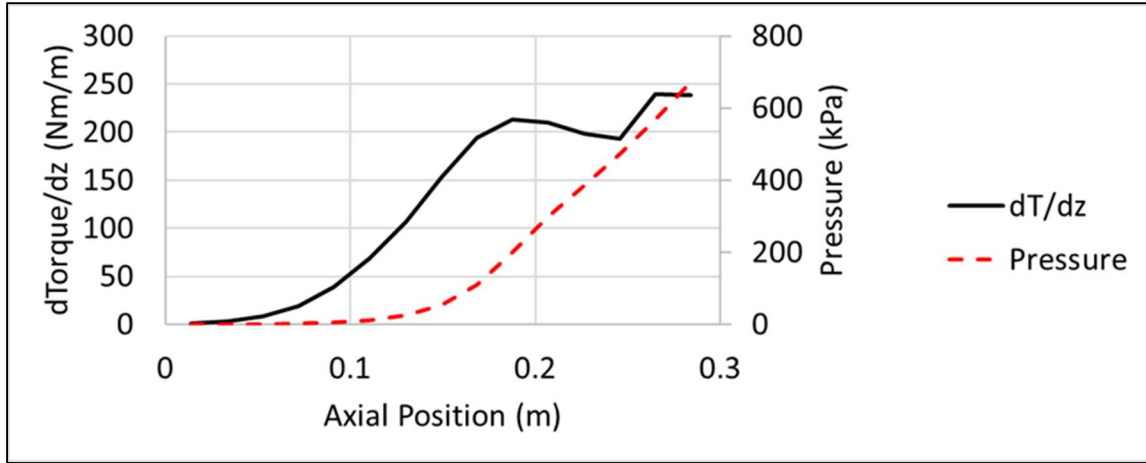


Figure 4.25:  $\frac{dT}{dz}$  and pressure versus axial position where pitch = 1.5", backpressure = 500 kPa,  $\mu_{pp} = 0.25$ . The figure shows that  $\frac{dT}{dz}$  is not proportional to the measured pressure.

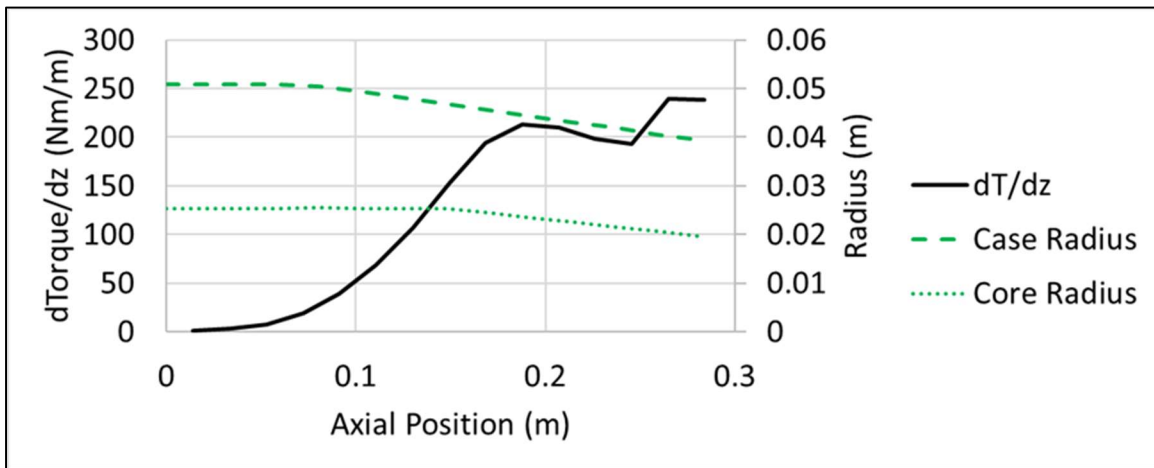


Figure 4.26:  $dT/dz$  and screw radii versus axial position where pitch = 1.5", backpressure = 500 kPa,  $\mu_{pp} = 0.25$ .  $\frac{dT}{dz}$  is affected by the case and core radius of the screw in addition to the solid pressure, but the form is unclear.

Figure 4.27 shows the rotational power required to drive the three main screw flight faces: the leading edge, the screw core, and the trailing edge. The rotational power is defined as the amount of energy dissipated in the direction of rotation of that body. A body with a positive rotational power requires input energy to cause the motion, dissipating energy and increasing operational torque in the case of the screw feeder. A surface with a negative power, though, is adding energy to the system, making the screw easier to rotate. Figure 4.27 shows that the leading screw flight dominates the power dissipated in the simulations and requires the most torque to

drive, trailed significantly by the screw shaft in each case. However, the trailing edge has a negative power dissipation, which is not predicted by any of the previous works. According to Metcalf (1965) and Tadmor et al. (1970), material is slipping against all screw surfaces and therefore each surface should dissipate energy. However, the magnitude and directions of the forces are geometrically complex and difficult to visualize. One possible explanation for this behavior is found by considering the torque on the screw caused by the normal forces acting on the screw faces. Figure 4.28 shows how the normal force acting on the leading face resists the boundary motion, while the normal force acting on the trailing face has a component in the direction of the boundary velocity, aiding boundary motion. This phenomenon is not well understood, and a deeper analysis of the velocity fields and stresses near the boundaries is required to uncover why the trailing edge behaves this way.

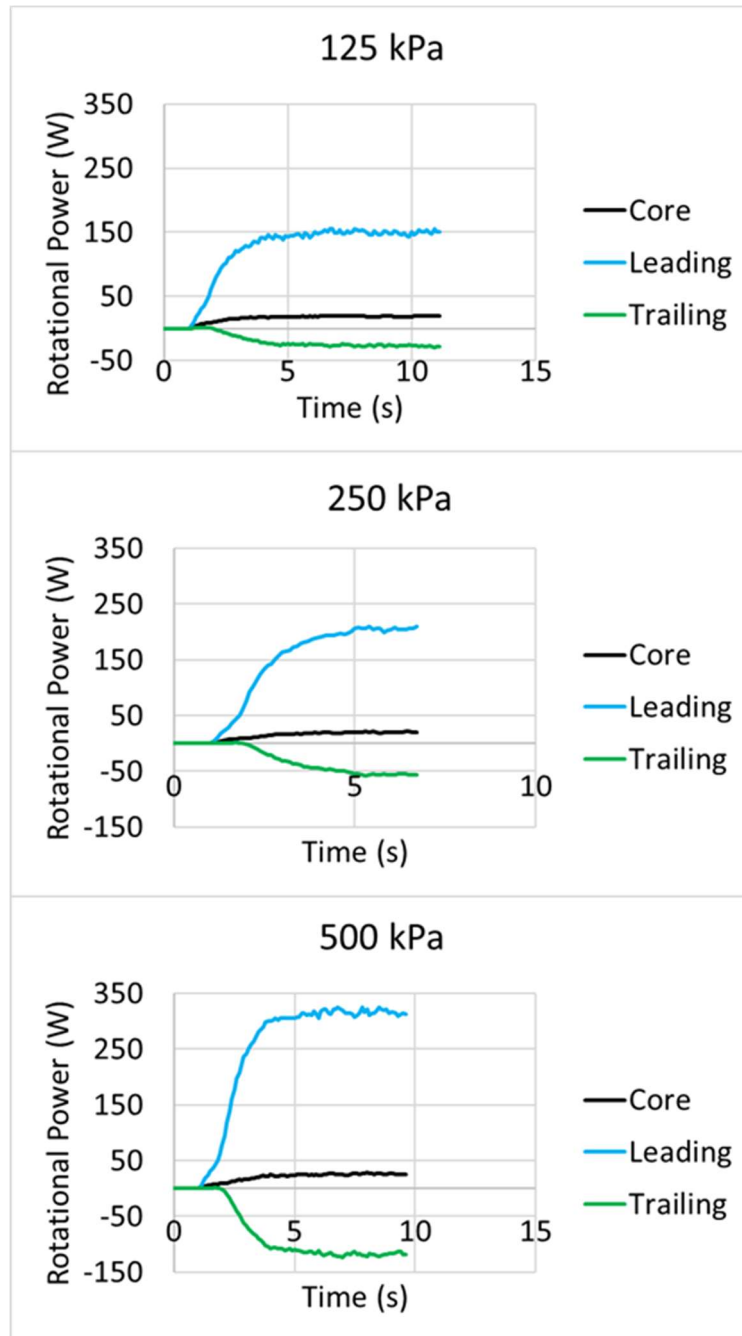


Figure 4.27: Rotational power dissipation by screw face, pitch = 2",  $\mu_{pp} = 0.5$ . In all cases, the leading flight dissipates the most energy, followed by the screw core almost an order of magnitude lower. The trailing flight generates energy in the system, but this behavior is not well understood.

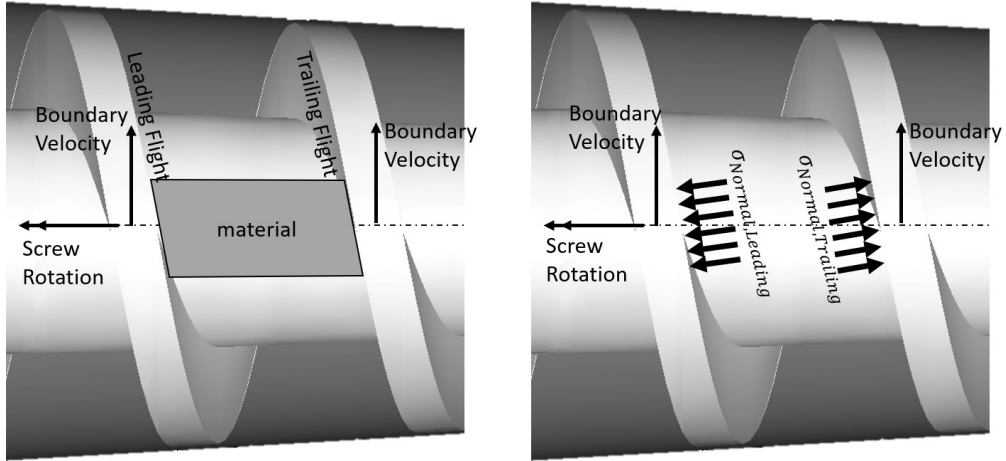


Figure 4.28: Stress direction compared with boundary velocity. This diagram shows that at the leading flight, a component of the normal stress is directed in the opposite direction of the boundary velocity, dissipating energy. However, the trailing flight has a component of the normal stress in the direction of the boundary velocity.

### 4.3 Plug Simulations

The plug section shown in Figure 4.2 is unique to compression screw feeders, and screw simulations suggest that this section plays a significant role in defining the maximum stress found in the screw assembly. Additionally, due to the correlation between maximum stress and total screw torque, the plug section significantly affects the screw torque. To better understand the plug sections as well as to test the assumptions of the compressed bed models described in Chapter 3, two types of plug section simulations were developed: straight (Figure 4.29) and tapered (Figure 4.30). The simulation setup and boundary conditions are now discussed.

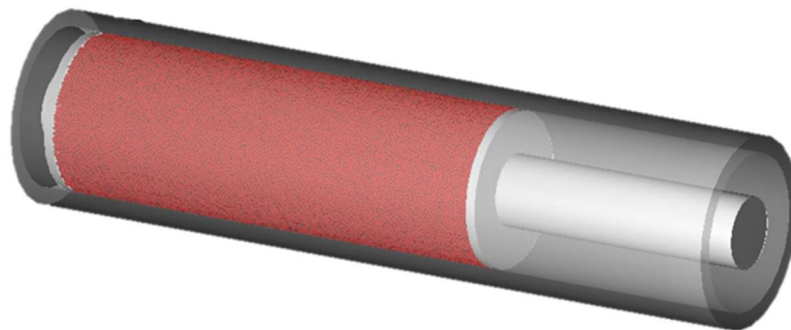


Figure 4.29: Straight plug section simulation showing the annular particle bed being compressed.

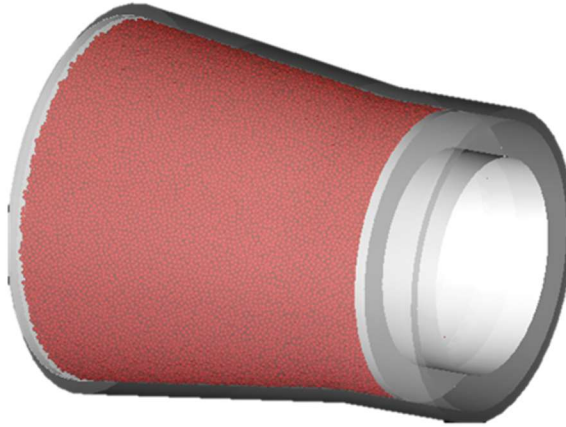


Figure 4.30: Tapering plug section simulation showing the arrangement of particles as they are being compressed.

### 4.3.1 Geometry, Setup, and Inputs

Standalone plug simulations were developed to mimic the loading state and boundary conditions that material in the plug section of the screw feeder experiences at steady-state operation. In the screw simulations, the plug section is subject to a high pressure at one end created by the end of the screw flights, and a low pressure at the other end created by the backpressure. In the plug simulations, a bed of particles is confined between an outer case and a stationary inner shaft while a frictionless annular ring at each end rests against the material. The annulus at one end of particle bed (the left side as shown in Figure 4.29 and Figure 4.30) is subject to an incrementally increasing axial force, representing the maximum pressure generated by the end of the screw flight section. At the other end, the annulus is given a threshold value of stress that resists particle flow until the threshold stress is overcome, representing the backpressure. Once the particle bed begins to move, signaling that the threshold stress has been reached, wall friction on the material is fully mobilized and points toward the high-stress side of the system, similar to what is seen in the screw feeder. The incremental loading process can be visualized in Figure 4.31. Figure 4.32 shows all dimensions in the plug section simulation, and Figure 4.33 and Figure 4.34 show the mesh shape (using the mesh properties shown in Table 4.1. Table 4.3 shows the input properties used in these simulations.

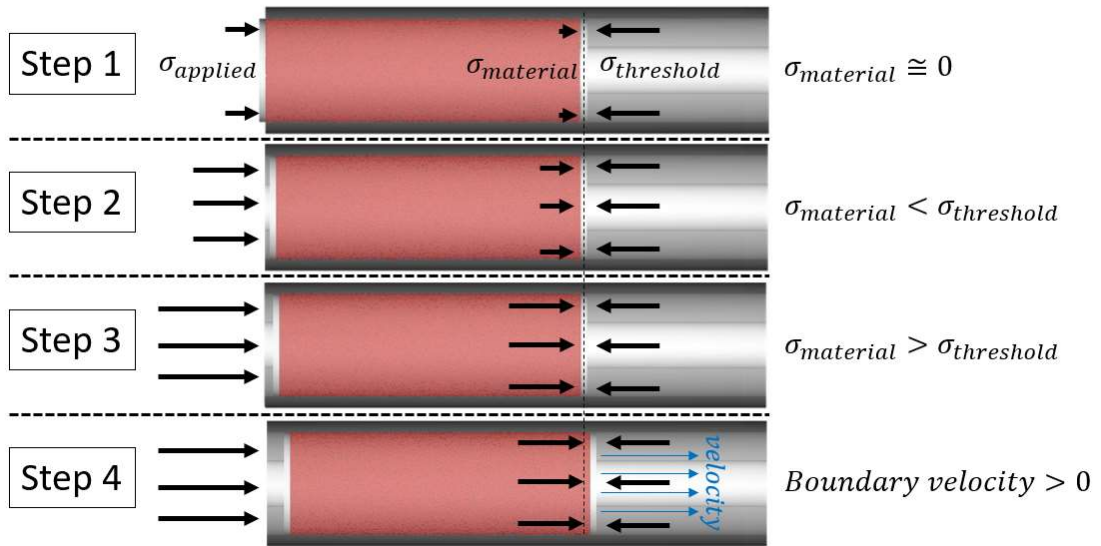


Figure 4.31: Plug simulation procedure for mobilizing friction. The applied stress is increased until the threshold stress is reached on the other end of the annulus and the bed starts sliding. After the bed begins to slide, and the direction of friction is known the pressure profile is measured

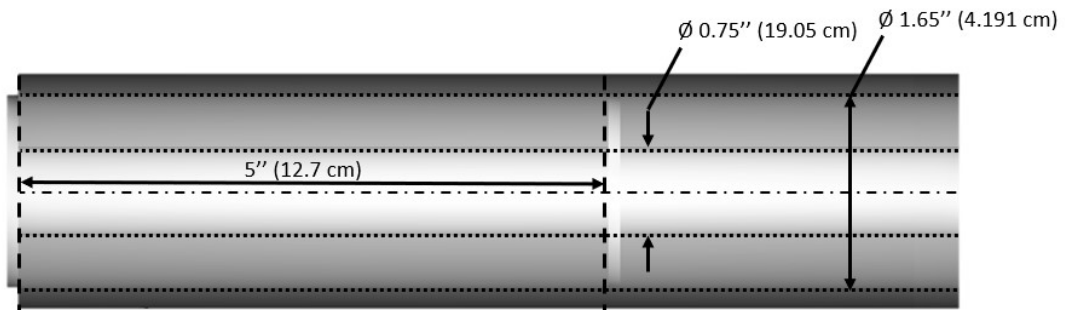


Figure 4.32: Straight plug section dimensions. The initial plug length is 5", but after compaction the axial length changes.

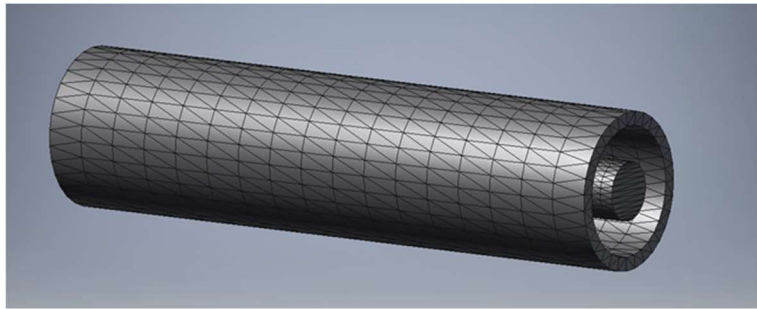


Figure 4.33: Straight plug section case mesh. This mesh was chosen due to the regularity of the mesh size and shape. Because particle bins are used to measure stresses instead of boundary forces, it is not necessary to use a fine mesh.

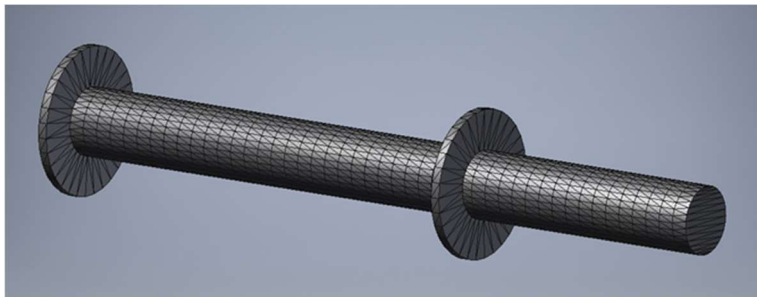


Figure 4.34: Straight plug section shaft mesh. Like Figure 4.33, this figure shows the regular mesh size and shape of the straight plug simulations.

Table 4.3: Straight plug simulation input properties. The properties shown were arbitrarily selected and resemble those used in the screw feeder simulations.

Input Parameter	Notation	Value
Threshold Pressure	$\sigma_{zz,outlet}$	100 [kPa]
Boundary Young's modulus	$E_{boundary}$	10 [GPa]
Boundary Poisson's ratio	$\nu_{boundary}$	.3
Particle bulk Young's modulus	$E_{particle}$	20 [MPa]
Particle Poisson's ratio	$\nu_{particle}$	.3
Particle density	$\rho_{particle}$	500 [ $\frac{kg}{m^3}$ ]
Particle-particle static friction	$\mu_{pp,static}$	0.7
Particle-particle dynamic friction	$\mu_{pp,dynamic}$	0.7
Particle-particle coefficient of restitution	$\epsilon_{pp}$	0.3
Particle-boundary static friction	$\mu_{pb,static}$	0.3
Particle-boundary dynamic friction	$\mu_{pb,dynamic}$	0.3
Particle-boundary coefficient of restitution	$\epsilon_{pb}$	0.3
Particle size range	d	1.05 – 0.95 [mm]
Particle distribution type	-	Uniform
Timestep	$\Delta t$	1e-6 s

In the converging plug section, the boundary conditions are the same as the straight plug section, but the outer case converges over the length. This geometry is more representative of the entrance of the plug section in the screw feeder, as there is a convergence in the outer case after the screw flights end. Figure 4.35 shows the dimensions of this section, and Figure 4.36 and Figure 4.37 show the mesh shape used. Table 4.4 summarizes the input properties used in the converging plug simulations.

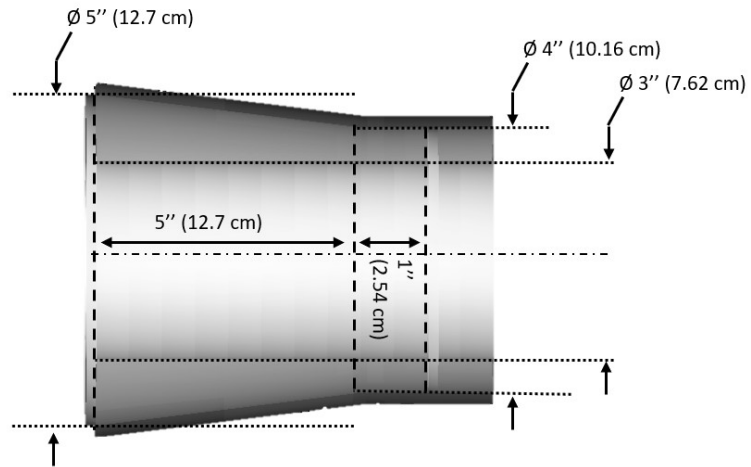


Figure 4.35: Tapering plug section dimensions. The tapering plug section simulations include one end with a tapering section where the stress is incrementally increased. On the other end, after a small straight section, a threshold pressure is applied.

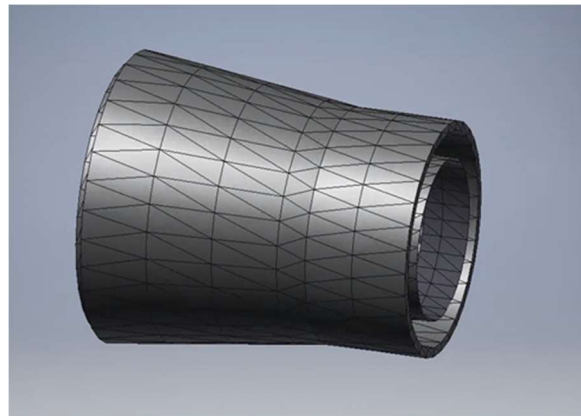


Figure 4.36: Tapering plug section case mesh. This mesh was generated with the same mesh properties as the screw feeder and the straight plug section

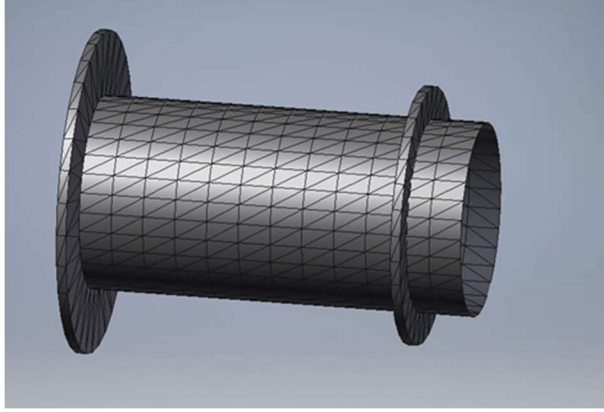


Figure 4.37: Tapering plug section shaft mesh.

Table 4.4: Converging plug simulation input properties. Like the straight plug simulation input properties, these are arbitrary chosen to be similar to those used in the screw simulations.

Input Parameter	Notation	Value
Threshold Pressure	$\sigma_{zz,outlet}$	30 [kPa]
Boundary Young's modulus	$E_{boundary}$	10 [GPa]
Boundary Poisson's ratio	$\nu_{boundary}$	.3
Particle bulk Young's modulus	$E_{particle}$	20 [MPa]
Particle Poisson's ratio	$\nu_{particle}$	.3
Particle density	$\rho_{particle}$	500 [ $\frac{kg}{m^3}$ ]
Particle-particle static friction	$\mu_{pp,static}$	0.7
Particle-particle dynamic friction	$\mu_{pp,dynamic}$	0.7
Particle-particle coefficient of restitution	$\epsilon_{pp}$	0.3
Particle-boundary static friction	$\mu_{pb,static}$	0.3
Particle-boundary dynamic friction	$\mu_{pb,dynamic}$	0.3
Particle-boundary coefficient of restitution	$\epsilon_{pb}$	0.3
Particle size range	d	1.7 – 1.8 [mm]
Particle distribution type	-	Uniform
Timestep	$\Delta t$	1e-6 s

The pressure was measured in these simulations using axisymmetric, annular, Eulerian particle bins like those used in the plug section of the screw feeder. Within these bins, a standard algorithm was used that sums the forces acting on the particles that intersect the bin boundaries and combines these values with the bin boundary areas to develop an average, full stress tensor. This technique was especially important because although the system should be axisymmetric, the

particle generation algorithm used to fill the simulation before the first timestep generated a slightly inhomogeneous packing. The inhomogeneity is located near the seed point of the particle generation algorithm and is the result of a decrease in the packing efficiency as more particles are added to the system. This effect results in a denser packing near the seed point, which results in higher stresses near that point as well.

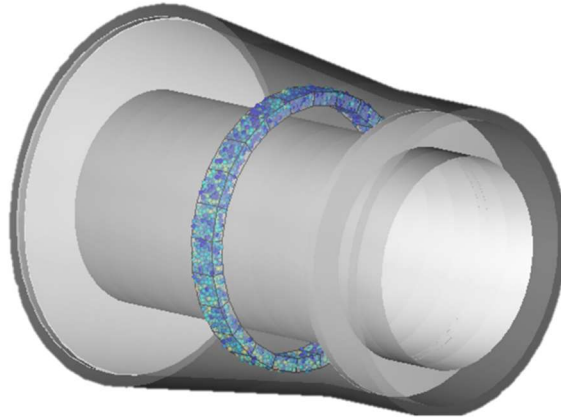


Figure 4.38: Annular Eulerian particle bin. The bin shown is positioned between the tapering outer case and the constant inner case.

### 4.3.2 Results

Firstly, the evolution of solid stresses for the straight plug section shown in Figure 4.39 is plotted in Figure 4.40. In all straight plug simulations, a monotonic growth in all stress components occurs from the low stress to the high-stress side. Also apparent in Figure 4.41, the ratio of the minor stresses to the principal stress remains almost constant over the length. However, the minor stresses are almost an order of magnitude lower than the principal stress, suggesting the material is not in a hydrostatic pressure state as the screw simulations demonstrated. Figure 4.40 also shows a small anomaly at the high-pressure side of the plug (the simulated plug entrance). One explanation for the unexpected change in stresses is a complication that arises from measuring pressures with the particle binning method. As the particle bins are moved close to a boundary the particle packing effects caused by the chosen size distribution and particle shape start to affect the measured pressures.

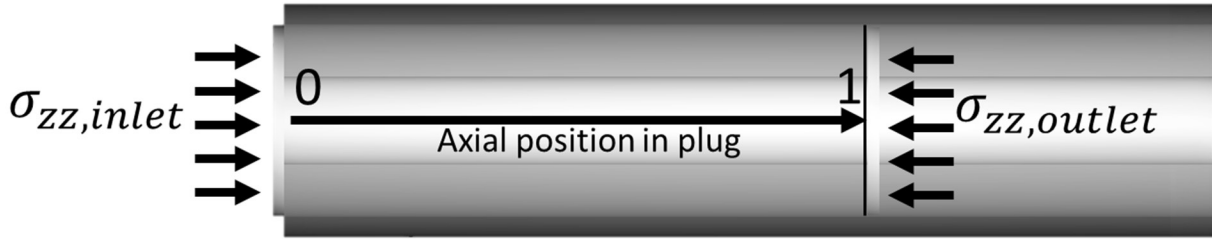


Figure 4.39: Direction of stresses and coordinate system. A high stress is applied at the inlet, and a low stress is applied at the outlet.

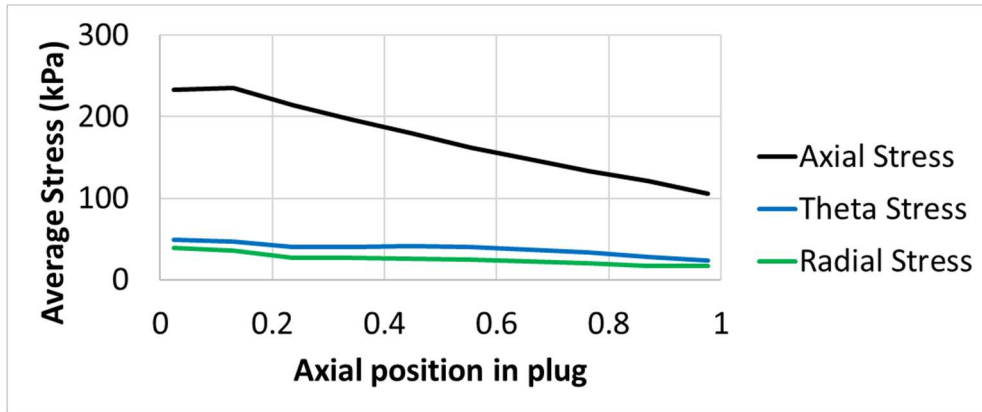


Figure 4.40: Average stresses over the length of the straight plug simulations. Except for some boundary effects at the high-pressure side, the growth from low to high pressure is consistent. The axial stress is much larger than the radial and theta stresses and the material is not in a hydrostatic stress state like that found in the screw feeder simulations.

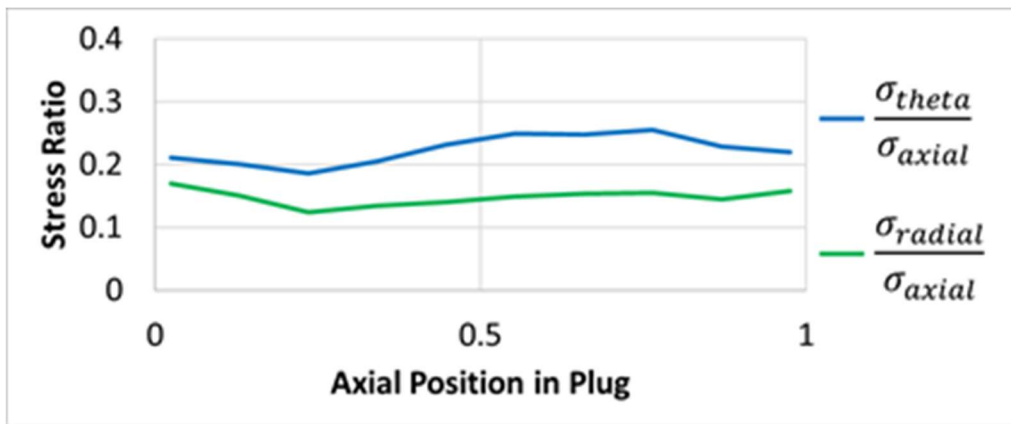


Figure 4.41: The ratio of average principal stresses over the length of the straight plug. These values remain largely constant over a wide range of stresses.

The difference between the nearly hydrostatically loaded plug section found in the screw simulations and the anisotropic plug section in the standalone simulations is not fully understood. One possible explanation for this discrepancy is the difference between the boundary conditions

of the plug section in each case. The standalone plug section simulations receive a uniform axial stress over the entire annulus while the plug section in the screw simulations does not. Figure 4.42 and Figure 4.43 illustrate this difference, where brightly colored particles are under higher loads. Additionally, the entrance to the plug section in the screw simulation is subject to considerable shear stress while the standalone simulation is not. The discrepancy between the plug section in the standalone simulations and the screw simulations is not the focus of this work, and assumption of a hydrostatic stress state is used in the analytical modeling approach.

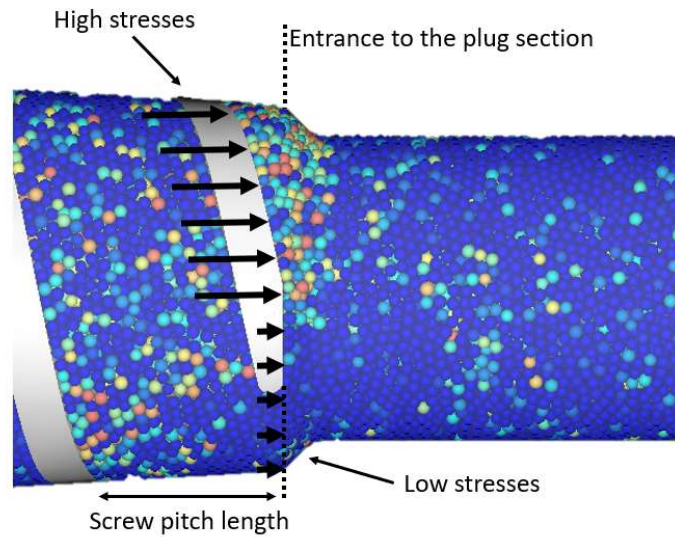


Figure 4.42: Screw feeder plug section, high-pressure entrance. The transition region from the screw flights into the plug section is complicated and subject to significant normal and shear stresses from the leading screw flight.

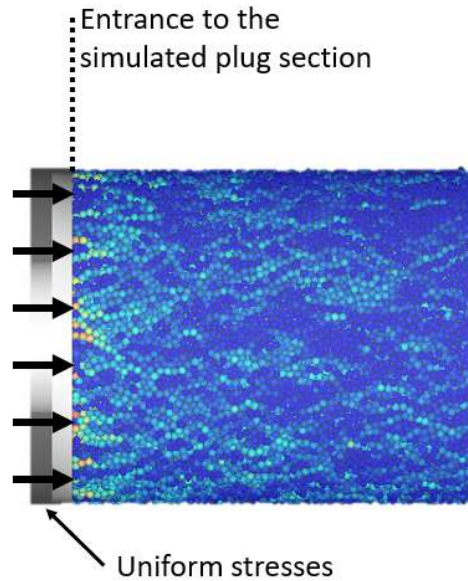


Figure 4.43: Standalone plug section, high-pressure boundary condition. Unlike the entrance to the plug region in the screw feeder simulations, the plug simulations experience a uniform axial loading.

Figure 4.44 illustrates the converging plug section, and Figure 4.45 and Figure 4.46 show the solid stresses and the ratio of the stresses over the length, respectively. The stresses shown in Figure 4.45 exhibit fluctuations in the middle of the section and nonuniformities towards the inlet and outlet. With smaller particles and more time averaging the trends are expected to show monotonic growth in all stresses from outlet to inlet. As with the straight plug simulations, the axial stress is still the principal stress but the radial and theta stresses are much closer. This behavior is believed to be caused by the radial compression experienced by particles passing through the tapering outer case, which also explains why the radial stress is larger than the theta stress. The stress state is not close to being hydrostatic and does not mimic the state of stress seen in the screw simulations. Also, the material is in an active stress state in both the converging and straight plug section ( $\sigma_{zz} > \sigma_{rr}$ ).

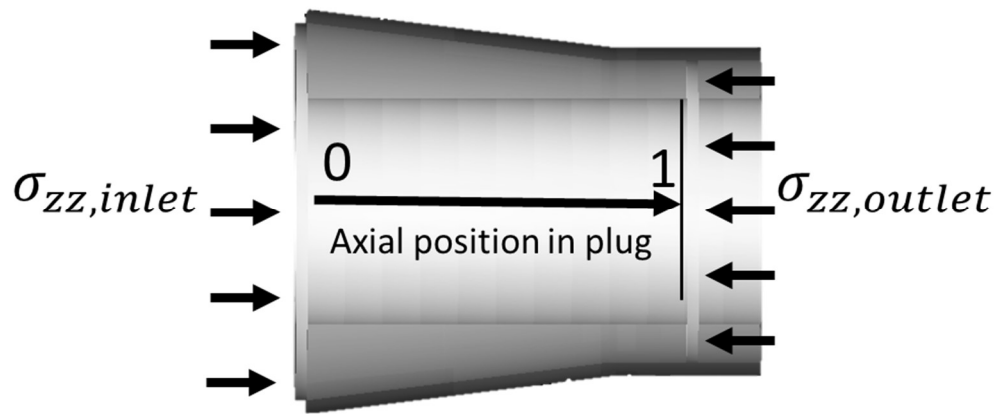


Figure 4.44: Direction of stresses and coordinate system for the converging plug simulations. The straight section begins at a dimensionless axial position of  $\sim 0.8$ .

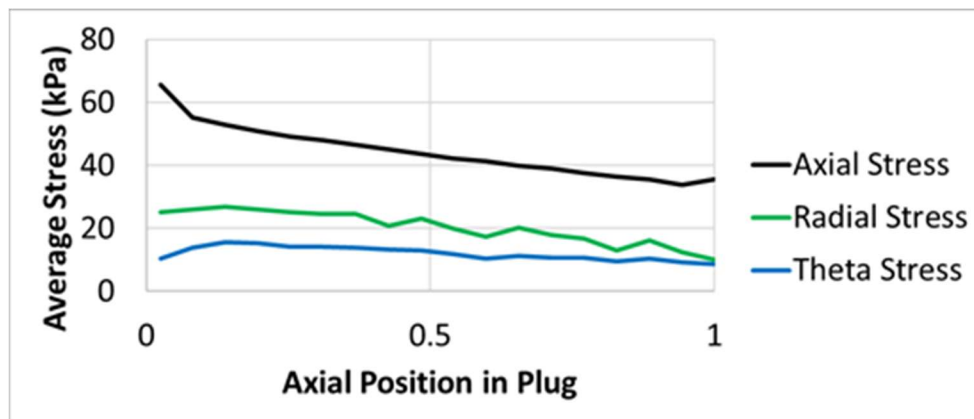


Figure 4.45: Average stresses over the length of the converging plug. Like the straight plug, the converging plug shows that the axial stress is much larger than the radial and theta stresses. However, due to the convergence causing a radial compression, the ratio of axial to radial stress is larger than in the straight plug simulations. Some oscillations and perturbations near the boundaries can be seen, but they are a result of the stress measurement and experimental setup.



Figure 4.46: The ratio of the average principal stresses over the length of the converging plug. Although there are oscillations in the curves, the ratios of the principal stresses remain relatively constant.

#### 4.4 Summary of DEM Conclusions

Simulations were run to compare the behavior of material within a compression screw feeder and a standalone simulation of the plug section within a compression screw feeder. In addition to later providing a set of data, the simulations provided insight into the different sections of the screw feeder. The screw simulations provide information about the stress state of the material passing through the screw channels; the pressure of that material; how the pressure is sensitive to internal friction angle, screw pitch, and backpressure; the torque generated over the length; how torque is sensitive to internal friction angle, screw pitch, and backpressure; and which screw surfaces generate torque. The plug simulations shed light on the stress state of columns of material under axial compression and provide a comparison between converging plug sections and straight plug sections. The major results for the compression screw feeder system studied in this work are:

1. The maximum pressure reached in the screw assembly is higher than the applied backpressure.
2. The backpressure is a critical parameter, but the geometry and material properties also significantly affect the peak pressure achieved.
3. The pressure evolution in the system seems to propagate upstream from the exit and is not fully prescribed by upstream conditions such as inlet pressure, screw geometry, and material properties as some previous literature suggests.
4. The material in the plug section is in an active stress state.

5. The stress state of the material in the screw region, which contributes most of the torque to the system, can be approximated as hydrostatic.

## 5. ANALYTICAL MODELS

Figure 5.1 shows the initially hypothesized pressure profile in the compression screw feeder, showing a monotonic growth to the outlet pressure. However, one of the first observations made in the DEM simulations is that the peak pressure in the system is higher than the outlet pressure and occurs at the end of the screw flights. This result reveals the two distinct sections before and after the peak pressure, and analytical techniques will now be applied to predict this behavior.

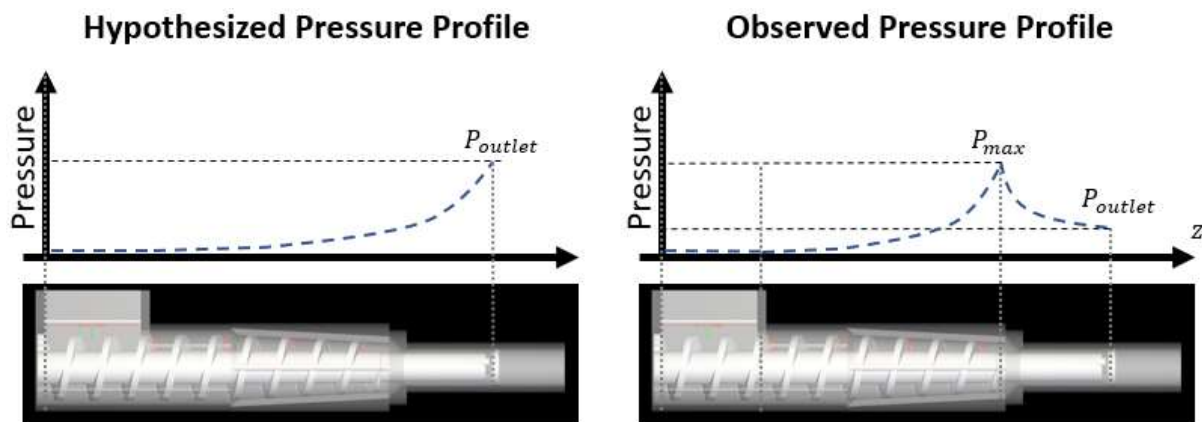


Figure 5.1: Hypothesized versus observed pressure profile. The DEM results show that the peak stress in the system is not the outlet stress, as was previously hypothesized. Rather, the screw section and plug section exhibit significantly different behavior and must be treated individually.

The first region of interest, the screw section, is defined as the region where screw flights directly interact with the material by exerting normal forces and shear forces. This is the region where predictions have been made for the solid stress along the axial path (Broyer & Tadmor, 1972; Campbell & Dontula, 1995; Hyun & Spalding, 1997), but the predictions were based on the assumption that the upstream conditions prescribed the downstream stress profile and the solid stress should be independent of backpressure. Once the material passes the end of the screw flights, it transitions into the plug section of the screw. This section resembles that studied by Janssen (1895), Walker (1966), Walters (1974), Bridgwater et al. (1979), and Nedderman (1992). Chapter 6 is devoted to developing one pair of models that predict the pressure within each section, and a different pair of models that converts the predicted pressure into the steady-state torque required

to drive each of the two sections. Figure 5.2 shows these sections, and Figure 5.3 shows the general shape of the plug section.

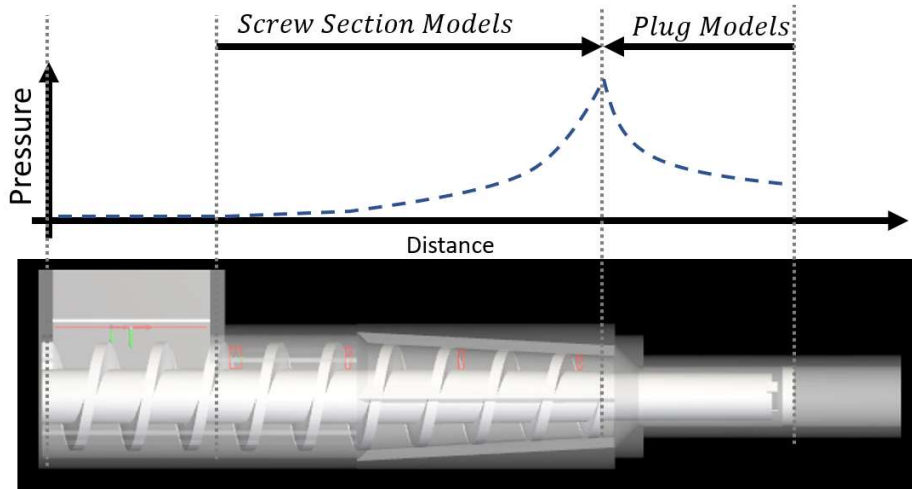


Figure 5.2: Screw section model versus plug section model. The two different regions of DEM behavior are highlighted and the validity of the models is defined.

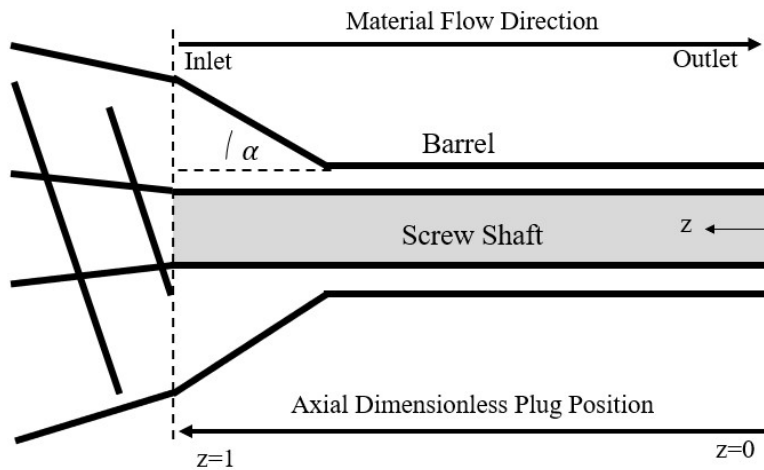


Figure 5.3: Plug section of the compression screw feeder. This figure shows the general shape of the feeder after the screw flights end, and define the direction of the coordinate system.

## 5.1 Methodology

In addition to presenting models that describe the behavior of material within the different screw sections, another goal of this chapter is to propose a complete procedure for approximating the torque required to run a compression screw feeder. Currently, this procedure does not exist,

and the systematic technique presented in the current work provides a first step toward that goal. Once the technique for torque calculation has been outlined, each model is independently developed, allowing for substitution and improvement on each component separately. The assumptions of the models are influenced by the DEM simulation results.

The DEM simulations show that the influence of the outlet pressure propagates backward through the system and affects upstream conditions. Therefore, the first step in the model begins at the feeder outlet, where the pressure is known. The mechanics of the plug section are detailed, and a mathematical model are developed, moving in the upstream direction, to calculate the pressure profile in this section. Next, a screw section model is developed that uses the peak pressure of the system, calculated from the plug model, as an input. Once the entire pressure curve has been approximated, a model is developed for each section that converts the pressure to a torque. In addition to providing a rapid approximation of torque values, the form of the torque equations provides information about the sensitivity of the torque to different input parameters without the need for additional simulations. Figure 5.4 shows the proposed methodology.

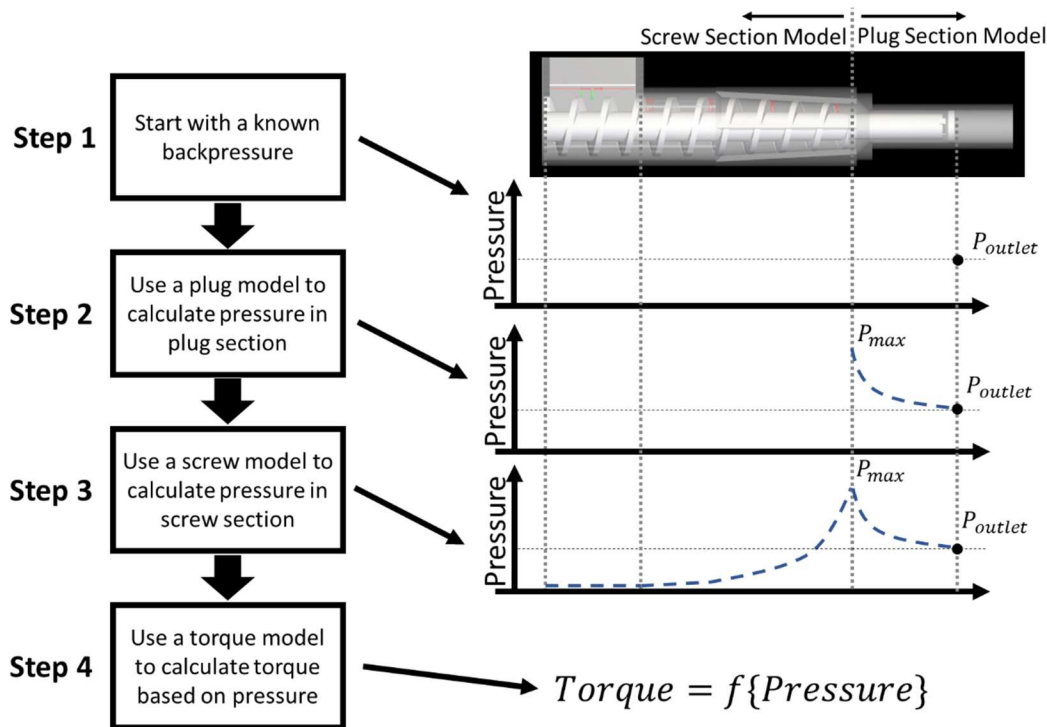


Figure 5.4: Torque model procedure. The most important part of the procedure is starting at the material outlet. By developing a model that begins with the backpressure, that boundary condition can be accounted for in the screw section model. Using the plug pressure as a boundary condition, a screw section pressure model, and then a model to convert from pressure to torque are presented.

## 5.2 Pressure Models

### 5.2.1 Plug Section Model

Beginning at the outlet, a mathematical model can be developed to describe the evolution of solid stress in the plug section. As seen in the previously discussed DEM simulations, there are two general geometries found in the plug section of screw feeders: those with a constant inner and outer radius, and those with a converging outer case. For both of these sections, the approach taken by (Janssen, 1895; McNab & Bridgwater, 1979; Walker, 1966; Walters, 1973a; Walters & Nedderman, 1973) is used, but most closely follows the derivation performed by Nedderman (1992). A small cylindrical or annular differential element is used to perform an axial force balance, and the resulting differential equation is solved. The assumptions used here are the same as described in Section 2.2, but the principal stress direction is not assumed. The derivation starts with the shape of the differential element in Figure 5.5.

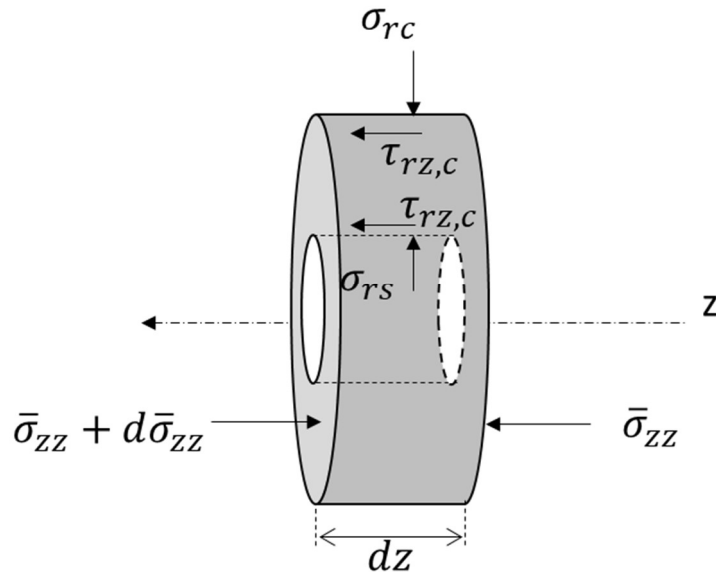


Figure 5.5: Constant geometry plug section differential element. The inner face of the annulus is touching a stationary inner shaft and sliding along it axially.

Performing a axial force balance on the element in Figure 5.5, one can find,

$$\frac{d\bar{\sigma}_{zz}}{dz} - \frac{2(\tau_{rz,c}R_c + \tau_{rz,s}R_s)}{R_c^2 - R_s^2} = 0 \quad (17)$$

where  $\bar{\sigma}_{zz}$  is the average axial normal stress over the cross-sectional area. Next, Mohr-Coulomb theory is used to find a relationship between  $\tau_{rz,b}$ ,  $\tau_{rz,s}$ , and  $\bar{\sigma}_{zz}$ . First, define,

$$\sigma_{zc} \equiv \sigma_{zz}(r = R_c, z) \quad (18)$$

$$\sigma_{rc} \equiv \sigma_{rr}(r = R_c, z) \quad (19)$$

$$\sigma_{zs} \equiv \sigma_{zz}(r = R_s, z) \quad (20)$$

$$\sigma_{rs} \equiv \sigma_{rr}(r = R_s, z) \quad (21)$$

In this model, axial normal stress can vary with radius by using two distribution parameters (Walker, 1966). The axial stress at the case and shaft can be related to the average axial stress by the following equations,

$$\mathcal{D}_c \equiv \frac{\sigma_{zc}}{\bar{\sigma}_{zz}} \Rightarrow \sigma_{zc} = \mathcal{D}_c \bar{\sigma}_{zz} \quad (22)$$

$$\mathcal{D}_s \equiv \frac{\sigma_{zs}}{\bar{\sigma}_{zz}} \Rightarrow \sigma_{zs} = \mathcal{D}_s \bar{\sigma}_{zz}. \quad (23)$$

It is assumed that the material is in an active stress state both because the material is being mechanically compressed axially and because the DEM simulations predict an active stress state ( $\sigma_{zc} > \sigma_{rc}$  and  $\sigma_{zs} > \sigma_{rs}$ ). In this case, a Mohr's Circle diagram can express the internal stresses in the material as shown in Figure 5.6. In the figure, principal stresses  $\sigma_1$  and  $\sigma_2$  are not aligned with the walls, the horizontal coordinate at point "R" represents the radial stress at the wall, the horizontal coordinate at point "Z" represents the axial stress in the material at the walls, and the relationship between the radius of the circle and the pressure are expressed on the plot as well.

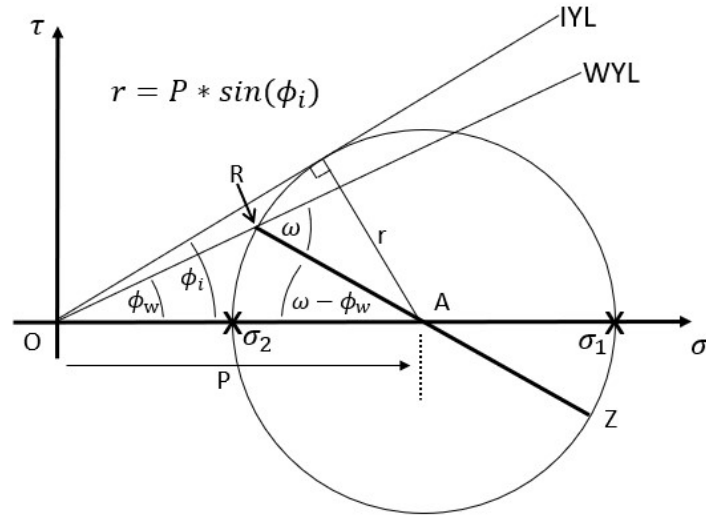


Figure 5.6: Mohr's circle for active failure at an orthogonal wall. This Mohr's circle defines the relationship between shear and normal stresses using trigonometric relationships.

Firstly, the angle  $\omega$  must be determined. By applying the Law of Sines to triangle OAR,

$$\frac{\sin(\phi_w)}{r} = \frac{\sin(180 - \omega)}{P} \quad (24)$$

where,

$$r = \frac{\sigma_1 - \sigma_2}{2} \quad (25)$$

$$P = \frac{\sigma_1 + \sigma_2}{2} \quad (26)$$

Assuming the material is internally failing it is known the radius of the Mohr's circle, "r", can be expressed with the angle of internal friction,  $\phi_i$ ,

$$r = P * \sin(\phi_i) \quad (27)$$

Substituting Eq. (27) into (24) and knowing that  $\sin(\pi - \alpha) = \sin(\alpha)$ ,

$$\omega = \arcsin\left(\frac{\sin(\phi_w)}{\sin(\phi_i)}\right) \quad (28)$$

Now a relationship can be developed between  $\tau_{rz,c}$ ,  $\tau_{rz,s}$ , and  $\bar{\sigma}_{zz}$ . Figure 5.7 shows a simplified Mohr's circle diagram depicting the active failure case,

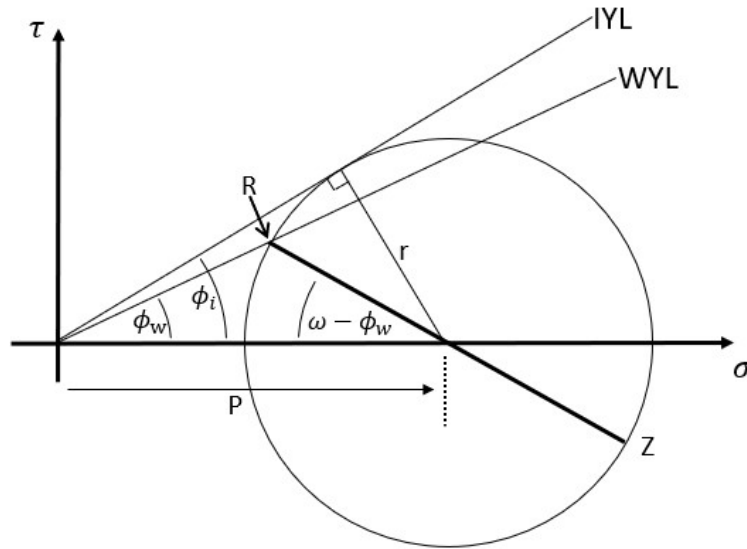


Figure 5.7: Simplified Mohr's circle diagram for the active state of stress, assuming failure along an orthogonal wall.

For the active case, point R represents the pair  $(\sigma_{rr}, \tau_{rz})$  and point Z represents  $(\sigma_{zz}, \tau_{rz})$ . This relationship is true at the case and the screw shaft, where the material is slipping against the wall and, therefore, touching the wall yield locus (WYL). From trigonometry,

$$\sigma_{rr} = p - r \cos(\omega - \phi_w) = P(1 - \sin(\phi_i) \cos(\omega - \phi_w)) \quad (29)$$

$$\sigma_{zz} = p + r \cos(\omega - \phi_w) = P(1 + \sin(\phi_i) \cos(\omega - \phi_w)) \quad (30)$$

$$\tau_{rz} = \sigma_{rr} \tan(\phi_w) \quad (31)$$

These equations can be combined to derive an equation relating  $\tau_{rz}$  at a certain radius, to  $\sigma_{zz}$  at that radius. At an arbitrary radius “A”, taking the ratio of Equations (29) and (30),

$$\sigma_{rr}|_{r=A,z} = \sigma_{zz}|_{r=A,z} \frac{(1 - \sin(\phi_i) \cos(\omega - \phi_w))}{(1 + \sin(\phi_i) \cos(\omega - \phi_w))} \quad (32)$$

From Eqs. (31) and (32), Bridgwater and McNab define a term  $\psi$  that defines the relationship between radial normal and shear stresses at the wall,

$$\psi_w = \frac{(1 - \sin(\phi_i) \cos(\omega - \phi_w))}{(1 + \sin(\phi_i) \cos(\omega - \phi_w))} \tan(\phi_w) \quad (33)$$

Combining Equation (31), (32) and (33),

$$\tau_{rz}|_{r=A} = \sigma_{zz}|_{r=A,z} \psi_w \quad (34)$$

Therefore, combining equations (18)-(23) and (32),

$$\tau_{rz,c} = \bar{\sigma}_{zz} \mathcal{D}_c \psi_c \quad (35)$$

$$\tau_{rz,s} = \bar{\sigma}_{zz} \mathcal{D}_s \psi_s \quad (36)$$

$$\sigma_{rc} = \frac{\bar{\sigma}_{zz} \mathcal{D}_c \psi_c}{\tan(\phi_w)} \quad (37)$$

$$\sigma_{rs} = \frac{\bar{\sigma}_{zz} \mathcal{D}_s \psi_s}{\tan(\phi_w)} \quad (38)$$

Now, substituting (35) and (36) into (17),

$$\frac{d\bar{\sigma}_{zz}}{dz} - \frac{2(\psi_c \mathcal{D}_c \bar{\sigma}_{zz} R_c + \psi_s \mathcal{D}_s \bar{\sigma}_{zz} R_s)}{R_c^2 - R_s^2} = 0 \quad (39)$$

and if  $\psi_c$  and  $\psi_s$  are the same,

$$\frac{d\bar{\sigma}_{zz}}{\bar{\sigma}_{zz}} = \left[ \frac{2\psi_w (\mathcal{D}_c R_c + \mathcal{D}_s R_s)}{R_c^2 - R_s^2} \right] dz \quad (40)$$

Equation (40) is the same as Eq. (11) in the work performed by McNab and Bridgwater, except there is no material weight or fluid force included. Integrating this equation gives,

$$\bar{\sigma}_{zz} = \bar{\sigma}_{zz,0} \int_0^z \left[ \frac{2\psi_w (\mathcal{D}_c R_c + \mathcal{D}_s R_s)}{R_c^2 - R_s^2} \right] dz \quad (41)$$

If the friction angles, distribution factor, and radii do not vary with the axial position, then Equation (41) becomes,

$$\bar{\sigma}_{zz} = \bar{\sigma}_{zz,0} \exp \left[ \frac{2\psi_w (\mathcal{D}_c R_c + \mathcal{D}_s R_s)}{R_c^2 - R_s^2} z \right] \quad (42)$$

Note from Eqs. (22) and (23), if  $\mathcal{D}_c = 1$  and  $\mathcal{D}_s = 1$ , then,

$$\sigma_{zw} = \sigma_{zs} = \bar{\sigma}_{zz}, \quad (43)$$

Although the straight plug section is a useful and common geometry in screw feeders, it is also common in screw systems to have converging plug section geometries. Although Equation 42 could be used to approximate the behavior of converging sections by using averaged radii, the mechanics are fundamentally different. Figure 5.8 shows the differential element used in a converging analysis, which due to the angle  $\alpha$  is considerably more complex. The directions of the shear and normal force at the case are now inclined, and the area changes in the z-direction.

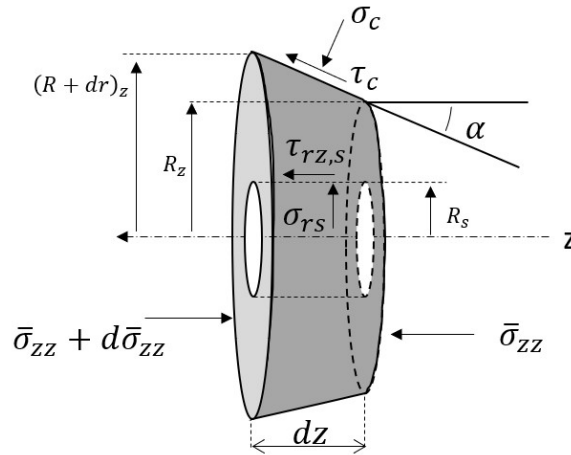


Figure 5.8: Converging plug section differential element. The radius is a function of the axial position causing the resulting surface areas to also be a function of axial position.

The analysis uses the same assumptions as in the straight plug section geometry calculations. Firstly, the outer area has a more complex form, and can be calculated with the equation for the surface area of the inclined surface of a conic frustum (Figure 5.9), given by Equation (44),

$$A_s = \pi(R + r)\sqrt{h^2 + (R - r)^2} \quad (44)$$

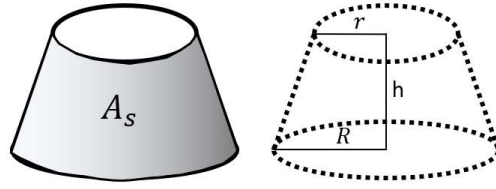


Figure 5.9: Surface area of the inclined edge of a conic frustum.

If the height is taken to be a differential term  $dz$ , the equation can be written as:

$$A_s = \pi[(R_z + dR_z) + R_z]\sqrt{dz^2 + dR_z^2} \quad (45)$$

where from geometry,

$$dR_z = dz \tan \alpha \quad (46)$$

Equation (45) simplifies to,

$$A_s = \frac{2\pi R_z dz}{\cos \alpha} \quad (47)$$

A z-direction force balance can be performed on this differential conic frustum, giving:

$$\begin{aligned} & \bar{\sigma}_{zz}\pi(R_z^2 - R_s^2) \\ & -(\bar{\sigma}_{zz} + d\bar{\sigma}_{zz})\pi((R_z + dR_z)^2 - R_s^2) \\ & +\sigma_c \frac{2\pi R_z dz}{\cos \alpha} \sin(\alpha) \\ & +\tau_c \frac{2\pi R_z dz}{\cos \alpha} \cos(\alpha) \\ & +\tau_{r,z,s} 2\pi R_s dz = 0 \end{aligned} \quad (48)$$

Plugging in Equation (46),

$$\frac{d\bar{\sigma}_{zz}}{dz} = \frac{2(\sigma_c R_z \tan(\alpha) + \tau_c R_z + \tau_{rz,s} R_s - \bar{\sigma}_{zz} R_z \tan(\alpha))}{R_z^2 - R_s^2} \quad (49)$$

Equation (49) simplifies to the McNab and Bridgewater solution for  $\alpha = 0$ :

$$\frac{d\bar{\sigma}_{zz}}{dz} = \frac{2(\sigma_c R_z \tan(0) + \tau_c R_z + \tau_s R_s - \bar{\sigma}_{zz} R_z \tan(0))}{R_z^2 - R_s^2} = \frac{2(\tau_b R_z + \tau_s R_s)}{R_z^2 - R_s^2} \quad (50)$$

Now, a relationship is developed between each of the respective stresses and the average axial stress using the following Mohr's circle. Beyond Equation 50, the solutions for  $\alpha = 0$  and  $\alpha \neq 0$  will differ, as the relationship between all stresses at the case is affected by the angle of inclination. The stresses at the shaft remain unaffected by the angle of incline and adhere to the analysis that leads to equation 42. The following Mohr's circle (Figure 5.10) represents an active stress state where point C represents the pair  $(\sigma_c, \tau_c)$ , point R represents  $(\sigma_{rr}, \tau_{rz})$ , and point Z represents  $(\sigma_{zz}, \tau_{zr})$ ,

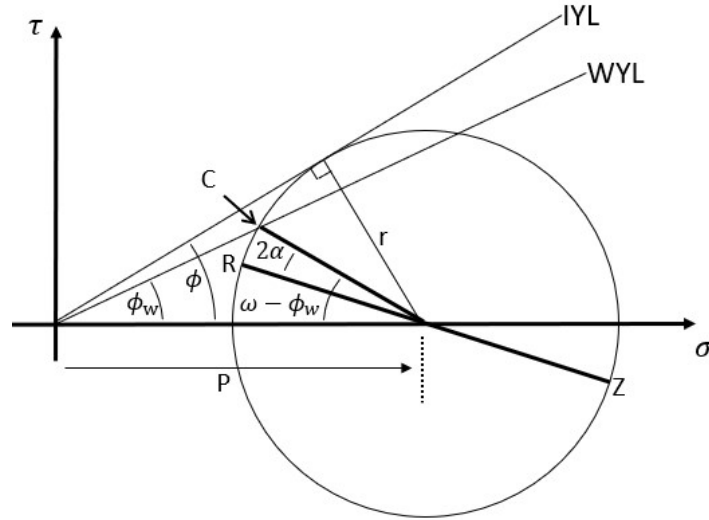


Figure 5.10: Mohr's circle for active failure at an inclined wall. Point C deviates from point R by two times the angle of inclination of the wall to the axis.

Using trigonometry:

$$\sigma_c = P - R \cos(\omega - \phi_w) = P(1 - \sin(\phi_i) \cos(\omega - \phi_w)) \quad (51)$$

$$\tau_b = R \sin(\omega - \phi_w) = P \sin(\phi_i) \sin(\omega - \phi_w) \quad (52)$$

$$\sigma_{rr} = P - R \cos(\omega - \phi_w - 2\alpha) = P(1 - \sin(\phi_i) \cos(\omega - \phi_w - 2\alpha)) \quad (53)$$

$$\sigma_{zz} = P + R \cos(\omega - \phi_w - 2\alpha) = P(1 + \sin(\phi_i) \cos(\omega - \phi_w - 2\alpha)) \quad (54)$$

The ratios of these relationships can be taken to remove their dependence on the pressure P, and each important quantity can be written in terms of  $\sigma_{zz}$ . Again, it is important to note that this  $\sigma_{zz}$  is local and changes with radius and axial position. However, Eqs. (22) and (23) can be used to relate the local axial stress at a specific radius and position to the average axial stress at an axial position. Performing this substitution,

$$\sigma_b = \bar{\sigma}_{zz} \mathcal{D}_b \frac{1 - \sin(\phi_i) \cos(\omega - \phi_w)}{1 + \sin(\phi_i) \cos(\omega - \phi_w - 2\alpha)} = \bar{\sigma}_{zz} \mathcal{D}_b \mathcal{A} \quad (55)$$

$$\tau_b = \bar{\sigma}_{zz} \mathcal{D}_b \frac{\sin(\phi_i) \sin(\omega - \phi_w)}{1 + \sin(\phi_i) \cos(\omega - \phi_w - 2\alpha)} = \bar{\sigma}_{zz} \mathcal{D}_b \mathcal{B} \quad (56)$$

To simplify the notation, the trigonometric terms are substituted with scripted variables  $\mathcal{A}$  and  $\mathcal{B}$  as defined by Eqs. (55) and (56),

$$\mathcal{A} = \frac{1 - \sin(\phi_i) \cos(\omega - \phi_w)}{1 + \sin(\phi_i) \cos(\omega - \phi_w - 2\alpha)} \quad (57)$$

$$\mathcal{B} = \frac{\sin(\phi_i) \sin(\omega - \phi_w)}{1 + \sin(\phi_i) \cos(\omega - \phi_w - 2\alpha)} \quad (58)$$

It is important to note that although Eqs. (55) and (56) are necessary for describing the active stress at the angled wall, Equation (36) is still valid at the inner screw shaft. Substituting these relationships into Equation (49) and simplifying,

$$\frac{d\bar{\sigma}_{zz}}{\bar{\sigma}_{zz}} = \frac{2(D_c \mathcal{A} R_z \tan(\alpha) + D_c \mathcal{B} R_z + D_s \psi_s R_s - R_z * \tan(\alpha))}{R_z^2 - R_s^2} dz \quad (59)$$

The final consideration of this model is motivated by the DEM simulations and specifically demonstrated in Figure 4.17. As discussed in previous chapters, although the Walker model predicts drastically different stresses in each principal direction for a uniformly and axially loaded column, it was observed that the material throughout the screw feeder was in a largely isotropic stress state on average. This state could be due to the nonuniform loading that the plug section receives, where only the tip of the final flight is pressing directly on the plug section. Although this difference is not understood or examined in the current work, the observation allows for a useful simplification in the analytical model. The previously derived plug model is used to calculate the average axial stress,  $\bar{\sigma}_{zz}$ , and this stress is assumed to be equal to the pressure with the following relationship;

$$Pressure = P(z) = \frac{trace(\sigma_{ij})}{3} \Big|_z \cong \bar{\sigma}_{zz}(z) \quad (60)$$

This simplification is also justified in part because it is a conservative, upper-bound estimate of the solid pressure. This relationship is applied in the models by using the solution for the axial stress in the plug section as an approximation to the pressure. The validity of this assumption is somewhat motivated in Figure 4.17, which shows that the material is in a hydrostatic stress state throughout the plug section when average stresses are used.

## 5.2.2 Screw Section Model

As opposed to the mechanistic approach taken to describe the plug section, the proceeding screw section model relies on a more empirical approach. The rationale for this decision is twofold. The previously developed one-dimensional models predict two key aspects of screw feeders: an exponential trend of stresses from the entrance to exit, and an insensitivity to downstream boundary conditions. Firstly, a departure from the predicted exponential trends has already been observed in simulations run by Yu and Arnold (1997) as well as simulations in the current work, suggesting that there are missing pieces to the analysis of the screw section. Secondly, the DEM simulations suggest that contrary to previous literature, it is not upstream boundary conditions and geometry (towards the hopper) that govern downstream behavior (towards the exit of the screw feeder), but rather, a combination of upstream and downstream conditions that prescribe the screw

behavior. Therefore, the current work uses the mechanistic plug section model to predict the peak pressure in the screw, and then assume the form of the pressure evolution in the screw section. The consequence of this simplification is that the accuracy of the screw section pressure model is dependent on the accuracy of the plug section model, and any mispredictions generated at the step of predicting plug pressure will propagate to the screw section.

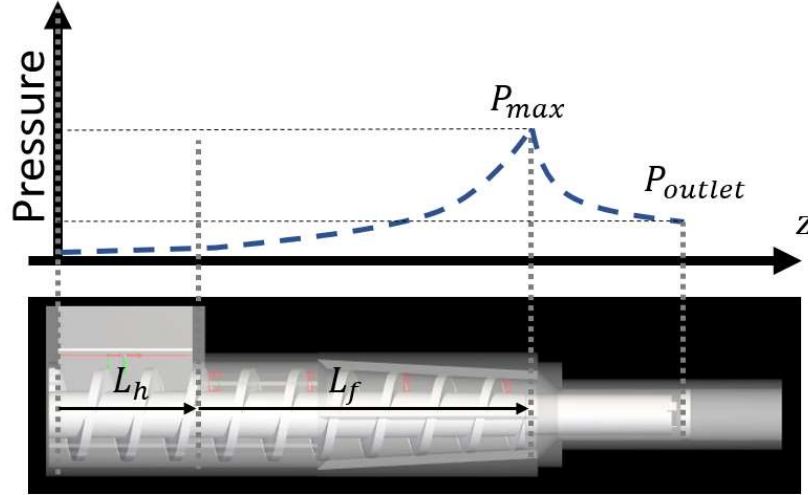


Figure 5.11: Screw feeder pressure profile. The pressure of the material within the hopper (up to the hopper length,  $L_h$ ) is zero, and the pressure grows to the peak pressure over the length of the screw flights,  $L_f$ .

The pressure growth in the screw section, defined as the region between the hopper section and the end of the screw flights ( $L_h$  and  $L_f$ ), is assumed to have the following form,

$$Pressure = P(z) = Az^2 + Bz + C \quad (61)$$

and the boundary conditions are assumed to be,

$$P(0) = 0, P(L_f) = P_{max}, \frac{dP}{dz} \Big|_{z=0} = 0 \quad (62)$$

With the boundary conditions, the pressure curve simplifies to,

$$P(z) = \left( \frac{P_{max}}{L_f^2} \right) z^2 \quad (63)$$

In this work the third boundary condition relating to  $\frac{dP}{dz}$  was arbitrarily chosen to simplify the analysis.

### 5.3 Torque Models

Now that expressions have been derived for the solid pressure throughout the screw, mechanical models can be used to describe the torque required to maintain the steady-state pressure. The general strategy is to consider an axial position in the screw feeder and combine at that point the solid pressure, surface area, average radial position of that surface area, the direction of force at that point, and a friction coefficient to calculate the torque generated by the pressure. Due to geometric differences, separate models must be used to predict the screw torque generated by the plug section and the screw section. These models and their assumptions are discussed in the following paragraphs.

#### 5.3.1 Plug Section Model

Due to the simplicity of the geometry in the plug section, the forces acting on the screw shaft are well defined. In this region, the screw rotates beneath the material as it is slowly conveyed in the axial and rotational direction. Figure 5.12 shows an isometric view of the plug section showing the rotational direction of the screw portion within the plug section, the direction of the material, and a simple schematic of the forces acting on the screw shaft surface.

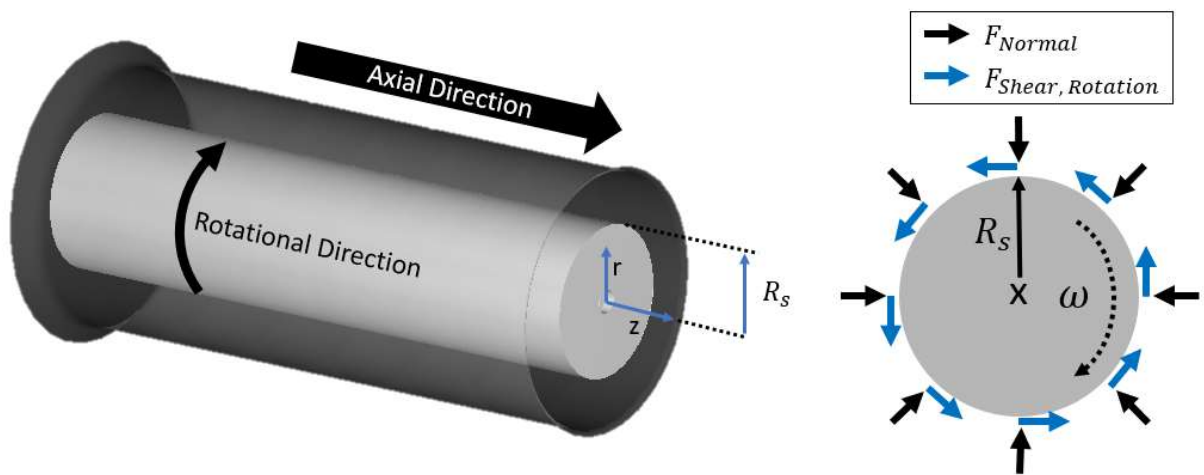


Figure 5.12: Plug section torque model. The shear and normal stresses are shown for a differential axial slice of the screw shaft.

To simplify the analysis further, the following assumptions are made:

1. The Coulomb friction model can be used with a constant friction coefficient over the length of the shaft to relate the normal and shear force.
2. The system is axisymmetric.
3. The translational velocity of the material is much less than the rotational velocity at the surface of the screw.

Due to the assumption that the system is axisymmetric, the problem is reduced to one dimension and changes in the rotational direction are not considered. If the screw is sliced many times in the axial direction, an expression can be developed for the torque required to rotate each section. The sum of these small torques can be used to calculate the full torque required to rotate the screw in the plug section with,

$$Plug\ Torque = \Sigma dT_z \quad (64)$$

The torque on a single differential slice of the screw can be calculated with the following analysis,

$$dTorque(z) = dT_z(z) = R_s * F_{shear} \quad (65)$$

In the plug section of a screw feeder material is sliding axially as the screw shaft rotates beneath the material. The relative velocity between the material and the shaft generates a frictional force, which has a rotational component and an axial component. However, assumption three above results in the rotational component of the frictional force being much larger than the axial component., and the full magnitude of Coulomb friction acts in the rotational direction. Using the area of a differential axial slice, the pressure at that axial location, and the coefficient of friction, the following equation can be developed to describe the torque of a differential slice.

$$dT_z(z) = 2\pi R_s^2 \mu_w P_z dz \quad (66)$$

The equation can be discretized by using average values for the radius of the screw shaft and the solid pressure if they change ( $\bar{R}$  and  $\bar{P}_z$ ), producing

$$\Delta T_z(z) = 2\pi \bar{R}_s^2 \mu_w \bar{P}_z \Delta z \quad (67)$$

Thus, the total torque on the plug section is,

$$Plug\ Torque = \Sigma_1^n (2\pi \overline{R_s^2} \mu_w \overline{P_z} * \Delta z) |_z \quad ; \quad where\ n = L_{plug} / \Delta z \quad (68)$$

### 5.3.2 Screw Section Model

Using a set of simplifying assumptions, the pressure, geometry, and material properties within the screw flights are used to develop a torque model. The assumptions are:

- 1) The Coulomb friction model can be used with a constant friction coefficient over the length of the screw channel to relate normal and shear forces.
- 2) The material is in a hydrostatic stress state, on average, within the screw flights.
- 3) The material is contacting all screw surfaces and is slipping against them at the average helical angle in the down-channel direction.
- 4) The pressure evolution occurs along the helical path situated between the leading and trailing flight, and the shaft and case radius.
- 5) At any position along the helix, the solid pressure maintains its full magnitude near the leading and trailing flight surface.
- 6) All stresses are evenly distributed over the face that they act on, such that the resultant forces act at the centroid of the face.

The screw section is geometrically more complex than the plug section, and therefore the differential elements are also more complex. However, the torque required to rotate the screw will still be calculated as a summation of differential torques with,

$$Total\ Torque = \Sigma T_z \quad (7)$$

Under the set of simplifying assumptions, the differential element can be chosen to take advantage of the assumption of hydrostatic stress to simplify the problem further. To visualize this process, Figure 5.13 shows a differential element of material within the screw flight and highlights the three surfaces in which the material interacts with the screw: the screw shaft, the trailing flight, and the leading flight.

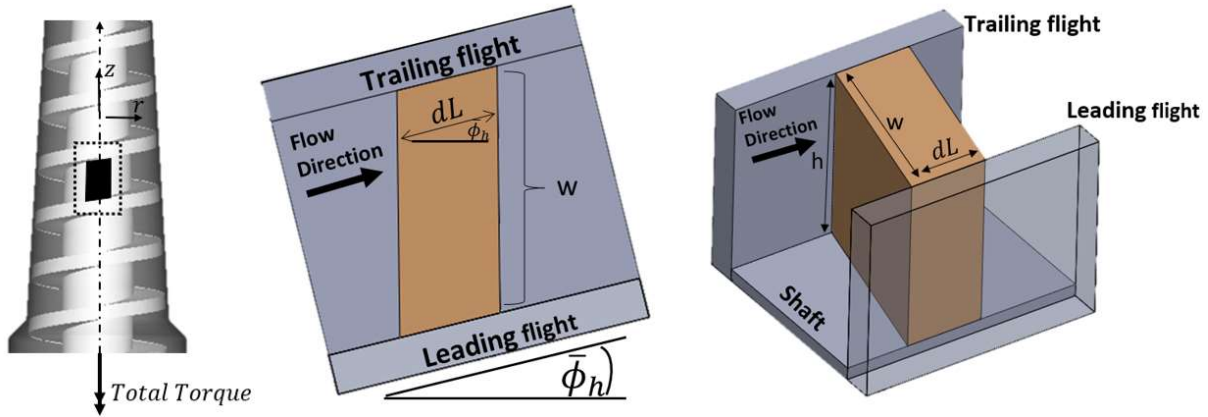


Figure 5.13: Differential element of material interacting with the screw feeder surface.

Once the screw surfaces that touch the material are well defined, the forces that the material exerts on the screw can be calculated using the assumption of hydrostatic stresses. A “U” shaped differential piece of the screw defined at each helical and axial position is used to generate a relationship between the solid stresses exerted by the material on the screw and the reaction torque generated by these solid stresses. The shape and top-down view are shown in Figure 5.14, which resembles Figure 2.4 but only shows the forces that the solid material exerts on the screw faces, as these are the forces that generate screw torque. Also important is that under assumption 6, the reaction forces generated by the solid pressure act at the radii shown in Figure 6.14.

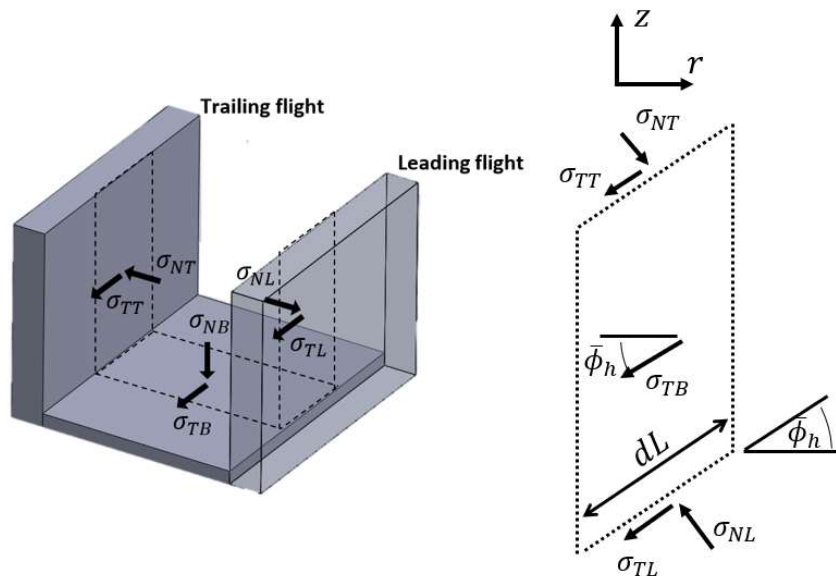


Figure 5.14: Screw torque model differential element. Only the stresses that the material exerts on the screw faces are considered.

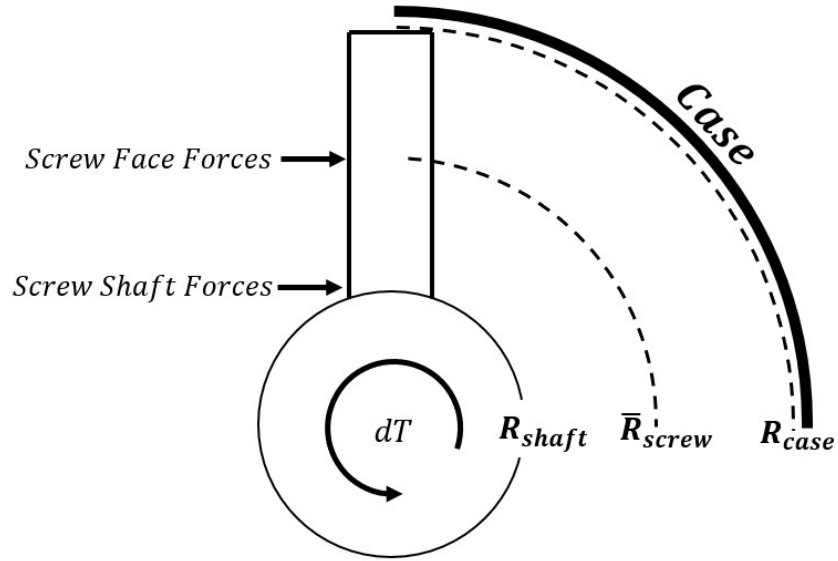


Figure 5.15: Radii at which the forces act about the screw axis. Looking down the length of the screw, assuming all stresses act at the center of their respective faces, the radii at which they act are known.

On one element of the screw, the total torque acting can be calculated with the following relationship;

$$dT_z(z) = \mathbf{R}_{shaft} \times \mathbf{F}_{screw,shaft} + \bar{\mathbf{R}}_{screw} \times \mathbf{F}_{screw,face} \quad (69)$$

$$dT_z(z) = R_{shaft,z} \sigma_{TB,z} \cos(\bar{\phi}_h) A_{B,z} + \bar{R}_{screw,z} (\sigma_{TL,z} \cos(\bar{\phi}_h) A_{L,z} + \sigma_{NL,z} \sin(\bar{\phi}_h) A_{L,z} + \sigma_{TT,z} \cos(\bar{\phi}_h) A_{T,z} - \sigma_{NT,z} \sin(\bar{\phi}_h) A_{T,z}) \quad (70)$$

where the areas of the different faces are shown in Figure 5.13 and Figure 5.16.

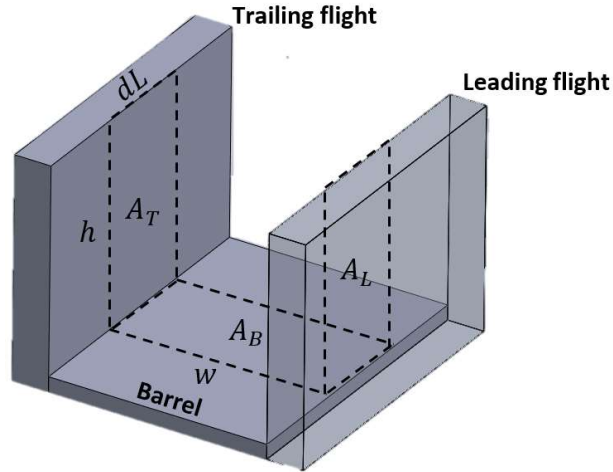


Figure 5.16: Screw differential element shape. The areas of each face are defined in terms of known geometric parameters,  $h$ ,  $w$ , and  $dL$ . It is important to note that  $dL$  is in the helical direction.

Under the assumption that the material is in a largely hydrostatic pressure state ( $\sigma_{NL} \cong \sigma_{NT} \cong \sigma_{NB} \cong \text{Pressure}$ ), substituting the equations for the face area and Coulomb friction ( $\sigma_T = \mu\sigma_N$ ) and noting that the normal interactions at the leading and trailing edges cancel out leads to the following form of differential torque,

$$dT_z(z) = P_z \mu_w (2h_z \cos(\bar{\phi}_h) * \bar{R}_{screw,z} + w_z \cos(\bar{\phi}_h)^2 * R_{shaft,z}) * dL \quad (71)$$

It is important to consider that the differential length of the element used,  $dL$ , is not aligned with the axial direction of the screw and the coordinate system of  $dT$ . Therefore, the final step is to convert from the helical path,  $dL$ , to the axial path,  $dz$ . The relationship between  $dL$  and  $dz$  is described in Figure 5.17, and yields the following equation,

$$dL = \frac{dz}{\sin(\bar{\phi}_h)} \quad (72)$$

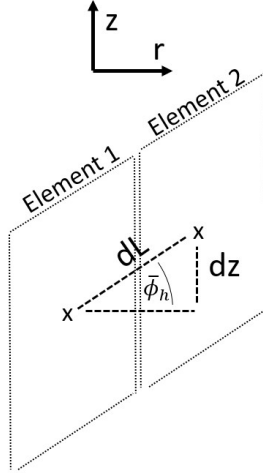


Figure 5.17: Relationship between the helical and axial direction. By placing two differential elements next to one another it is possible to construct the relationship between the helical and axial direction.

Substituting this expression into the analysis,

$$dT_z(z) = \frac{P_z \mu_w}{\sin(\bar{\phi}_h)} (2h_z \cos(\bar{\phi}_h) * \bar{R}_{screw,z} + w_z \cos(\bar{\phi}_h)^2 * R_{shaft,z}) * dz \quad (73)$$

This relationship can be discretized to simplify the form to,

$$\Delta T_z(z) = \frac{\bar{P}_z \mu_w}{\sin(\bar{\phi}_h)} (2\bar{h}_z \cos(\bar{\phi}_h) * \overline{R_{screw,z}} + \bar{w}_z \cos(\bar{\phi}_h)^2 * \overline{R_{shaft,z}}) * \Delta z \quad (74)$$

Next, the differential torque for each segment can be summed to develop an equation to calculate the full screw torque,

$$\begin{aligned} \text{Screw Section Torque} = \\ \sum_1^n \frac{\bar{P}_z \mu_w}{\sin(\bar{\phi}_h)} (2\bar{h}_z \cos(\bar{\phi}_h) * \overline{R_{screw,z}} + \bar{w}_z \cos(\bar{\phi}_h)^2 * \overline{R_{shaft,z}}) * \Delta z ; n = \frac{L_{screw}}{\Delta z} \end{aligned} \quad (75)$$

#### 5.4 Analytical Models Summary

The purpose of this chapter was to present a procedure for calculating the total torque required to run a compression screw feeder comprised of two distinct sections: a screw section and a plug section. First, analytical descriptions of the solid stress were developed for each region, and then basic mechanics were applied to develop a relationship between solid stress and screw torque. The models presented in this chapter are meant to serve as a first-order approximation to the screw

torque, and each individual model can be independently investigated and improved to produce a better result. The plug pressure model is the most important model because it is used to predict the peak pressure in the system, which directly affects the torque model in the plug section and the screw section. This approach, which starts at the exit and develops a pressure profile moving upstream, is different than the conventional approach, which seeks to start at the hopper and move downstream. The plug section is geometrically much simpler, and is also easier to study experimentally, which would allow for easier future developments of a better plug pressure model.

## 6. ANALYTICAL MODEL INPUT PARAMETERS

The analytical models developed depend on the geometry of the screw feeder, and the material properties that conventionally describe the bulk material behavior.

Table 6.1 shows the properties, excluding the geometry, that the analytical models use to calculate both pressure and torque. First, the outlet axial stress,  $\sigma_{zz,outlet}$ , represents the backpressure and therefore the lowest pressure of the plug section. This is a known property and represents what would be the pressure inside of the reactor at the outlet of the compression screw feeder. The Walker distribution parameter,  $D$ , is applicable in the plug section of the screw feeder and represents the relationship between the average axial stress, and the axial stress near the boundaries. To simplify the analysis the parameter is taken to have a value of 1, representing the case where the axial stress is uniform over the cross-section. The axial stress has been seen to change in DEM simulations near the boundaries and significantly affect friction at the walls. However, the Walker parameter is not a focus of this chapter. The other two friction properties in the table as well as some of the complex geometry of the screw feeder will now be discussed.

Table 6.1: Non-geometric model input properties. All other model parameters are known and well defined.

Input Parameter	Notation
Outlet Pressure	$\sigma_{zz,outlet}$
Wall Friction Angle	$\phi_{wall}$
Internal Friction Angle	$\phi_{internal}$
Walker Distribution Parameter	$D$

### 6.1 Screw Geometry

One of the benefits of using a simple model for the evolution of stress and torque in the screw section of the feeder is that most of the inputs are well defined and measurable. Considering a continuum description of the material within the screw flights and performing a differential analysis like that performed by Darnell & Mol (1956) requires several complex geometric input properties. One of these properties, the conveying angle  $\alpha_c$ , is a complicated parameter that

describes the direction of the frictional force of the case on the material in the screw flight. The conveying angle is dependent on the mass flow rate, and either requires the mass flow rate to be assumed or an expression for the flow rate to be developed. The model and procedure presented in the current work are independent of the mass flow rate.

The most complicated geometric input parameter in the current work is the helical angle shown in Figure 6.1, which represents the “tilt” of the flight face. The helical angle is directly related to screw pitch, screw thickness, and screw radius, and therefore plays a role in determining the way material conveys in the system and the amount of torque generated by the screw faces. The angle can be calculated by considering the two different motions along the helical path of one screw flight: axial and rotational (Figure 6.2). Figure 6.1 shows two helical paths, one at the screw core and one at the screw case. The helical angle of these paths is shown as  $\phi_h$ , and is defined for a screw pitch and radial position. To simplify calculations, an average helical angle is used and calculated at the average radius using the following equation;

$$\bar{\phi}_h = \arctan\left(\frac{Pitch}{2\pi\bar{R}}\right) \quad (76)$$

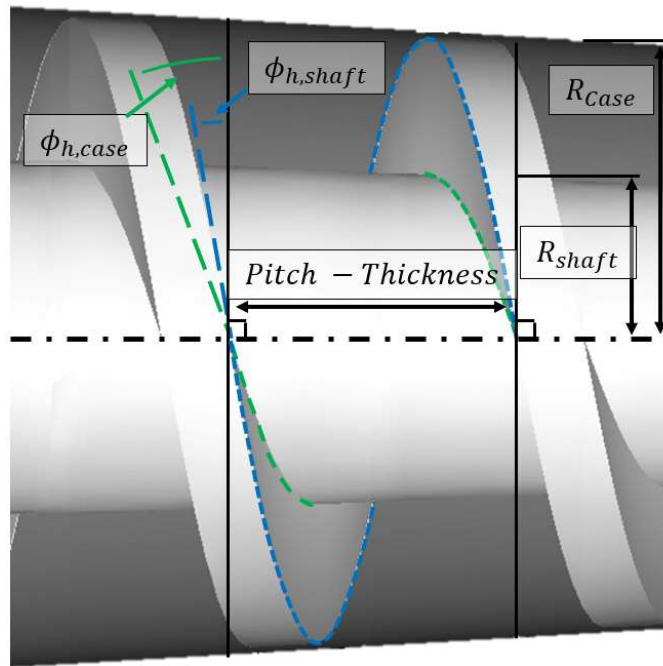


Figure 6.1: Helical angle at the screw shaft and at the screw case. Because the helical angle changes as a function of the radius on the screw face, a single average value must be used.

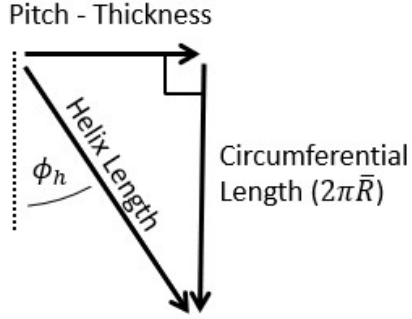


Figure 6.2: Helical angle calculation. Using the average radius, the flight thickness, and the screw pitch, the average helical angle can be calculated.

## 6.2 Friction Coefficients and Friction Angles

The friction angle is a common bulk material property used to describe the relationship between normal stresses and shear stresses within bulk materials. Two friction angles arise from the Mohr-Coulomb failure theory of granular media, and a basic understanding of this theory is required to understand the analytical models and their inputs. The first friction angle is called the internal friction angle ( $\phi_i$ ) and arises from the observation that the shear strength of a bulk material increases with an increase in compressive loading. This angle defines the growth in shear strength (resistance to flow) with respect to normal stress with the following equation,

$$\tau_f = \sigma \tan(\phi) + c \quad (77)$$

where  $\tau_f$  is the shear strength (or failure stress),  $\sigma$  is the normal stress,  $\phi_i$  is the internal angle of friction, and  $c$  is the cohesion. This line is called the internal yield locus (IYL), and can be obtained with a machine such as a Schulze Shear Cell, which directly measures shear strength of a material at multiple, increasing compressive loads. The Mohr's circle for a powder bed cannot pass beyond the IYL because when the stress at any point reaches the locus, the material will flow.

The second friction parameter is called the wall friction angle, and is represented as  $\phi_{wall}$ . This parameter provides the relationship between normal stress and shear stress as a bulk material slides along a boundary with the equation,

$$\sigma_{shear} = \sigma_{normal} \tan(\phi_w) \quad (78)$$

where  $\sigma_{she}$  is the shear stress on the material,  $\phi_w$  is the wall friction angle, and  $\sigma_{normal}$  is the normal stress at the wall. In the case of the current work, the amount of shear stress that the screw

and case surfaces can exert on the material is limited by this equation, and if the material is slipping, the shear stress is known to be  $\sigma_{shear}$ . To measure this property, a simple bulk friction tester can compress a sample of material against a wall with a known normal stress, and the shear stress to slide the sample against the wall can then be measured. This phenomenon is captured by the wall yield locus (WYL), can also be shown on a Mohr's Circle diagram, and is used to provide the limit of shear stress at any of the boundaries (Figure 6.3).

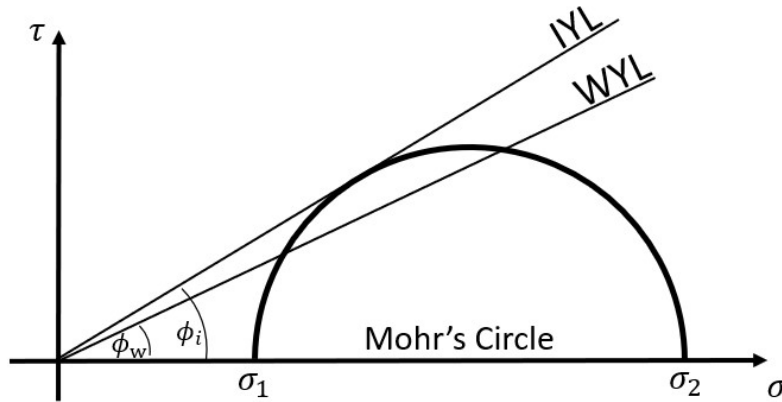


Figure 6.3: Internal yield locus and wall yield locus for a granular material. The Mohr's circle is always constrained by the internal yield locus, but the wall yield locus will intersect the Mohr's circle at two points. One of these points represents active failure, and the other represents passive failure.

Because the analytical models are being compared to DEM simulations, it is also necessary to consider how the DEM solver performs calculations related to friction. Within the DEM simulations, the user has direct control over the relationship between the normal force and the tangent force calculated at every contact. The following equations show the form of the friction calculation, and Figure 6.4 illustrates the simulated conditions,

$$F_T = \mu_{pp} F_N \tag{79}$$

$$F_T = \mu_{pb} F_N \tag{80}$$

where  $F_T$  is the tangent force at a contact,  $F_N$  is the normal force,  $\mu_{pp}$  is the particle-particle coefficient of friction, and  $\mu_{pb}$  is the particle-boundary coefficient of friction.

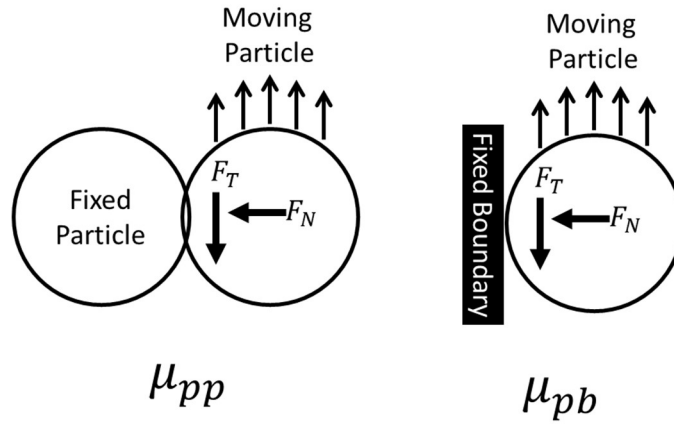


Figure 6.4: DEM friction coefficients are defined by the interacting bodies. The friction coefficients do not change under static or dynamic conditions and are represented by one value.

The simple Coulomb Limit friction model used in this work does not consider a difference between dynamic and static friction, and they are taken to have the same value. Additionally, all screw system surfaces are assumed to be made from the same material and therefore have the same particle-boundary friction coefficient. The coefficient of friction is also taken as a constant with respect to the applied normal force. This assumption has been shown to be flawed (Mehrishal et al., 2016), but is still used in this work to simplify the analysis.

The final important consideration is how to compare DEM simulations that use particle-level friction coefficients as an input with an analytical model that use bulk friction angles. The challenge of relating particle properties to bulk properties is an ongoing research area and for this work a simple relationship is considered, beginning with the wall friction angle. The DEM simulations use a friction coefficient that can be directly related to the wall friction angle,  $\phi_w$ . The DEM particle-boundary friction coefficient for a non-rotating particle is identical to the tangent of the bulk wall-friction angle,

$$\mu_{pb} = \tan(\phi_w). \quad (81)$$

The relationship between the internal friction angle and particle-particle coefficient of friction is more complex, and depends on particle shape, particle size, size distribution, tangent force model, normal force model, and more. However, irrotational spheres have been studied in this context before (Ketterhagen et al., 2009), and the relationships shown in Figure 6.5 is used to

convert between the two properties and compare DEM simulations predictions against analytical model predictions.

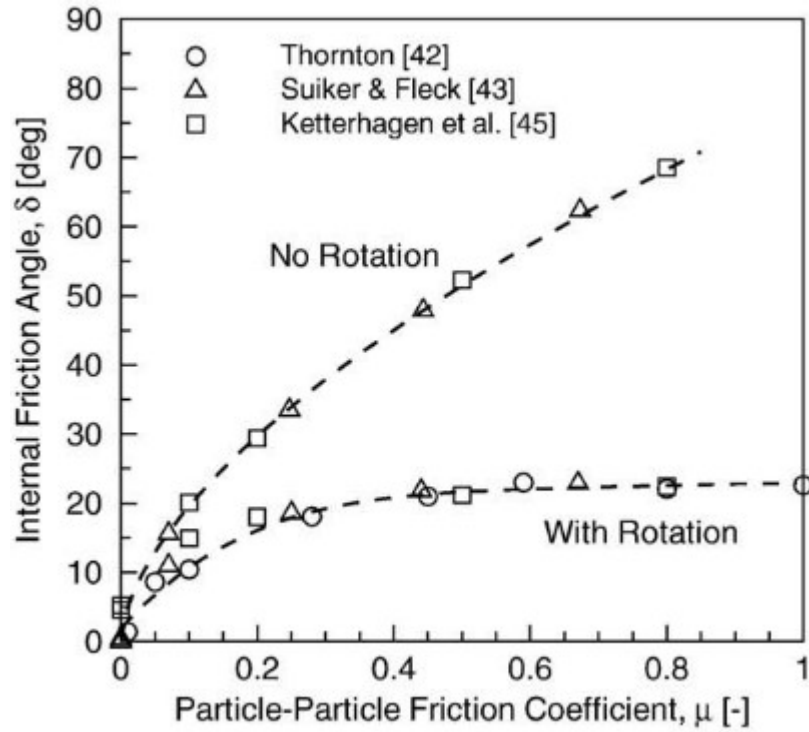


Figure 6.5: Relationship between DEM friction coefficient and bulk friction angle (Ketterhagen et al., 2009). The current work uses non-rotational particles, and therefore the upper curve is used to map particle-particle friction coefficient (DEM input) to internal friction angle (analytical model input).

## 7. COMPARISON OF ANALYTICAL MODELS TO DEM SIMULATIONS

In this chapter, the various trends and behaviors predicted by the analytical models are compared to DEM simulations, and their accuracy is assessed. The simulations compensate for the lack of experimental data and also allow for direct comparison of stress and torque trends that cannot be measured in an experimental apparatus.

### 7.1 Plug Section And Screw Section Pressure Models

The first step in the torque prediction procedure is the calculation of the pressure in the plug section of the screw feeder. In this section the backpressure is known and all geometry and material properties are well defined or assumed to be constant. In Chapter 4.3, DEM simulations of a standalone plug section were presented, and their trends were analyzed. These trends differed slightly from those seen in the full screw simulations presented earlier in that chapter, and these differences are highlighted when comparing the DEM simulation results to their respective analytical models.

Using the input properties shown in Table 7.1, the analytical model for pressure (Equation 42) is compared to the standalone plug simulations, with results shown Figure 7.2. The inputs for the analytical models are directly analogous to those from the DEM simulations, as described in Chapter 6. The model predicts a pressure trend like that shown in DEM simulations, but does not capture the peak value. Although the peak value is not predicted accurately, deviating as much as 100%, the prediction is on the same order of magnitude even with the many simplifying assumptions used in the analytical model (hydrostatic stress state, Walker distribution parameter is unity, etc.).

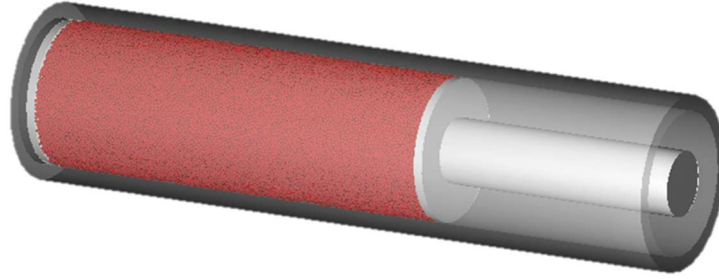


Figure 7.1: Straight plug section simulation.

Table 7.1: Straight plug model input parameters. These parameters were chosen using Figure 6.5 to provide a valid comparison between DEM and the analytical models.

Input Parameter	Notation	Value
Outlet Pressure	$\sigma_{zz,outlet}$	99 [kPa]
Wall Friction Angle	$\phi_w$	0.291 [rad]
Internal Friction Angle	$\phi_i$	1.047 [rad]
Walker Distribution Parameter	$\mathcal{D}$	1

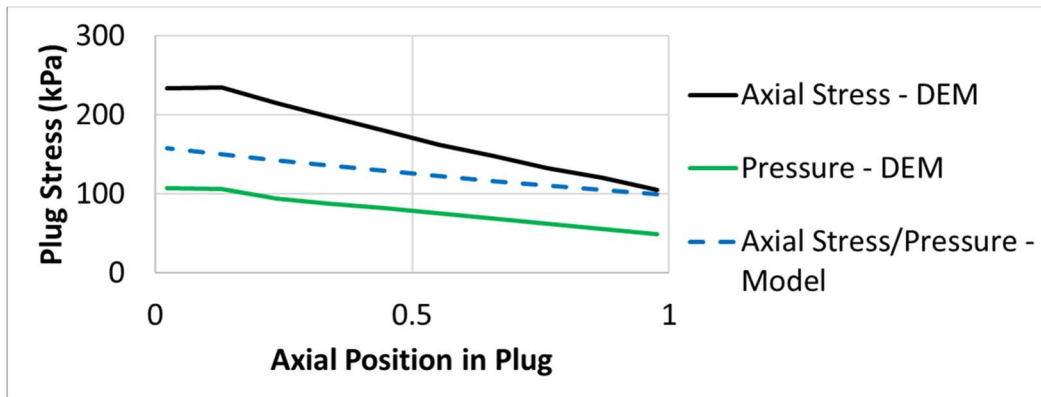


Figure 7.2: Comparison of Equation 42 to DEM simulations. The model for pressure lies between the axial stress and the pressure measured in DEM, and predicts a peak stress on the correct order of magnitude.

The plug pressure model can also be compared against the stresses measured in the converging DEM simulations. Table 7.2 shows the inputs used in Equation 59 to develop predictions for the system shown in Figure 7.3. Figure 7.4 shows good agreement with the model near the low-pressure, straight section of the converging plug. However, beginning at a dimensionless position of 0.2 from the exit where the taper starts, the model deviates significantly

from the observed DEM behavior. The mathematical cause of this behavior is discussed in the following paragraphs, but a deep understanding of which assumptions or analysis steps cause the model to mis-predict the behavior in this section is not clear.

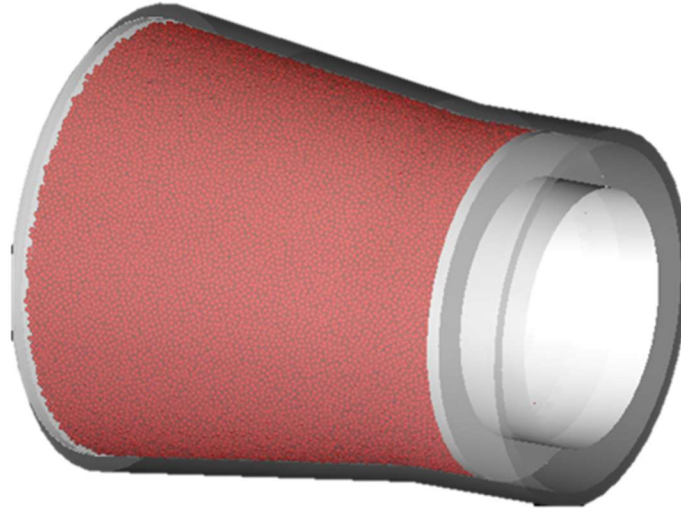


Figure 7.3: Converging plug section simulation.

Table 7.2: Converging plug model input parameters. These parameters were chosen using Figure 6.5 to provide a valid comparison between DEM and the analytical models.

Input Parameter	Notation	Value
Outlet Pressure	$\sigma_{zz,outlet}$	36 [kPa]
Wall Friction Angle	$\phi_{wall}$	0.291 [rad]
Internal Friction Angle	$\phi_{internal}$	1.134 [rad]
Walker Distribution Parameter	$D$	1

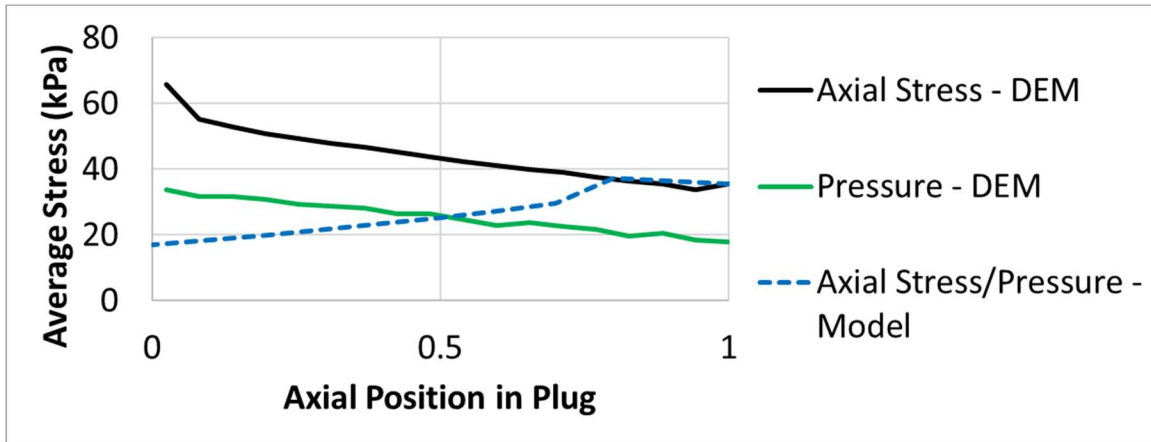


Figure 7.4: Comparison of Equation 59 to plug DEM simulations. The straight section of the converging plug simulations (from a dimensionless axial position of  $\sim 0.8$ -1.0) are well captured by the analytical model, but the converging section (from a dimensionless axial position of 0- $\sim 0.8$ ) is not captured by the analytical model.

The analytical model shown in Equation 59 contains four terms that contribute to the sign of the exponential growth in pressure: the inclined normal force at the case, the shear force at the case, the shear force at the shaft, and the pressure change due to the change in the area. These four contributing factors are shown in Figure 7.5, and the sign of their sum determines whether the models predict a pressure rise or fall. In the case of the simulated screw, using the material properties input to the DEM simulations, the models predict that the term that captures the change in area dominates the stress behavior and causes the predicted stress gradient to be negative. The assumption of uniform stresses over the cross section is suspected to contribute to this problem, but a deeper analysis is required in order to understand why the analytical model behaves this way.

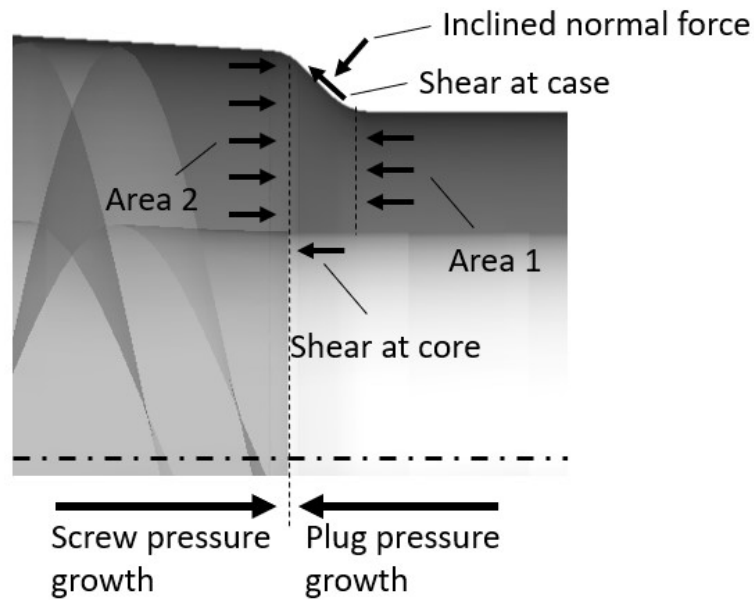


Figure 7.5: Factors contributing to the pressure change in a converging plug. Each of these factors (area, inclined normal force, shear force at case, shear force at core) are accounted for with a distinct term in the converging plug model.

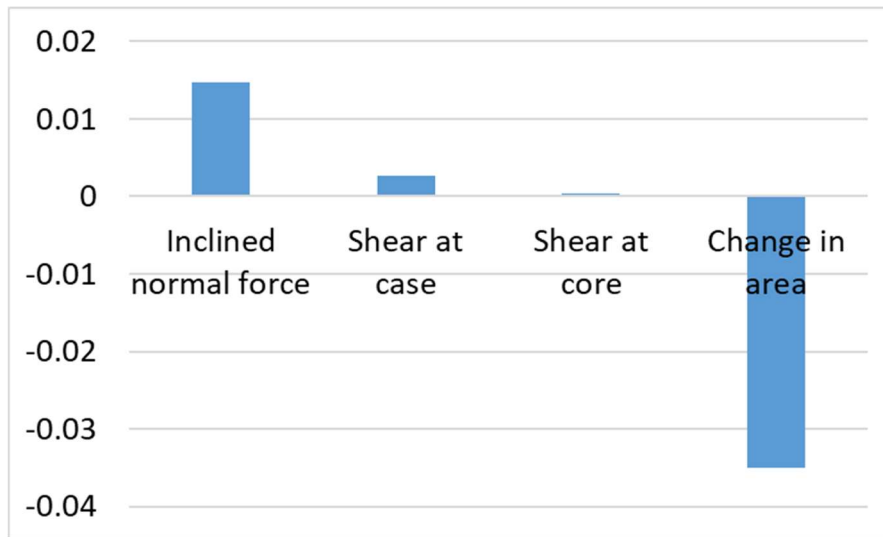


Figure 7.6: Relative magnitudes of terms in the plug section of the screw feeder. The contributions of each factor are summed to determine the sign and magnitude of the exponential growth predicted in the plug section, and the change in area contributes a large negative value.

Figure 7.7 shows the general geometry for the plug section of a screw feeder, showing only the particles in the plug section. As discussed in the DEM section, the stress state of the material in the screw feeder is largely hydrostatic on average, and therefore the pressure is the most suitable point of comparison. Using the input properties shown in Table 7.3, Figure 7.8 shows two pressure

curves with different internal friction angles. The DEM simulations use a particle-particle coefficient of friction, which corresponds roughly to a  $50^\circ$  internal angle of friction and a curve corresponding to an internal angle of friction of a  $65^\circ$  was shown to demonstrate the sensitivity of the pressure to that parameter. Additionally, the Walker distribution parameter can be varied to achieve a similar fitting. Like the converging plug simulations, the model provides a reasonable prediction of the pressure curve until the tapering geometry is encountered by the material. At a dimensionless axial position of 0.9. At this position, the analytical model predicts a sudden decrease in the stress due to the change in cross sectional area.



Figure 7.7: Screw simulation showing only the particles in the plug section.

Table 7.3: Analytical model parameters used in the plug model in order to compare results with the screw simulation. These parameters were chosen using Figure 6.5 to provide a valid comparison between DEM and the analytical models.

Input Parameter	Notation	Value
Outlet Pressure	$\sigma_{zz,outlet}$	273 [kPa]
Wall Friction Angle	$\phi_{wall}$	0.381 [rad]
Internal Friction Angle	$\phi_{internal}$	0.873 [rad] (50 degrees) 1.134 [rad] (65 degrees)
Walker Distribution Parameter	$D$	1

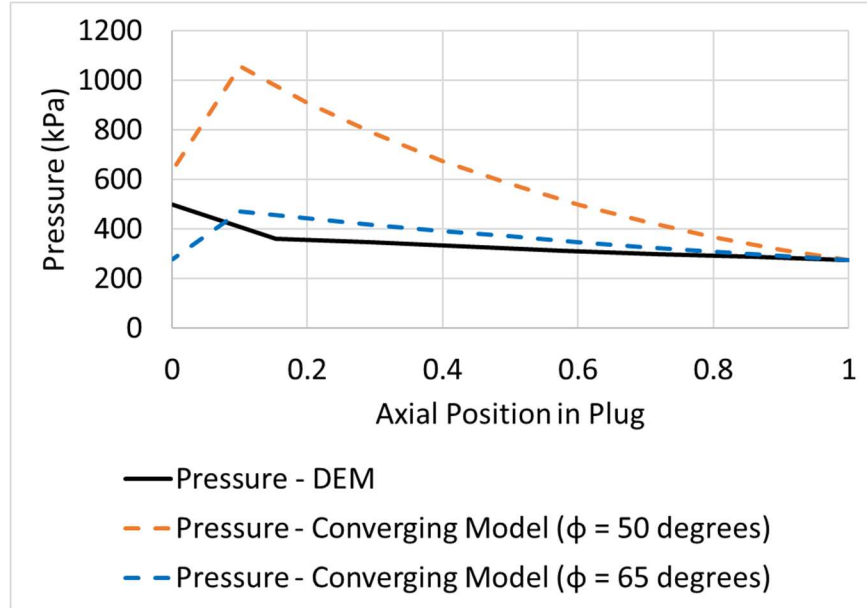


Figure 7.8: Comparison of Equation 59 to screw DEM simulation. The straight section of the plug (from a dimensionless axial position of  $\sim 0.15$ -1) is captured well if the internal friction angle is varied, and similar results are obtained if the Walker distribution factor is varied) However, the converging section (from a dimensionless axial position of 0- $\sim 0.15$ ) is not captured.

Once the maximum pressure is predicted from the growth in the plug section, the value is used as an input to the screw section model. Figure 7.9 shows the analytical model developed in Chapter 5.2.1 to predict the pressure in the screw section. The model requires a peak pressure prediction, which usually comes from the plug model, but in Figure 7.9 the peak pressure is taken directly from the DEM simulations. In developing the analytical model, exponential and power-law relationships predicted too much curvature in the profile, and a linear profile fit many of the DEM simulations well. However, in general, the proposed polynomial fit does a good job of matching the magnitude of pressure and the rate of change over various screw pitches and backpressures. It is important to note again that the accuracy of this prediction depends entirely on the accuracy of the predicted peak pressure coming from the plug pressure model.

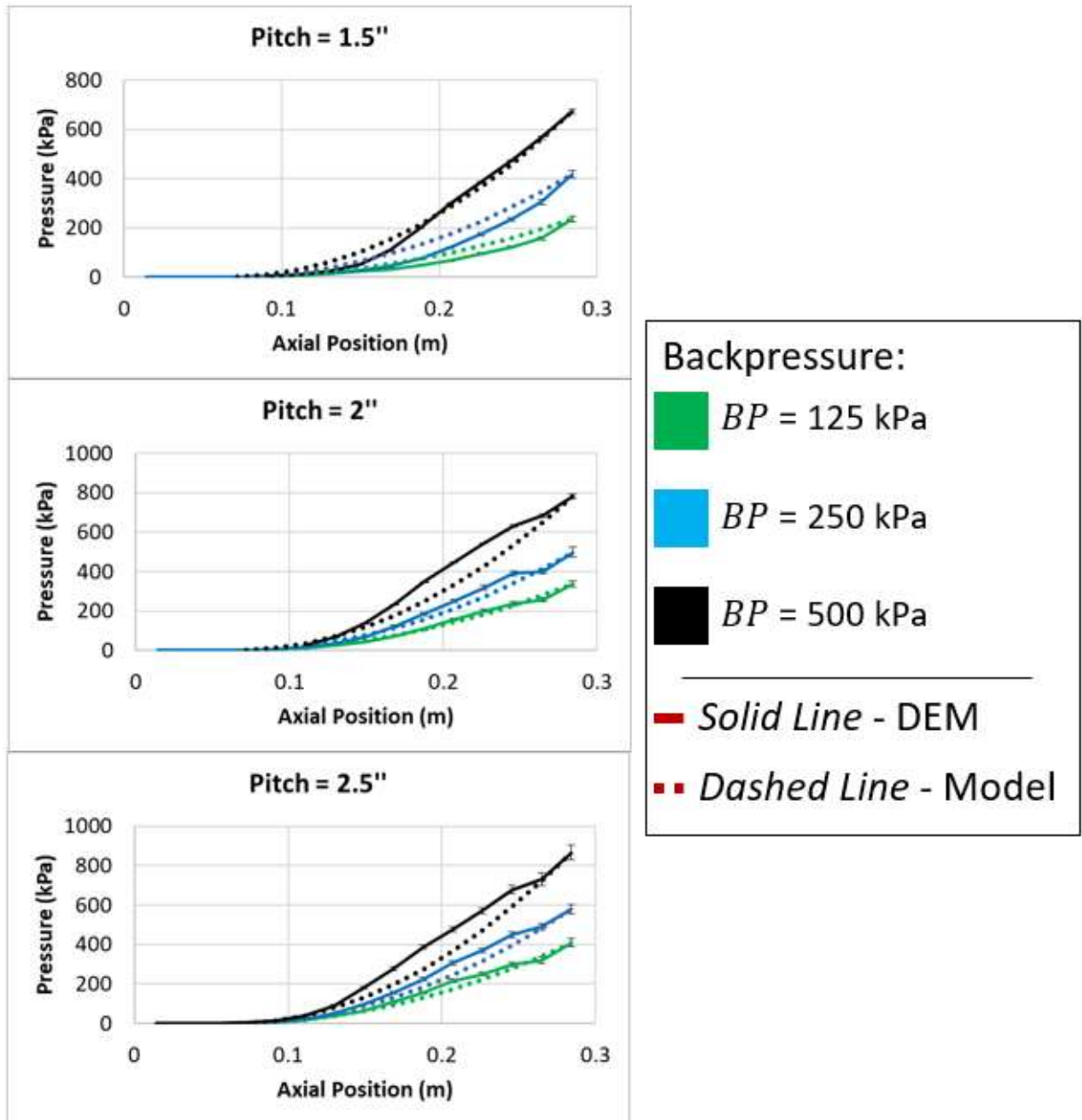


Figure 7.9: Model predictions of DEM pressure values,  $\mu_{pp} = 0.5$  if the peak pressure is known. The quadratic form fits the data well and matches the curvature at the high pressure region at the end of the screw flights, although in some cases, a linear fit provided a better match.

## 7.2 Plug Section Torque Model

Although the screw section contributes the largest percentage to the total torque of the screw feeder, more than 10% of the torque is still generated within the plug section. Figure 7.10 compares the predicted torque values with the analytical torque model. One set of points is generated using

the predicted pressure profile from the plug section pressure model, labeled “Predicted Pressure”. Because the torque model is based on the pressure prediction, and the pressure predictions generally overpredicted the peak pressure in the screw feeder (especially for values of internal friction angle), the torque values were also overpredictions. However, the accuracy of the torque model can be assessed by using the DEM pressure as an input instead of the pressure model predictions. This curve, labeled “DEM Pressure”, represents the case where the model exactly matches the DEM pressure and significantly improves the torque prediction. However, even with the correct pressure profile, the torque model overpredicts the steady-state screw feeder torque. It is suspected that the assumption of uniform, hydrostatic stress is the main factor causing overpredictions. It was seen in Figure 7.2 that in an axially compressed, annular bed, the stresses in the radial and theta direction pressure were lower than the axial direction. Additionally, though not presented in this thesis, simulations showed that radial stress decreases when approaching the core and case in the plug section. The radial stress is what is acting normal to the screw surface and generating the torque-causing shear force as the screw slips under the material. Because the model assumes that the radial stress is larger than it is, the torque is overpredicted, and a better understanding of the stresses in the plug section would improve the torque model.

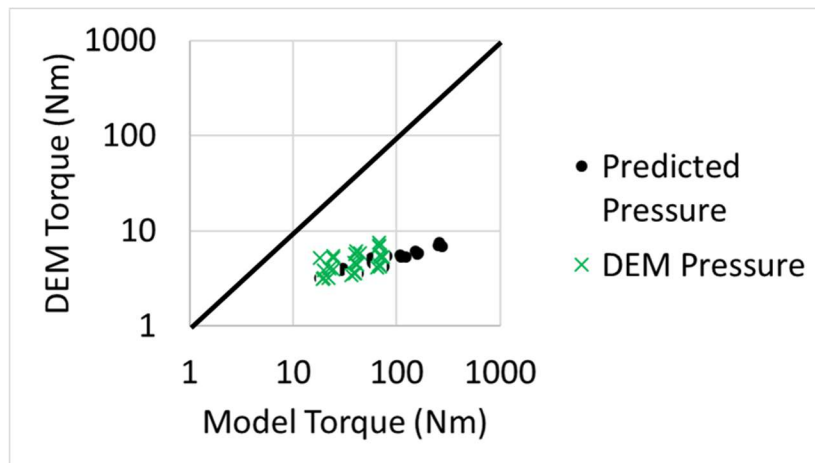


Figure 7.10: Plug section torque model compared against DEM torque values. The plug torque is overestimated by the model even if the DEM pressure is used.

### 7.3 Screw Section Torque Model

The DEM simulations suggest that the screw section is the largest torque contributor to the system, and Figure 7.11 shows that the screw section torque model overpredicts the torque for all

combinations of backpressure, pitch length, and internal friction angle. Like in the plug section, the torque analytical model results are tested using the predicted pressure profile, as well as the profile measured in Rocky. Using the DEM pressure improved model agreement with simulations, but in the cases of high backpressure and low internal friction angle, the overestimates are close to one order of magnitude.

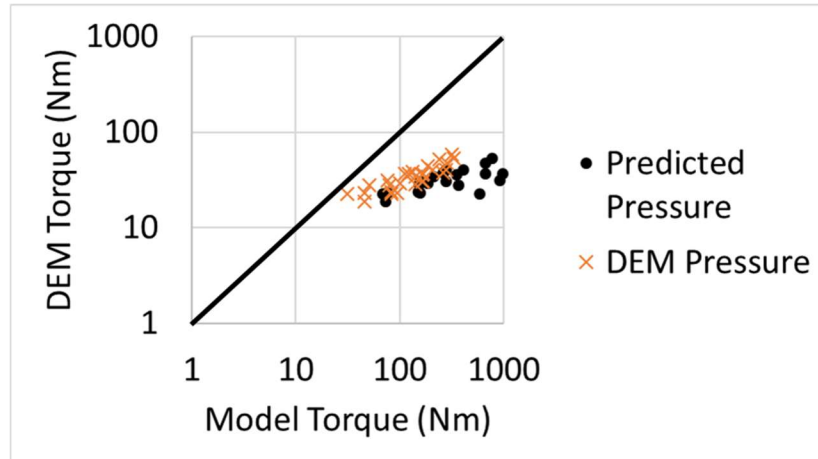


Figure 7.11: Screw section torque model compared against DEM torque values. The screw torque is overestimated by the model even if the DEM pressure is used.

There is still significant progress to be made when attempting to predict the relationship between material properties, geometry, and a pressure profile. In the current state, the model predicts that all screw surfaces generate torque, and specifically the shear force on the leading and trailing flight generate an equal torque. Figure 4.27 shows that interactions at the trailing flight may not be dissipating energy at all, and in fact, may be making the screw easier to rotate. If the contribution from the trailing flight is removed entirely from the final equation of the torque calculation, the prediction again improves drastically. Figure 7.12 shows that all predictions are improved for the total torque if the modified torque equation is applied. Although this is only a small example of an empirical improvement that could be made, the way material interacts with the different screw surfaces is still misunderstood.

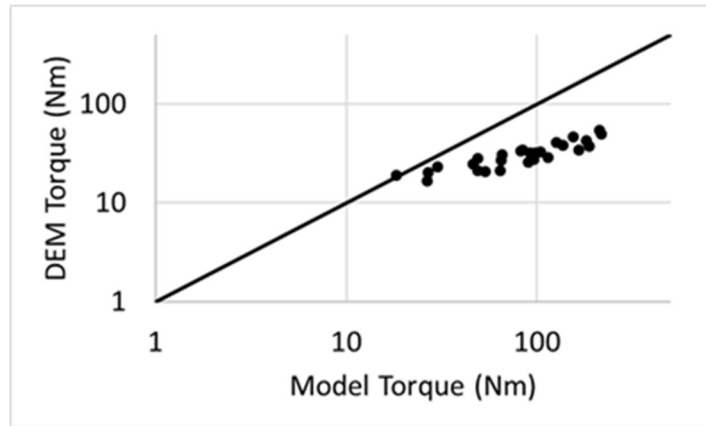


Figure 7.12: Modified torque model with DEM pressure curve. By removing the contribution of the trailing flight from the final form of the torque model, the prediction is improved significantly. This modification is motivated by Figure 4.27.

#### 7.4 Full Screw Comparison

Because both the plug section and screw section models overpredicted the torque, the full screw torque is also an overprediction. The estimation is also drastically improved if the DEM pressure is used as an input to the torque model, suggesting that a correct pressure prediction significantly improves the ability of the torque model to capture the system behavior. Cases with low backpressures and high internal friction angles are best predicted by the model and almost match the DEM results, but cases with high backpressures and low internal friction angles are overpredicted by as much as an order of magnitude. Figure 7.13 shows the torque model's prediction using the predicted pressures and the DEM pressures, and Figure 7.14 shows the model with the trailing flight interactions removed.

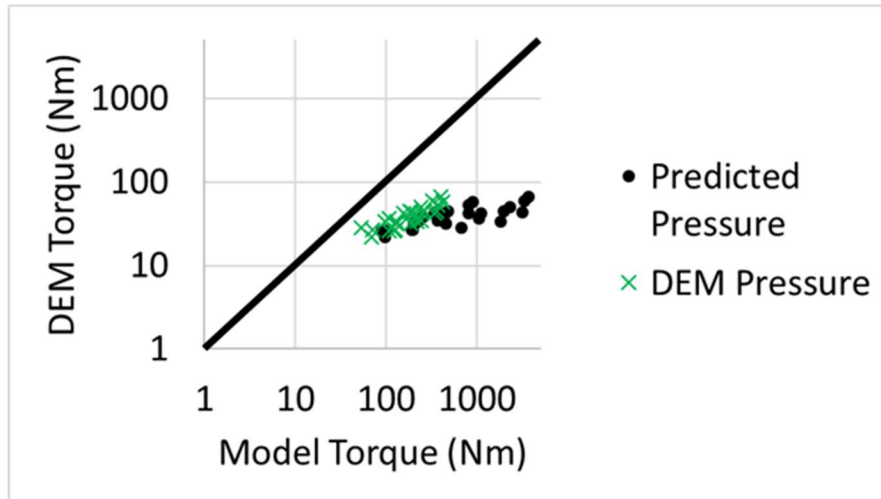


Figure 7.13: Full screw torque model predictions versus DEM torque. Both the plug section model and screw section model overpredicted the torque, and when combined, they overpredict the total torque. The predictions were worse for small internal friction coefficients and high backpressures.

Lastly, it is important to compare not only the magnitude of total torque predicted but also the torque contribution over the length of the screw. Comparing the torque contribution of the different segments of the screw determines whether a pressure-based torque model with constant properties is capable of capturing the shape of torque growth in each section of the screw. Figure 4.25 and Figure 4.26 show that the DEM pressure growth is not directly proportional to the torque contribution, and Figure 7.15 demonstrates that the analytical torque model does not match the DEM torque profile, especially near the end of the screw flights where the most torque is generated. The model does exhibit some downward inflection at the end of the screw flights due to geometry changes, but the shape is not the same as that measured in the DEM simulations.

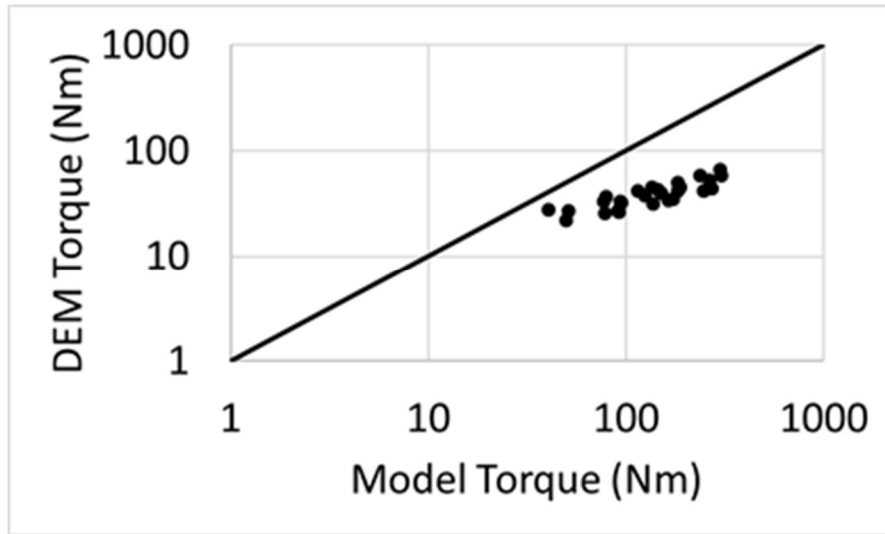


Figure 7.14: Full screw torque model predictions with modified torque model and DEM pressure (no trailing flight). By modifying the torque model using conclusions from the DEM simulations, it is possible to significantly improve the match.

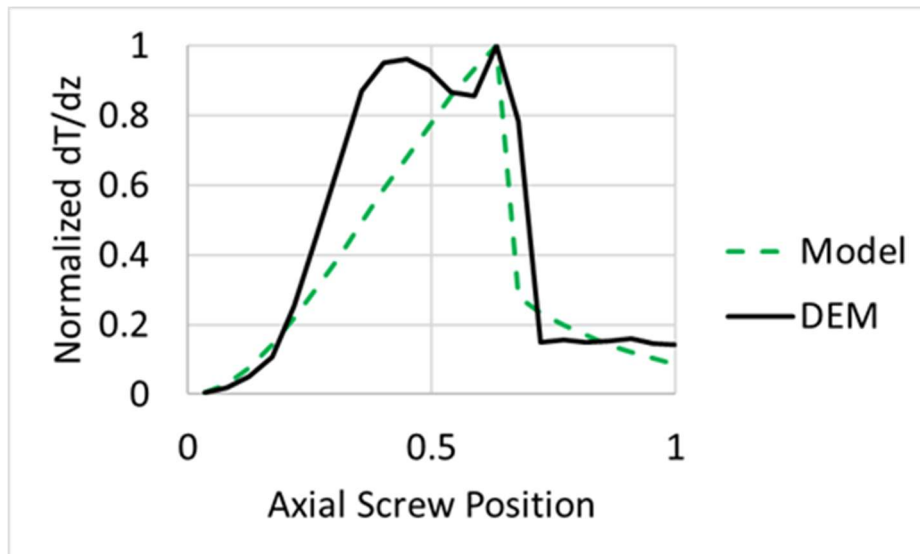


Figure 7.15:  $\frac{dT}{dz}$  shape for pressure-based torque model and typical DEM simulations. The curvature is not captured in the screw section or the plug section, and further investigation is needed.

## 8. SUMMARY AND CONCLUSIONS

The goal of this thesis is to develop a set of models to estimate the steady-state torque required to run a compression screw feeder that depends on screw geometry, material properties, and downstream operation conditions. There is currently no standard procedure for approaching this problem, and the way material interacts with the screw feeder is still not well understood. However, using DEM simulations to provide insight into the stresses and torques, two different regimes were identified inside the screw feeder, the screw section and the plug section, and their mechanics were investigated. The proposed method of torque calculation is accompanied by four independent models, a pressure model and a torque model for each of the two regimes of the screw feeder. Each of these models can be independently investigated and improved to provide a more accurate torque prediction, and the full model can be used both to predict sensitivity of torque to the bulk material properties of the material being passed through the screw and to better understand the design of screw feeders and how geometric parameters affect the outputs.

First, DEM models were used to inform the development of the analytical models presented later in the thesis. The DEM models showed many interesting phenomena regarding the evolution of stresses and torques within the screw flights and the plug section. The major conclusions were:

1. The solid stress growth in a plug screw feeder is not monotonic and reaches a peak at the end of the screw flights, then decreases in the plug section moving toward the outlet.
2. The stress throughout the screw is largely hydrostatic on average but does vary when approaching the boundaries.
3. The torque contribution by any location in the screw is not proportional to the average pressure, especially near the transition from the screw section to the plug section.
4. The screw torque required to drive each face of the compression screw feeder is not well understood, and although the material is shearing against all surfaces, the DEM simulations suggest that the trailing flight and the leading flight exhibit significantly different behavior.
5. The leading flight in the screw section contributes most of the total screw torque.
6. The standalone plug section simulations do not match the behavior within the plug section of the screw due to differences in the high-pressure, inlet boundary conditions.

Using the conclusions from the DEM simulations as a foundation, analytical models were developed to describe the pressure change and torque contribution within the plug section and

the screw section. Starting with the plug section, a model for the pressure evolution in the plug section of a compression screw feeder was developed based on Walker (1966) and Mohr-Coulomb failure theory. The plug pressure model was used to determine the peak pressure in the system, which serves as an input for the screw section pressure model. Using the pressure curve, geometric properties, and material properties, a simple mechanistic model was developed for the plug section and screw section to calculate the screw torque. These models assumed constant properties and a hydrostatic stress state and the only empirical property, the Walker distribution factor ( $\mathcal{D}$ ), comes from the plug pressure model. The torque model in its current state relies on the hydrostatic assumption and does not include variations in the material stresses near the boundaries.

Next, the input properties for these models and their connection with the DEM simulations were discussed before comparing the analytical models to simulation results. Due to a lack of experimental data, the DEM trends were used to assess the accuracy of the models. It was concluded that,

1. The torque model is most sensitive to the plug pressure model, since the peak pressure from the plug section model is used as a boundary condition for the screw section model.
2. The plug pressure model is sensitive to internal friction angle.
3. The plug pressure model can capture the pressure growth reasonably within the straight portion of the plug section. However, the model incorrectly predicts stress growth in the converging plug sections.
4. Even if the models perfectly predicted the pressure growth throughout the screw system, the current formulation of the torque model produces an overprediction.
5. Removing the contribution of the trailing screw flight from the final form of the torque model improved the prediction, but even so, the formulation is currently unable to match the relationship between pressure and torque at various positions in the screw.

This thesis provides an extension of existing models from two fields, plastic extrusion and hopper/silo mechanics, and applies their principals to a compression screw feeder to produce a prediction of the steady-state operational torque. The model can be easily implemented in a short Python code to provide rapid predictions of torque and as opposed to previous models, it is insensitive to screw speed and mass flow rate. Additionally, the pressure and torque predictions do not show prohibitive levels of sensitivity to backpressure, geometry, and internal friction

angle. Although all predictions from the model in its current state are over-predictions and the torque-pressure relationship is not well captured, this model can be incrementally improved to include a better understanding of the mechanics occurring in each section. The model combined with the DEM simulation results represents a significant step towards a better understanding of how the material in a screw feeder interacts with the screw surfaces and how torque is developed within a compression screw feeder.

## 9. FUTURE WORK

The most important element of future work in the opinion of the author is the development of novel experiments to characterize the behavior of different materials within the different screw sections. Instrumented dies could be used to understand how stresses change with axial and radial position within the plug section (only captured by the Walker distribution factor in the current work), and instrumented screw feeders could help understand how stress changes with axial position in screw feeders. The current assumption of a hydrostatic stress state in the whole screw system and constant material properties hinders the ability of the current model to capture real system behavior. It is suspected that the percentage of the average pressure that is realized at the walls changes with axial position in all sections of the screw feeder. This behavior may be one significant reason that the pressure-based torque model cannot capture the simulation measurements and motivates the need to understand individual stresses. Utilizing experiments, DEM simulations, and FEM simulations will each be important in building further understanding of how stresses change within a compression screw feeder.

Regarding DEM, the next step is a full parametric study of all dimensionless parameters that influence a compression screw feeder system. Many important system properties were left out of the current work and their effects could be characterized using DEM at a low cost. DEM will be especially useful in testing the effects of particle shape, particle size, and size distribution on the different stresses and torques measured within the system. Additionally, both DEM and FEM are critical in understanding the difference between average stresses and those measured near the boundaries, as these stresses cannot be easily measured in any experimental apparatus.

The effect of particle size on the DEM results must also be investigated for two reasons. The first reason arises due to the particle binning approach used to measure solid stresses in within the screw feeder. In order to obtain meaningful average values of the desired stresses, the particle bins must encapsulate a certain number of particles. Therefore, the minimum size of the particle bin scales directly with particle size and using a smaller distribution will allow for higher resolution measurements. A smaller particle bin can also be brought closer to the boundaries to extract measurements that better represent the stresses near the surface. The second reason for studying the size distribution is related to the geometry of the screw feeder. The first step in simplifying the compression screw feeder geometry was to eliminate all clearances smaller than the DEM particle

size, and to increase clearance in the plug section that was close to the size of the DEM particles. When the DEM particle size is close to the same size as the geometry being studied, particles do not pack correctly, cannot correctly mobilize friction, and cause wedging that does not occur in normal screw feeder operation. Therefore, it is recommended that the particle size in all future simulations is greatly reduced for added resolution and confidence in the DEM results.

Next, the force models used in the DEM simulations need to be investigated. Although not presented in this thesis, the peak pressure was found to be similar in screw systems using the linear hysteretic spring model and the Hertzian model, but the two models showed different stress paths in the plug section (where material is unloading). Capturing both the loading and unloading behavior of the screw feeder is important for capturing stress evolution of the material in such a complicated system. Preliminary comparisons with available experimental data show that the linear hysteretic model provides a poor approximation to the behavior of biomass. Additionally, because shear stresses dominate the behavior of the screw system, the sensitivity of the torque to the tangent force model must be investigated. The DEM simulations were used as a substitute for experimental data in this work, but there are still multiple steps that need to be taken in order to verify and validate the behaviors predicted in the simulations.

Another parameter of interest within compression screw feeders is the mass flow rate. DEM could be used to study the relative velocity of material against all screw surfaces, the conveying angle, and the dependency of mass flow rate on geometry, material properties, and boundary conditions, and more. Understanding the flow fields of material within a compression screw feeder is vital to understanding how torque is developed, and further investigation may relax some of the limiting assumptions used in the current work.

The final suggestion for future work is to extend the pressure/stress analysis to consider the change in a material's solid fraction over the length of the screw. Without accurate force models the stress-displacement behavior of the material cannot be well captured by the simulations, and because solid fraction and porosity are critical system parameters in the plug section, understanding the densification of material is critical. The methodology presented in this thesis could be extended to include a pressure-density relationship, which would allow the predicted pressure profiles to be mapped to solid fractions using experimental data. Once the density of the material is known, a mass flow rate model could also be developed, providing the last of the three

major operating parameters of a compression screw feeder: screw torque, plug density, and mass flow rate.

## REFERENCES

- Broyer, E., & Tadmor, Z. (1972). Solids conveying in screw extruders part I: A modified isothermal model. *Polymer Engineering & Science*, 12(1), 12–24. <https://doi.org/10.1002/pen.760120103>
- Campbell, G. A., & Dontula, N. (1995). Solids Transport in Extruders. *International Polymer Processing*, 22(3), 199–207.
- Carleton, A. J., Miles, J. E. P., & Valentin, F. H. H. (1969). A study of factors affecting the performance of screw conveyers and feeders. *Journal of Manufacturing Science and Engineering, Transactions of the ASME*, 91(2), 329–333. <https://doi.org/10.1115/1.3591565>
- Dai, J., & Grace, J. R. (2008a). A model for biomass screw feeding. *Powder Technology*, 186(1), 40–55. <https://doi.org/10.1016/j.powtec.2007.10.032>
- Dai, J., & Grace, J. R. (2008b). Biomass screw feeding with tapered and extended sections. *Powder Technology*, 186(1), 56–64. <https://doi.org/10.1016/j.powtec.2007.10.033>
- Darnell, W. H., & Mol., E. A. J. (1956). No Title. *Society of Plastics Engineers*.
- DOE. (2016). Biorefinery Optimization Workshop Summary Report, (October 2016). Retrieved from [https://static1.squarespace.com/static/53a09c47e4b050b5ad5bf4f5/t/58b5928203596ec6631c4065/1488294533706/biorefinery\\_optimization\\_workshop\\_summary\\_report.pdf](https://static1.squarespace.com/static/53a09c47e4b050b5ad5bf4f5/t/58b5928203596ec6631c4065/1488294533706/biorefinery_optimization_workshop_summary_report.pdf)
- George J. Burkhardt. (1967). Effect of Pitch, Radial Clearance, Hopper Exposure and Head on Performance of Screw Feeders. *Transactions of the ASAE*, 10(5), 0685–0690. <https://doi.org/10.13031/2013.39761>
- González-Montellano, C., Gallego, E., Ramírez-Gómez, Á., & Ayuga, F. (2012). Three dimensional discrete element models for simulating the filling and emptying of silos: Analysis of numerical results. *Computers and Chemical Engineering*, 40, 22–32. <https://doi.org/10.1016/j.compchemeng.2012.02.007>
- Hancock, A. W. (1970). *Ph.D. Thesis*.
- Hou, Q. F., Dong, K. J., & Yu, A. B. (2014). DEM study of the flow of cohesive particles in a screw feeder. *Powder Technology*. <https://doi.org/10.1016/j.powtec.2014.01.062>
- Hyun, K., & Spalding, M. A. (1997). A New Model for Solids Conveying in Single- Screw Plasticating Extruders. *ANTEC 1997 Plastics: Plastics Saving Planet Earth*, 1, 163.

- Janssen, H. A. (1895). Versuche uber Getreidedruck in Silozellen. *Vereines Derutscher Ingenieure*, 39, 1045.
- Ketterhagen, W. R., Curtis, J. S., Wassgren, C. R., & Hancock, B. C. (2009). Predicting the flow mode from hoppers using the discrete element method. *Powder Technology*, 195(1), 1–10. <https://doi.org/10.1016/j.powtec.2009.05.002>
- Landry, J. W., Grest, G. S., & Plimpton, S. J. (2004). Discrete element simulations of stress distributions in silos: Crossover from two to three dimensions. *Powder Technology*, 139(3), 233–239. <https://doi.org/10.1016/j.powtec.2003.10.016>
- Landry, J. W., Grest, G. S., Silbert, L. E., & Plimpton, S. J. (2003). Confined granular packings: Structure, stress, and forces. *Physical Review E - Statistical Physics, Plasmas, Fluids, and Related Interdisciplinary Topics*, 67(4), 9. <https://doi.org/10.1103/PhysRevE.67.041303>
- Lessmann, J. S., & Schoeppner, V. (2015). Validation of discrete element simulations in the field of solids conveying in single-screw extruders. *AIP Conference Proceedings*, 1664(May 2015). <https://doi.org/10.1063/1.4918405>
- Lessmann, J. S., & Schoeppner, V. (2016). Discrete element simulations and validation tests investigating solids-conveying processes with pressure buildup in single screw extruders. *AIP Conference Proceedings*, 1713(2016). <https://doi.org/10.1063/1.4942314>
- Liu, Y. Y., & Yeung, A. T. (2008). Accurate Measurement of Vertical Stress Distribution Underneath Sand Columns, (1), 1–6.
- McNab, G. S., & Bridgwater, J. (1979). A Theory for Effective Solid Stresses in the Annulus of a Spouted Bed, 57, 274–279.
- Mehrishal, S., Sharifzadeh, M., Shahriar, K., & Song, J. J. (2016). An Experimental Study on Normal Stress and Shear Rate Dependency of Basic Friction Coefficient in Dry and Wet Limestone Joints. *Rock Mechanics and Rock Engineering*, 49(12), 4607–4629. <https://doi.org/10.1007/s00603-016-1073-2>
- Merrow, E. W. (1985). Linking R&D To Problems Experienced in Solids Processing. *Chemical Engineering Progress*.
- Merrow, E. W., Phillips, K. E., & Myers, C. W. (1981). Understanding Cost Growth and Performance Shortfalls in Pioneer Process Plants. *Library of Congress Cataloging in Publication Data*.

- Metcalf, J. R. (1965). Mechanics of the Screw Feeder. In *Proceedings of the Institution of Mechanical Engineers* (Vol. 180, pp. 131–146).
- Michelangelli, O. P., Gaspar-Cunha, A., & Covas, J. A. (2014). The influence of pellet-barrel friction on the granular transport in a single screw extruder. *Powder Technology*, 264, 401–408. <https://doi.org/10.1016/j.powtec.2014.05.066>
- Moysey, P. A., & Thompson, M. R. (2004). Investigation of solids transport in a single-screw extruder using a 3-D discrete particle simulation. *Polymer Engineering and Science*. <https://doi.org/10.1002/pen.20248>
- Moysey, P. A., & Thompson, M. R. (2008). Discrete particle simulations of solids compaction and conveying in a single-screw extruder. *Polymer Engineering and Science*. <https://doi.org/10.1002/pen.20845>
- Nedderman, R. M. (1992). *Statics and Kinematics of Granular Materials*. Cambridge University Press.
- Ovarlez, G., & Clément, E. (2005). Elastic medium confined in a column versus the Janssen experiment. *European Physical Journal E*, 16(4), 421–438. <https://doi.org/10.1140/epje/i2004-10098-8>
- Patterson, T. J. (2014). Prediction of the stress at the inlet of the nip region in a roll compactor.
- Sperl, M. (2006). Experiments on corn pressure in silo cells - Translation and comment of Janssen's paper from 1895. *Granular Matter*, 8(2), 59–65. <https://doi.org/10.1007/s10035-005-0224-z>
- Tadmor, Z., & Klein, I. (1970). *Engineering Principles of Plasticating Extrusion*.
- Trippe, J., & Schöppner, V. (2018). Modeling of solid conveying pressure throughput behavior of single screw smooth barrel extruders under consideration of backpressure and high screw speeds. *International Polymer Processing*, 33(4), 486–496. <https://doi.org/10.3139/217.3507>
- Vanel, L., Cates, M. E., & Wittmer, J. P. (1999). Stresses in silos: Comparison between theoretical models and new experiments, 6–9.
- Walker, D. M. (1966). An approximate theory for pressures and arching in hoppers. *Chemical Engineering Science*, 21(3), 975–997. [https://doi.org/10.1016/0009-2509\(67\)80145-3](https://doi.org/10.1016/0009-2509(67)80145-3)
- Walters, J. K. (1973a). A theoretical analysis of stresses in axially-symmetric hoppers and bunkers. *Chemical Engineering Science*, 28(3), 779–789. [https://doi.org/10.1016/0009-2509\(77\)80012-2](https://doi.org/10.1016/0009-2509(77)80012-2)

- Walters, J. K. (1973b). A theoretical analysis of stresses in silos with vertical walls. *Chemical Engineering Science*, 28(3), 13–21.
- Walters, J. K., & Nedderman, R. M. (1973). A note on the stress distribution at great depth in a silo. *Chemical Engineering Science*, 28(10), 1907–1908. [https://doi.org/10.1016/0009-2509\(73\)85077-8](https://doi.org/10.1016/0009-2509(73)85077-8)
- Wambaugh, J. F., Hartley, R. R., & Behringer, R. P. (2010). Force networks and elasticity in granular silos, *145*, 135–145. <https://doi.org/10.1140/epje/i2010-10608-1>
- Yu, Y., & Arnold, P. C. (1997). Theoretical modelling of torque requirements for single screw feeders. *Powder Technology*, 93(2), 151–162. [https://doi.org/10.1016/S0032-5910\(97\)03265-8](https://doi.org/10.1016/S0032-5910(97)03265-8)